PETROLOGICAL AND GEOCHEMICAL INVESTIGATION OF POLYMETAMORPHIC METABASIC ROCKS FROM THE SONGSHUGOU OPHIOLITE, CHINA

Master Thesis

by

Maximilian Belic, BSc

Submitted at

Graz University of Technology

Supervisor

Ao.Univ.-Prof.Mag.Dr.rer.nat., Christoph A. Hauzenberger

Graz, spring 2017

1 Acknowledgement

Without the help and support of all the kind people around me, it would not have been possible to write this master thesis. My sincere gratidude goes to my supervisor Dr. Christoph Hauzenberger, who has expertly guided me throughout the whole thesis, with advice, expertise, mentoring in the lab and and not in the least his enthusiasm for the field. I would also like to thank Dr. Yunpeng Dong for his advice and support. Special thanks to Dr. Karl Ettinger and Mr. Jürgen Neubauer for assistance with the electron microprobe and the scanning electron microscope and all other faculty members of the Department of Mineralogy and Petrology. Thanks to Mr. Anton Pock for his assistance in the preparation of thinsections.

I am also very grateful to all my friends and fellow students who supported me throughout the thesis. Many thanks also to my friend Patrick, for his linguistic advice and motivation.

And finally, above all, I would like to thank my wife Melilssa for all her love, encouragement and great patience at all times and my parents who were supporting me through the years during my entire education.

2 Abstract

The Qinling Orogenic Belt is one of the major collisional orogens in eastern Asia and marks the natural boundary between North China Craton and South China Craton. (Zhang et al., 1989, 1995; Dong et al., 2011c). The Songshugou ophiolite is the largest ophiolite to be found in the North Qinling Belt. It is comprised of a series of ultrabasic and metabasic rocks, which were emplaced as a lense shaped body into the southern margin of the Qinling Group during the Proterozoic closure of the Songshugou Ocean (Dong et al., 2008). A detailed geochemical and petrological investigation of garnet amphibolites of the metabasic unit was conducted. Mineral chemical analyses and whole rock analyses were performed with electron microprobe analysis, inductively coupled plasma mass spectrometry, and wavelength dispersive X-ray fluorescence spectroscopy. The metabasic unit can be divided into garnet amphibolites and amphibolites. Amphibolites show trends of tholeiitic differentiation. Garnet amphibolites show different trends, probably related to amphibole fractionation. Garnet amphiobolites display highly fractionated REE_N patterns (La_N/Yb_N = 2.3 – 4.6), similar to trends observed in EMORB and OIB, but with higher overall REE abundance ($\sum REE_N$ = 130 – 700). Amphibolites are far less enriched in REEs and hardly show any REE fractionation ($\sum REE_N$ = 48 – 70). Based upon trace elements, and REE patterns, amphibolites represent oceanic tholeiitic basalts with T-MORB and E-MORB character; Grt amphibolites, however, represent either unusual SiO_2 – poor FeO and TiO_2-rich E-MORB melts; or probably evolved dikes of alkaline affinity.To determine metamorphic conditions, the petrography was studied thoroughly, pseudosections were generated and conventional geothermobarometric calculations were performed. Thermodynamic modelling of garnet zoning patterns of major and trace elements along with inclusions, as well as textural analysis indicate a polymetamorphic history. Garnets clearly show characteristics of discontinuous growth; as they display a sudden increase in grossular, and decrease in almandine, components at the rims. REE distribution patterns of garnets also show clear trends, with rims enriched in Tb, Dy and Ho (compared to garnet cores), which can be attributed to the breakdown of amphibole at higher PT conditions. In various samples, symplectitic pyroxenes with inclusions of Mg-hornblende + plagioclase ± quartz were observed. The presence of symplectitic pyroxenes after omphacite, is commonly regarded as evidence of prior eclogite-facies metamorphism, generated in response to post-peak decompression (Wilkerson et al., 1988; O'Brien et al., 1990; Droop et al., 1990; Zhao et al., 2001). Recalculated preliminary pyroxene compositions indicate a high pressure metamorphic event. This theory is supported by garnet isopleth geothermobarometry, where garnet core isopleths indicate an older amphibolite to granulite facies metamorphic episode (630°C–740°C and 0.7–0.9 GPa). Garnet-rim isopleths, however, represent eclogite facies conditions (570°C–630°C and 1.7–2.1 GPa). Different stages of garnet breakdown to plagioclase + amphibole, were also observed. In stronger retrograded samples, plagioclase + amphibole ± quartz pseudomorphs entirely replace former garnet grains. Certain coronas and symplectites also contain Prehnite which was formed during late retrograde stages at low PT conditions (200°C–350°C). On grounds of our study, a polymetamorphic history of Songshugous metabasic rocks can be concluded. The age of the eclogite facies metamorphic event is probably related to the closure of the Shangdan Ocean during the early Paleozoic, while the age of garnet core growth remains enigmatic. Those characteristic retrograde textures together with the PT path point at decompression and later cooling possibly related to two stages of lifting in North Qinling at around 450Ma and 420Ma (Liu et al., 2013; Li Tang et al., 2016).

Keywords: Songshugou ophiolite; Qinling orogen; North Qinling Belt; HP eclogite facies

3 Zusammenfassung

Das O-W verlaufende Qinling Gebirge ist eines der Hauptkolliosionsorogene Ostasiens und befindet sich zwischen dem North- und dem South China Kraton. Die O-W verlaufende Shangdan Suture Zone (SSZ) unterteilt das Gebirge in das North- und das South Qinling Terrane (Zhang et al., 1989, 1995; Dong et al., 2011c). Der Songshugou Ophiolith ist der größte, zahlreicher entlang der SSZ aufgeschlossenen Ophiolithe, und besteht aus einer ultrabasischen und einer metabasischen Einheit, die im Zuge der proterozoischen Schließung des Songshugou Ozeans auf den südlichen Teil der Qinling Group aufgeschoben wurden (Dong et al., 2008). Diese Arbeit befasst sich mit dem detaillierten petrologischen Studium der Metabasite. Proben wurden petrographisch und mineralchemisch untersucht (Elektronenstrahlmikrosonde, LA-ICPMS) und Gesamtgesteinschemismen mittels Röntgenfluoreszenzanalyse und ICPMS bestimmt. Die metabasische Einheit beinhaltet Amphibolite und Granat Amphibolite. Erstere folgen tholeiitischen Differentiationstrends, während geochemische Trends der Granat Amphibolite auf Amphibolfraktionierung zurückzuführen sind. Im Gegensatz zu den Amphiboliten ($\sum REE_N$=48–70, La_N/Yb_N=0.8–2.0), sind die Granat Amphibolite stark an REE angereichert ($\sum REE_N$=130–700) und zeigen EMORB/OIB ähnliche, ausgeprägte REE-Fraktionierung (La_N/Yb_N=2.3–4.6). Die Chemismen und REE Muster der Amphibolite sind charakteristisch für ozeanische tholeiitische Basalte mit T-MORB und E-MORB Charakter. Granat Amphibolite hingegen haben Chemismen, die entweder ungewöhnliche, SiO_2 untersättigte, an FeO und TiO_2 angereicherte E-MORB Schmelzen, oder weit entwickelte, mafische, alkaline Dikes darstellen. Granatzonierungsmuster lassen auf diskontinuierliches Wachstum schließen. Mit vergleichsweise hoher Grossular- und geringer Almandinkomponente, unterscheiden sich die Granatränder eindeutig von den -kernen. Auch REE Verteilungsmuster von Granatkern- und Randbereichen differieren stark. Die Granatränder sind an Tb, Dy, und Ho angereichert, was auf den Zusammenbruch von Amphibol bei höheren PT Bedingungen während des Granatwachstums hinweist. Matrix-Klinopyroxen tritt meist als Symplektit mit Verwachsungen von Mhbl+Pl±Qz auf. Derartige Symplektite resultieren üblicherweise aus dem Zusammenbruch von Omphazit während dekompressiver Tektonik (Wilkerson et al., 1988; O'Brien et al., 1990; Droop et al., 1990; Zhao et al., 2001). Das Rückrechnen der Symplektite zu ursprünglichen Klinopyroxenchemismen ergab jadeitreiche Omphazitchemismen (symptomatisch für Paragenesen hochgradiger Metamorphose). Zur PT Bestimmung des Granatwachstums wurden Granatkerne und -ränder zusammen mit den darin vorkommenden Einschlüssen mineralchemisch quantifiziert und konventionelle Geothermobarometer als auch Granatisoplethengeothermobarometrie angewandt. Die Berechnungen ergaben: 1) amphibolithfazielle bis granulitfazielle Bedingungen für das initiale Granatwachstum (630°C–740°C und 0.7–0.9 GPa), 2) eklogitfazielle Bedingungen für Granatränder (570°C–630°C und 1.7–2.1 GPa). Die Bildung von Klinopyroxensymplektit, Koronen um Granat und Reaktionsbändern zwischen Matrix-Klinopyroxen und Granat, deuten auf einen dekompressionsgeprägten retrograden PT Pfad. Prehnit, welcher teilweise in Cpx-Symplektiten und Plagioklaskoronen auftritt, wurde während später Phasen des retrograden Pfades bei sehr geringen Temperaturen (200°C–350°C) gebildet. Vorliegende Ergebnisse lassen auf eine polymetamorphe Geschichte der Metabasite schließen. Die eklogitfazielle Metamorphose könnte im Bezug zur Schließung des Shangdan Ozeans im frühen Paläozoikum stehen. Das Auftreten retrograder Texturen und niedergradiger Minerale wie Prehnit, lässt auf einen retrograden PT Pfad mit anfänglicher Dekompression und späterem Abkühlen schließen der möglicherweise im Bezug zur 2 phasigen Hebung des North Qinlings um 450Ma und 420Ma steht (Liu et al., 2013; Li Tang et al., 2016).

Schlagwörter: Songshugou Ophiolith; Qinling Orogen; North Qinling Belt; HP eklogitfaziell

4 INDEX

5 Introduction

5.1 Geological Frame

China is located in one of the most complicated tectonic areas in the world. Since archaic Archean China underwent 17 significant tectonic events which lead to a tectonically complex framework. It is comprised of three major Precambrian cratons and several surrounding Phanerozoic orogenic belts i.e. (North China Craton NCC, South China Craton SCC and Tarim Craton). All cratons evolved individually and amalgamated during the Paleozoic period through the Upper Triassic, forming the main part of the Eastern Asia Continent. The SCC is subdivided into the Yangtze Block (YZB) and the Cathaysia Block (CTB) which were cohered during the Neoproterozoic (Zhou et al., 2008; Shu, 2012). All major tectonic units (cratons, and fold systems) are displayed in Fig. 1.

The NCC (North China Craton) is considered to be one of the oldest cratons in the world (3.8 Ga) and mainly comprises late Paleoproterozoic to Paleozoic sedimentary covers, Precambrian metamorphic basements and Mesozoic intrusions. The craton extends over an area of about 1.700.000 km² in north-eastern China, northern Korea and the southern parts of Mongolia; and is composed of several micro-blocks that had been amalgamated about 2.5 Ga ago (Zhai 2011; Zhai and Bian, 2001).

The SCC (South China Craton) consists of the Yangtze Craton, and the Cathaysia Craton; which are separated by the Jiangnan Orogenic Belt. The Yangtze Craton contains two basements: An upper-level metamorphic fold basement in the upper part, and a middle-level metamorphic basement in the lower part (Ren et al., 1990).

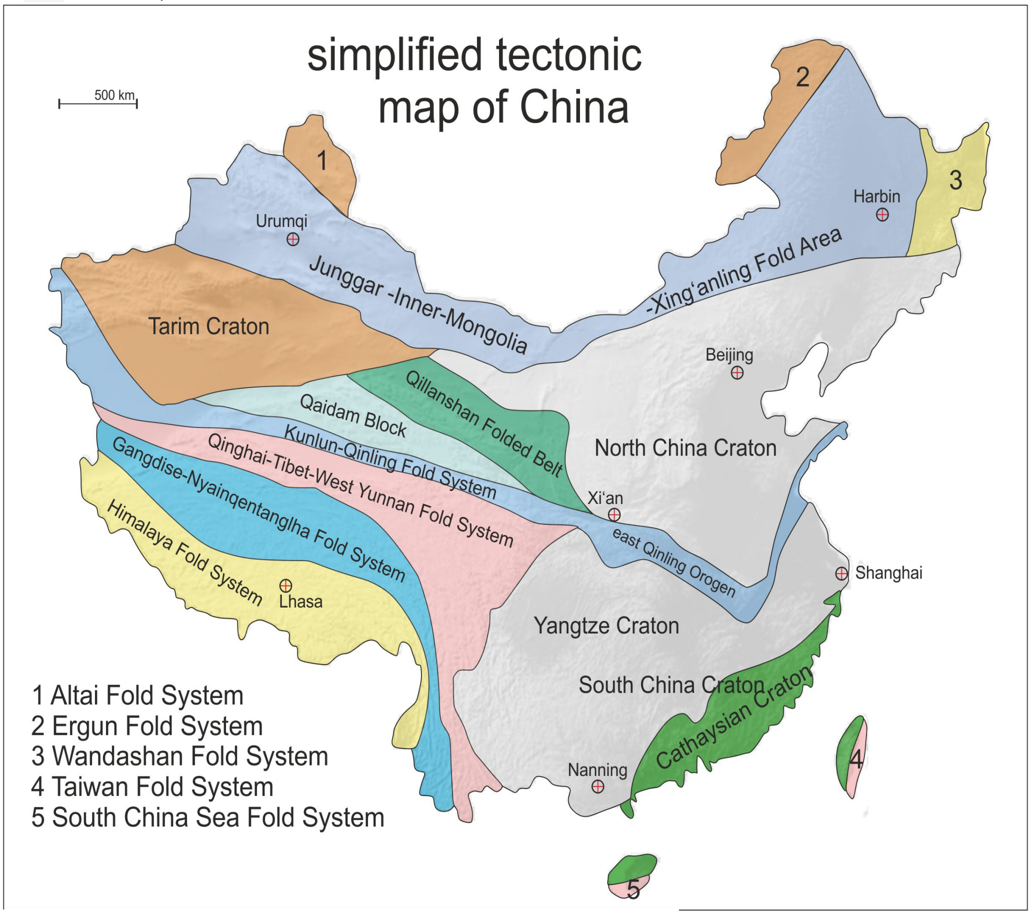

Fig. 1 Chinese map of regional geological units (modified after Ren et al. 1990)

5.1.1 The Qinling Orogenic Belt (QOB)

The Qinling Orogenic Belt (QOB) extends west-east nearly 2500 km across Central China. Conjoined with the Dabie, Qilian and Kun Lun mountains, it is one of the major collisional orogens in eastern Asia situated in between North China Craton (NCC) and South China Craton (SCC). To the west, this belt unites with the Qilian and Kun Lun belts. To the east, it is truncated by the N-S striking Tan Lu Fault. Multiple stages of convergence between the two cratonic blocks (NCC, SCC) induced a complex geologic framework (Tseng et al., 2009; Dong et al., 2011c; Wu and Zheng, 2013). The QOB was thrust onto the southern margin of the NCC along the Lingbao-Lushan-Wuyang fault (LLWF) in the north; and onto the northern margin of the SCC along the Mianlue-Bashan-Xianguang fault (MBXF) in the south. The Shangdan Suture Zone (SSZ), a massive fault system, traverses the orogenic belt from east to west dividing it into North Qinling Belt (NQB) and South Qinling Belt (SQB) (GW.Zhang et al., 1995a; S.G. Li et al., 1996; Dong et al., 1999; GW.Zhang et al., 2001; Xu et al., 2002; Dong et al., 2014). Along this zone, several early Paleozoic ophiolites and subduction-accretion related volcanic arc assemblages are exposed, hence, it has been regarded as the main collision zone between NCC and SCC.

Previously, NCC and SCC were assumed to represent former parts of a united China continent; before they were segregated by the opening of the Shangdan Ocean (Yuan, 1991; Zhang et al., 1991). Yet further study has shown that that Precambrian Basement and cover sequences of both units diverge significantly. Hence, independent tectonic histories of the NCC and SCC before Phanerozoic collision were concluded (Zhang et al., 1996; G.W. Zhang et al., 2001; Zhu, 2001; Zhai, 2013, 2014; Zhao and Zhai, 2013; Dong et al., 2014).

Among most authors, the assumption of the Shangdan suture zone (SSZ) representing the main subduction and collision zone of NCC and SCC, is widely accepted. A temporal allocation of those events, however, is controversial. According to different authors it ranges from early Paleozoic, Devonian to Triassic (e.g.; Kröner et al., 1993; Li et al., 1993a; Okay and Sengör, 1993; Yin and Nie, 1993; Li, 1994; Gao et al., 1995; Ames et al., 1996; Zhang et al., 1997a; Hacker et al., 1998; Zhai et al., 1998; Zhang et al., 2001).

5.1.2 Tectonic belts of the QOB

With the Paleozoic Shangdan Suture Zone (SSZ), the Triassic Mianlue Suture Zone (MLSZ) and several other major strike-slip faults, the QOB can be tectonically divided into 5 basic zones: **1** Southern North China Craton (S-NCC), **2** North Qinling Belt (NQB), **3** Central Qinling Belt (CQB), **4** South Qinling Belt (SQB) and **5** northern South China Craton (N-SCC).

The S-NCC is bounded by the Lingbao-Lushan-Wuyang fault (LLWF) in the north and the Luonan-Luanchuan fault (LLF) in the south. It mainly comprises deformed and metamorphosed (dominantly amphibolite facies) Upper Archean – Lower Proterozoic basement complexes such as the Taihua Group and the Tietonggou Group (Zhang et al., 2000) which are superimposed by: **1** low-grade to non-metamorphic Mid-Proterozoic rift-related volcanic rocks, **2** Mid- to Neo-Proterozoic marine facies clastic and carbonate sequence, **3** Uppermost Neoproterozoic tillite (G.W. Zhang et al., 2001) and **4** Cambrian to Ordovician passive continental margin sequences. All those overlaying rocks were thrust along the LLWF onto the NCC. During Cretaceous, manifold granitoid plutons intruded into S-NCB (e.g. Lantian, Laoniushan and Huashan granitoids) (Mao et al., 2005; Li et al., 2006a; Ye et al., 2006; Zhu et al., 2008a; Zhang et al., 2010). In the south, the S-NCC is bounded by the LLF and the Kuanping Suture (KPS) to the NQB. (Dong et al., 2011, 2016).

The CQB is situated between SSZ and the MXDZ and mainly consists of Neoproterozoic gneiss and amphibolite basement rocks represented by the Foping Group, and the Tongbaishan (Tongbai and

Hong'an Groups). Cover sequences of the eastern CQB are mainly represented by pelagic turbidite rocks, which were deposited into a forlandbasin during Devonian times (Dong et al., 2013). In the west, the CQB includes a northern Upper Paleozoic zone and a southern Triassic zone separated by the Minxian-Danchang and Fengxian fault.

The SQB is bounded by the Mianlue Suture Zone (MXLZ) in the north and the Yangpingguan fault (YPGF) as well as the Mianlui-Bashan-Xiangguang fault (MBXF) in the south. Along the MBXF, the QOB was thrust onto the northern margin of the SCC during Late Paleozoic to Middle Triassic times (Zhang et al., 1995). The SQB largely consists of: **1** Neoarchean basement, **2** Neoproterozoic clastic and volcanic rocks, and **3** Upper Proterozoic to Lower Paleozoic successions, as well as minor Upper Paleozoic to Middle Triassic strata in the northern SQB (Dong and Santosh., 2016; Zhang et al., 2001).

The N-SCC, also known as the foreland fold-thrust belt, is bound to the SQB by the MBXF, and progressively grades into undeformed Mesozoic sequences within Jianghan and Sichuan basins in the main region of the SCC. The SCC is comprised of a highly metamorphosed Neoarchean-Paleoproterozoic crystalline basement, greenschist facies Meso-Neoproterozoic transitional basement, and a cover sequence of non-metamorphosed Proterozoic-Mesozoic clastic and carbonate rocks (G.W.Zhang et al., 1995a,b, 2000; Dong et al., 2011a).

The NQB is situated between the LLF and the SSZ (Shangdan Suture Zone). It extends over 1000 km from east to west and mainly comprises: **1** Precambrian crystalline basement units, **2** Neoproterozoic-Lower Paleozoic ophiolites and **3** Mesoproterozoic-Paleozoic volcano-sedimentary assemblages which are sparsely overlain by Phanerozoic cover rocks such as Carboniferous and/or Permian clastic sediments (Dong et al., 2011a). The Precambrian basement underwent amphibolite facies metamorphism at ~ 1.0 Ga and greenschist facies metamorphism at ~ 400 Ma (Liu et al., 1993; Zhang et al., 1994b).

The main units exposed in the NQB from north to south have been designated as the Kuanping Group, Erlangping Group, Qinling Group, Songshugou ophiolite and Danfeng Group (Danfeng ophiolite included). Those units are separated by thrust faults and ductile shear zones.

The Meso-Neoproterozoic Kuanping Group consists mainly of an ophiolite unit (greenschist, amphibolite facies) and a meta-sedimentary unit (quartzite, mica schist, marble). Protolithes of the ophiolitic metabasites are tholeiitic basalts with N-MORB to T-MORB geochemistry, representing metamorphosed oceanic crust (Zhang and Zhang, 1995 Diwu et al., 2010; Dong et al., 2014). The metasedimentary unit is considered to represent overlying accretionary wedge material possibly related to the closure of the Paleozoic Erlangping back-arc basin with youngest detrital zircon ages approaching 610 to 500 Ma. (C.L.Zhang et al., 1994, 2004; Yan et al., 2008; Dong et al., 2011b). Sm-Nd whole rock isochron ages range from 0.94 to 1.2 Ga (Zhang et al., 1994; Zhang and Zhang, 1995).

The Erlangping Group is comprised of three units: **1** the Erlangping ophiolite (pillow basalts, sparse ultra-mafic rock, sheeted dike basalt, gabbro and radiolarian chert), **2** clastic sedimentary rocks, and **3** carbonate rocks. Geochemistry of basalts and radiolarites suggest a back-arc basin existing during Ordovician and Silurian (Wang et al., 1995; Sun et al., 1996).

The Danfeng Group discontinuously outcrops along the SSZ, and contains metavolcanic and metasedimentary rocks. Meta-mafic rocks of this unit are regarded as ophiolite formed during early Paleozoic (Dong et al., 2011b).

The Qinling Group is generally regarded as micro continental terrain (G.W.g et al., 1995). It consists of gneiss, amphibolite, and marble (clastic rocks and limestone as protolith) (You et al., 1991). Zircon ages of gneiss and amphibolite suggest an evolutionary history of late Paleoproterozoic to Mesoproterozoic times (You et al., 1991; Shi et al., 2009; Yang et al., 2010; Wan et al., 2011; Diwu et al., 2012). A simplified tectonic map of the eastern QOB with its main geological units is displayed in Fig. 2.

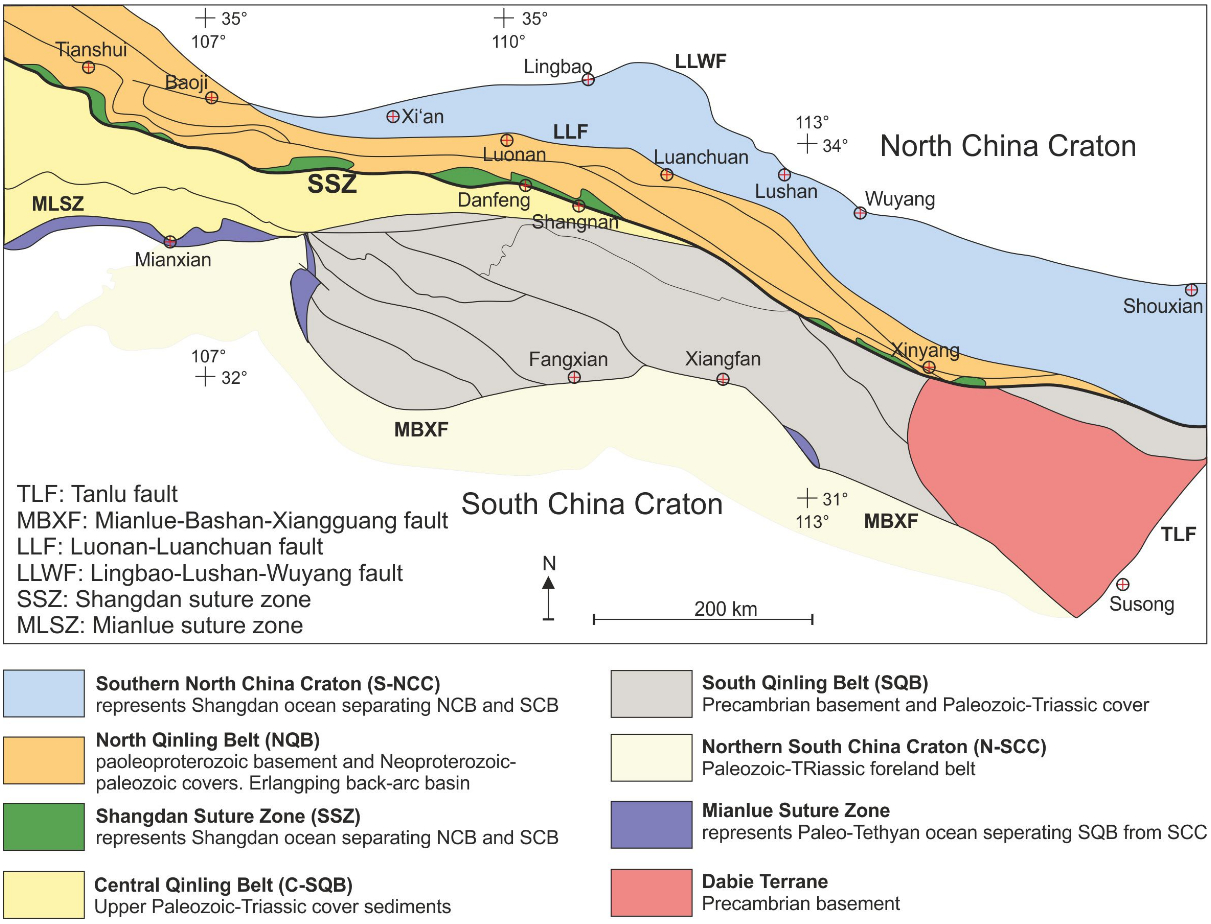

Fig. 2 Simplified tectonic map of the eastern QOB showing tectonic divisions. Modified after Dong et al. 2011a

5.1.3 Songshugou ophiolite

The Songshugou ophiolite complex is located in eastern Shaanxi Province and western Henan Province. It outcrops along the SSZ as a rootless nappe which was emplaced into the southern margin of the Qinling Group. The complex forms a SE-NW trending block about 27 km long and 3 km wide. In the north, the ophiolite has been thrust along the Jieling ductile shear zone onto the Qinling group. In the south it is bound to the Qinling Group and the Fushui gabbroic complex by the Xigou fault (Fig. 4, & Fig. 3).

It consists mainly of a series of ultrabasic, and a variety of tholeiitic metabasic, rocks. REE patterns, Trace element geochemistry and isotope composition show that the mafic rocks are mainly E-MORB and T-MORB metabasalts (Dong et al., 2008b). Nd, Sr and Pb isotopic data (Dong et al., 2008a) are isotopically similar to those of Indian Ocean MORB (Xu et al., 2002; Xu and Castillo, 2004). Hence, the metabasalts are believed to have been derived from a mantle source with a DUPAL isotope anomaly produced by exchange between the asthenosphere and a mantle plume (e.g. Dupre and Allegre, 1983; Hamelin et al., 1986; Mertz et al., 1991). The country rocks of Qinling Group are marble, and a gneiss-migmatite complex (Zhou et al., 1995).

Within the ophiolite sequence, fresh peridotites (mostly dunites and harzburgites), can be found. Fine grained dunites and harzburgites display schistose deformation with mylonitic textures and relict olivine porphyroblasts. Medium to coarse grained dunites exhibit typical cumulate textures without any conspicuous metamorphic overprint (Dong et al., 1996). Harzburgite crops out as undeformed to slightly deformed patches, lenses and veins penetrating dunite mylonite. Dunite mylonites show typical high-temperature deformational fabrics and dislocation, probably imposed by shearing processes in a subduction environment at temperatures beyond 1000°C (Dong et al., 1996). Low CaO (<0.39 wt.%) and Al_2O_3 (<0.51 wt.%) in conjunction with high MgO (41–48 wt.%) contents classify the peridotites as depleted, non-fertile mantle rocks. Dunites and harzburgites mainly consist of heterogranular forsterite rich olivine, enstatite rich orthopyroxene, Ca-amphibole (tremolite) and Mg-Fe-Mn amphibole (cummingtonite) ± chlorite ± talc ± chromite. Chromite occurs as disseminated phase but sometimes forms massive chromite bands. Chromites show increasing Fe-Cr zoning patterns towards their rim, which could be symptomatic of serpentinization or metamorphic processes (Pohl 2005). Chromite commonly includes sulfides e.g. pentlandite, pyrrhotine and Laurite (RuS_2) rich PGMs (platinum group minerals). Podiform chromite mineral chemistry clearly confirms the ophiolitic origin of Songshugou metabasic unit. The peridotite unit is cut by granitic, pegmatitic and dioritic intrusives. An up to 10 m wide serpentinized zone separates the peridotite from the metabasic unit.

The Metabasic unit occurs structurally underneath the peridotite body. It mainly consists of **1** hornblende amphibolite, **2** augen amphibolite and **3** garnet amphibolite. Hornblende amphibolite is structurally located at the lowermost part; in other words, the outmost parts of the unit. Augen amphibolite, presumably emerged out of garnet bearing metabasites, outcrops as 10 – 200 m wide areas structurally between garnet amphibolite and hornblende amphibolite. Garnet amphibolites occur as discontinuous lenses in the innermost or uppermost part of the metabasic unit. The modal abundance of garnet increases towards the core of the lenses, probably due to different degrees of garnet retrogression. Even though previously considered to represent a contact aureole around the peridotitic unit (Huang, 1984), garnet amphibolites were ascribed as retrograde eclogites in later publications (An et al., 1985; Liu et al., 1995; Chen et al., 1993; Liu & Zhou., 1994; Zhang, 1999). Garnet amphibolites and peridotites are separated by a ~ 10 m wide zone of serpentinization. Whole rock chemistry analyses of metabasic rocks point at basaltic protoliths with N-MORB and E-MORB characteristics (Zhou et al., 1995; Liu et al., 2004; Dong et al., 2008). Other subordinate rocks occurring in the metabasic Songshugou unit are felsic granulites close to the Xigou fault as well as marble and peridotitic rocks outcropping as elongated blocks. The genesis of garnet amphibolites is considered to be related to oceanic subduction, and the emplacement of the Songshugou ophiolite (Liu et al., 1995). Several publications suggest a peak metamorphic age of 537 – 480 Ma based on obtained zircon U-Pb age data (Su et al., 2004; Chen et al., 2004; Liu et al., 2009; Qian et al., 2013; Li et al., 2014b, Li Tang et al., 2016). Metabasic rocks yield Sm-Nd whole rock isochron ages of 1030 ± 46 Ma, with depleted mantel model ages (T_{DM}) ranging from 1271 to 1440 Ma, describing the age of basaltic protolith (Dong et al., 2008a). Garnet amphibolites are the focus of this present study.

The Fushui meta-gabbroic complex is situated to the south of the Songshugou complex. It consists mainly of metagabbro and metadiorite, and lesser amounts of tonalite and ultrabasic rocks. With an area of about 52.5 km² it outcrops as the largest meta-gabbroic complex in the NQB. Geochemistry indicates arc-magmatic signatures with calc-alkalic rocks cross-cutting tholeiitic rocks (Zhang Z-J. 1991). Whole - rock Sm-Nd model ages (1290-1570 Ma) of metagabbros, point at a Jinningian related evolution of Fu-shui complex.

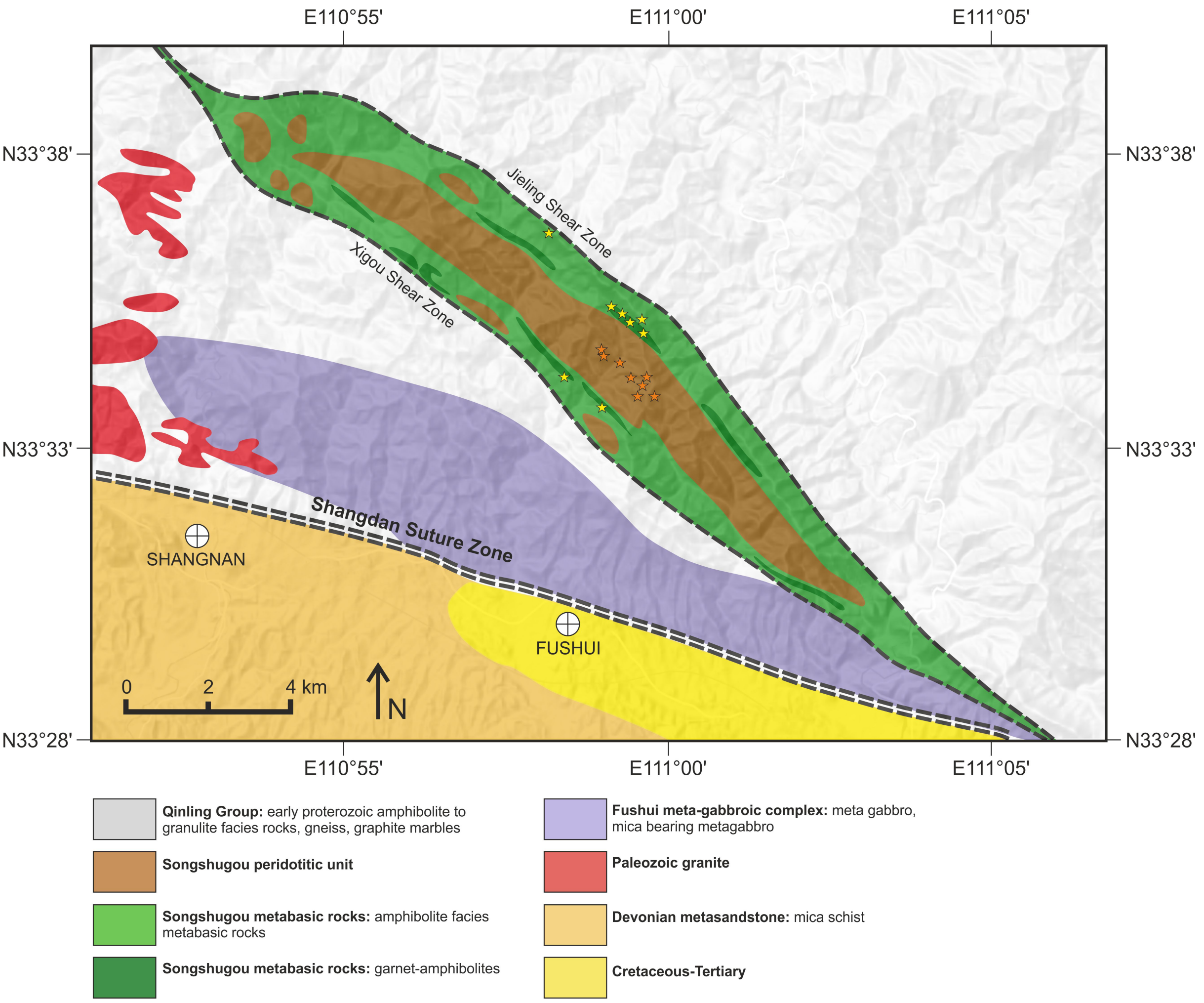

Fig. 3 Geological map of the Songshugou ophiolite, NQB (after Dong et al., 2008) yellow stars represent metabasic samples, orange ones samples of peridotite

5.2 Analytical techniques

5.2.1 REM and electron microprobe analysis:

Samples were prepared as polished thin sections (~30µm) and thick sections (~120µm); and then, thoroughly investigated by transmitted and reflected light microscopy. Quantitative mineral analyses and chemical mappings, were carried out by using a scanning electron microscope JEOL JSM 6310 with a LINK ISIS energy dispersive system (measurement time for energy dispersive elements 100 sec) equipped with a MICROSPEC wavelength dispersive system (measurement time for wavelength dispersive elements 20 sec on peak position) at the Institute of Earth Sciences, Mineralogy and Petrology, University of Graz. Then, additionally, a JEOL JXA 8200 electron microprobe (UZAG EUGEN F.STUMPFL Electron Micropobe Laoratory, at the Montanuniversity, Leoben) was utilized for detailed petrology on carbon-coated thin sections. Conditions of measurements on both devices were ~ 5 (SEM) and 12 (EPMA) nA beam current, ~1 µm beam diameter (point mode) and 15 kV acceleration voltage. Most minerals were measured in point mode except for plagioclase, which was analyzed using a rastered beam (10 x 10 µm) to minimize loss of Na and K, if grain sizes permitted. Acceleration voltage was increased to 20 kV for sulfur compound analysis. Natural and synthetic standards used for element calibration on the JEOL JSM 6310 are listed in table 1 and table 2. Element distribution mappings were executed with a JEOL JXA 8200 electron microprobe.

table 1 used standards for silicates for energy and wavelength dispersive analysis with JEOL JSM 6310

element	**dispersive system**	**standard**
F	*WDX*	F-phlogopite S61 HO88
Na	*WDX*	jadeite MS 2970 A Clear Creek
Mg	*EDX*	garnet S6 #12442 Gore Mountain
Al	*EDX*	adular S1
Si	*EDX*	adular S1
P	*EDX*	F-apatite S3 Wilberforce
Cl	*EDX*	atacamite S9 NMW
K	*EDX*	adular S1
Ca	*EDX*	wollastonite Auerbach
Ti	*EDX*	titaniteS4 Bündner Oberland ETHZ
V	*EDX*	chromite S7 53-IN-8
Cr	*EDX*	chromite S7 53-IN-8
Mn	*EDX*	rhodonite S5 660-388
Fe	*EDX*	garnet S6 #12442 Gore Mountain
Ni	*EDX*	NiO_Ni-Tiegel
Cu	*EDX*	Cu-Metall
Zn	*EDX*	ghanite USNM 145883

table 2 Standards used for sulphides, for energy analysis with JEOL JSM 6310

element	dispersive system	standard
S	*EDX*	chalcopyrite Western mines
Cr	*EDX*	chromite 53-in-8
Fe	*EDX*	chalcopyrite Western mines
Ni	*EDX*	nickel-metal
Cu	*EDX*	chalcopyrite Western mines
Zn	*EDX*	%C21 Zn60.3Fe6.43S33.27
As	*EDX*	Cabri-526 (PtAs2)
Ru	*EDX*	Ru-metal
Rh	*EDX*	Rhodium-metal
Pd	*EDX*	Cabri-461 (Pd3As)
Sb	*EDX*	Cabri-141 (NiSb)
Te	*EDX*	Dutrizac (Bi2Te3)
Os	*EDX*	Osmium-metal
Ir	*EDX*	Iridium-metal

Mineral formulas and geothermobarometry were calculated using the program PET 7 (Dachs, 1998).

5.2.2 Trace element and REE mineral analysis:

Trace elements and REEs of mineral phases were obtained in polished thick sections through laser ablation inductively coupled plasma mass spectrometry (LA-ICP MS) (NAWI Graz Labs for Water, Mineral and Rocks, Graz University of Technology) with an ESI New Wave 193 Excimer Laser (193nm wavelength) attached to a quadrupole Agilent 7500 CX mass spectrometer. A beam size diameter of 35 µm, 60 s of ablation and a dwell time of 35 msec for each mass data acquisition was used for element analyses. NIST SRM 612 glass was used for standardization and the USGS reference glass BCR-2G was analyzed as monitor standard. The quality of spot measurements was assessed using the software GLITTER. For garnet and amphibole analysis Si was taken as internal calibration element, Ca for apatite.

5.2.3 Whole rock chemistry:

Sample preparation was carried out at the Institute of Petrology and Mineralogy, University of Graz. Fresh rock samples were crushed and powdered using a carbide mill. Whole rock major element concentrations were obtained by wavelength dispersive fluorescence spectrometry (WDXRF) on fused glass discs using a Bruker Pioneer S4 under standard conditions (Institute of Earth Sciences, Mineralogy and Petrology, University of Graz). For quality control of the method, one randomly selected sample was analyzed twice. Whole rock data processing was executed using the R language based software package GCDkit (Geochemical Data Toolkit, version 3) (Janousek et al., 2006a). Perplex_X version 6.7.3 (Connolly, 2005) was used for thermodynamic phase equilibrium calculations with the revised hp04ver.dat dataset from Holland and Powell (1998).

Inductively coupled plasma mass spectrometry (ICP MS) was used to determine whole rock trace element and rare earth element REE concentrations with abundances < 20 ppm (Institute of chemistry, University of Graz) with a quadrupole Agilent 7500 CX mass spectrometer.

Mineral abbreviations used according to Whitney and Evans (2010) are displayed in table 3.

table 3 Mineral abbreviations used according to Whitney and Evans (2010)

Mineral abbreviations after Whitney and Evans, 2010			
Act	actinolite	Jd	jadeite
Aeg	aegirine	Kfs	K-feldspar
Ab	albite	Lws	lawsonite
Afs	alkali feldspar	Liq	liquid
Alm	almandine	Mhb	magnesiohornblende
Als	alumosilicate	Mag	magnetite
Amp	amphibole	Mnz	monazite
An	anorthite	Ol	olivine
Ap	apatite	Omp	omphacite
Aug	augite	Or	orthoclase
Bt	biotite	Opx	orthopyroxene
Ccp	chalcopyrite	Prg	pargasite
Chl	chlorite	Pn	pentlandite
Chr	chromite	Ph	phengite
Czo	clinozoisite	Pl	plagioclase
Coe	coesite	Prh	prehnite
Cum	cummingtonite	Pmp	pumpellyite-(Al)
Di	diopside	Py	pyrite
Ed	edenite	Prp	pyrope
En	enstatite	Po	pyrrhotite
Ep	epidote	Qz	quartz
Fsp	feldspar	Rt	rutile
Grt	garnet	Sps	spessartine
Ged	gedrite	Spn	sphene
Gln	glaucophane	Tlc	talc
Grs	grossular	Tr	tremolite
Hst	hastingsite	Ts	tschermakite
Hbl	hornblende	Zrn	zircon
Ilm	ilmenite	Zo	zoisite

5.3 Sampling

Schistose plagioclase amphibolites (X32, X33), garnet amphibolites (X35, X36, X37) and augen amphibolites (X38, X42, QS2D) were collected from the Songshugou metabasic-ultramafic complex together with harzburgites, dunites and chromite-peridotites (QS2H1, QS2H1.2, QS2A, QS2B, QS2C, QS2E, QS2F, QS2G). Sample locations with rough descriptions are presented in table 4 and table 5. The focus of this study was on the metabasic unit, especially the garnet-amphibolites. Peridotitic rocks are only mentioned peripherally.

table 4 metabasic samples, Songshugou ophiolite

sample nr.	rock type	locality	mineralogy
X32	schistose plagioclase-amphibolite	33-33.895N 110-58.369E	Qz, Pl, Amp
X33	schistose plagioclase-amphibolite	33-34.230N 110-58.236E	Qz, Pl, Amp
X35	garnet-amphibolite	33-34.671N 110-58.038E	Amp, Grt, Cpx, Pl, Qz, Ilm, Czo/Ep, Ap
X36	garnet-amphibolite	33-34.671N 110-58.038E	Amp, Grt, Cpx, Pl, Qz, Ilm, Czo/Ep, Ap, Spn, Bt
X37	garnet-amphibolite	33-34.671N 110-58.038E	Amp, Grt, Cpx, Pl, Qz, Ilm, Czo/Ep, Ap
X38	augen-amphibolite	33-34.671N 110-58.038E	Amp, Grt, Cpx, Pl, Qz, Ilm, Czo/Ep
X42	augen-amphibolite	33-34.671N 110-58.038E	Amp, Pl, Qz, Ilm, Czo/Ep, Bt
QS2D	augen-amphibolite	33-34.671N 110-58.038E	Amp, Pl, Ilm, Czo/Ep

table 5 peridotite samples, Songshugou ophiolite, PGM abbreviation for platinum group minerals

sample nr.	rock type	locality	mineralogy
QS2H1	chromite-harzburgite	33-32.109N 110-57.881E	Ol, Amp, Chl, Chr, PGM, Opx
QS2H2	chromite-harzburgite	33-32.109N 110-57.881E	Ol, Amp, Chl, Chr, PGM, Opx
QS2B	harzburgite	33-32.109N 110-57.881E	Ol, Amp, Chr, Opx
QS2E	chromite-dunite	33-32.109N 110-57.881E	Ol, Amp, Chr
QS2F	ol-orthopyroxenite	33-32.109N 110-57.881E	Ol, Amp, Chl, Chr, Opx
QS2C	chromite-harzburgite	33-32.109N 110-57.881E	Ol, Amp, Chr, Opx
QS2G	harzburgite	33-32.109N 110-57.881E	Ol, Amp, Chl, Chr, Opx, Tlc
QS2A	harzburgite	33-32.109N 110-57.881E	Ol, Amp, Chr, Opx

6 Petrography

Metabasic rocks were collected and studied in thin sections. Sample locations are displayed in Fig. 3. Seven samples were selected for detailed electron microprobe analysis. As already described by Zhang et al. (1999), the metabasic unit can be subdivided into three groups according to mineral assemblage and textures: (1) hornblende amphibolite, (2) augen amphibolite, and (3) garnet amphibolite. Hornblende amphibolite is a massive to foliate rock which mainly consists of fine to medium-grained green and brown Amp + Pl + Qz + Ilm ± Czo/Ep. (Fig. 4a, b, c). Augen amphibolite is comprised of fine to medium-grained green amphibole and fine-grained mineral aggregates (Pl + Qz ± Amp augen) which postdate garnet porphyroblasts. Aggregates after garnet are more or less elongated parallel to the foliation (Fig. 4h, i). Garnet amphibolite is a coarse to medium-grained massive inhomogeneous rock, which shows compositional layering defined by modal variation of Grt, Cpx and Amp. Garnet mode within rocks can vary dramatically at the centimeter scale from 60 vol.% to near zero. (Fig. 4d, e, f, g). Garnet amphibolite exhibits a mineral assemblage of poikiloblastic Grt, Cpx, various generations of calcic Amp, Pl, Qz, Czo/Ep, Ilm, Ap and minor amounts of Rt, Zrn ± Prh ± Pmp ± Bt ± Spn ± sulfides ± Chl. In certain samples sphene occurs in higher proportions. Garnets are usually embedded in a fine-grained symplectitic matrix of tightly intergrown Cpx, Amp and Pl. Various conspicuous reaction textures were observed such as vermicular Cpx-symplectites, coronal reaction bands developed between garnet and symplectitic Cpx and fine grained mineral aggregates after Grt or Cpx. These were clearly caused by retrogression. Garnet is generally rounded with grain sizes of 0.3 – 5 mm. In some cases the approximate location of the original grain boundary of euhedral garnets can be inferred by observation of hexagonal outlines of Pl-Amp aggregates replacing garnet. Pargasitic Amp, albitic Pl, Czo/Ep, Ilm, Ap, Zrn, Rt ± Cpx commonly occur as garnet inclusions. Compared to garnet rims, cores appear lighter in the microscope and are inclusion rich. Occasionally inclusion alignment of snowball structure is observed in garnet cores (Fig. 4g), which is indicative of syntectonic growth. Garnet porphyroblasts show chemical zoning patterns with cores low in X_{Grs}, a sudden increase in X_{Grs} marking Rim1 and a decrease marking Rim2. Zoning patterns and mineral chemistry will be discussed in subsequent chapters. High abundances of sphene are idiosyncratic for sample X36, where big idiomorphic to sub-idiomorphic grains (with lengths of up to 500 µm) occur as matrix minerals and garnet inclusions.

6.1 Reaction-bands between garnet and Cpx-symplectite

50 – 500 µm wide reaction bands separate garnet from fine-grained Cpx-symplectite. Those reaction bands can be divided into 4 zones as is illustrated in Fig. 5 and Fig. 6. Zone 1: intact Grt; Zone 2: coronal textures around Grt (Pl ± Amp); Zone 3: thin layer of zoned amphibole (± Ilm ± Czo/Ep ± Ap); and Zone 4: Cpx-symplectite. Mineral assemblages throughout the reaction-bands become progressively less hydrous towards Grt. Fisher specified the following criteria for recognizing textures generated by diffusion-controlled reactions: "..diffusion-controlled structures characteristically have a strong spatial organization, with well-defined mineral zones showing sharp changes in compositions at zone boundaries, all arranged in an orderly sequence of increasing or decreasing chemical potential" (Fisher., 1977). The coronas around the garnet display a variety of well-organized textures, diagnostic of diffusion-controlled reaction. The most commonly observed coronal textures from Zone 2 are: (1) Pl coronas, (2) vermicular Pl-Amp coronas, (3) vermicular Pl-Amp-Prh coronas, and (4) granular Pl-Qz-Amp coronas surrounding garnet remnants in strongly retrograded samples (X38, X42). Coronas with vermicular textures are radially arranged around garnet grains with internal structures perpendicular to the surface of the garnet. Czo/Ep with grain sizes up to 100 µm sometimes occurs in reaction zones 2 and 3, as well as small (~20 µm) grains of ilmenite. Prominent reaction bands are displayed in Fig. 5 and Fig. 6.

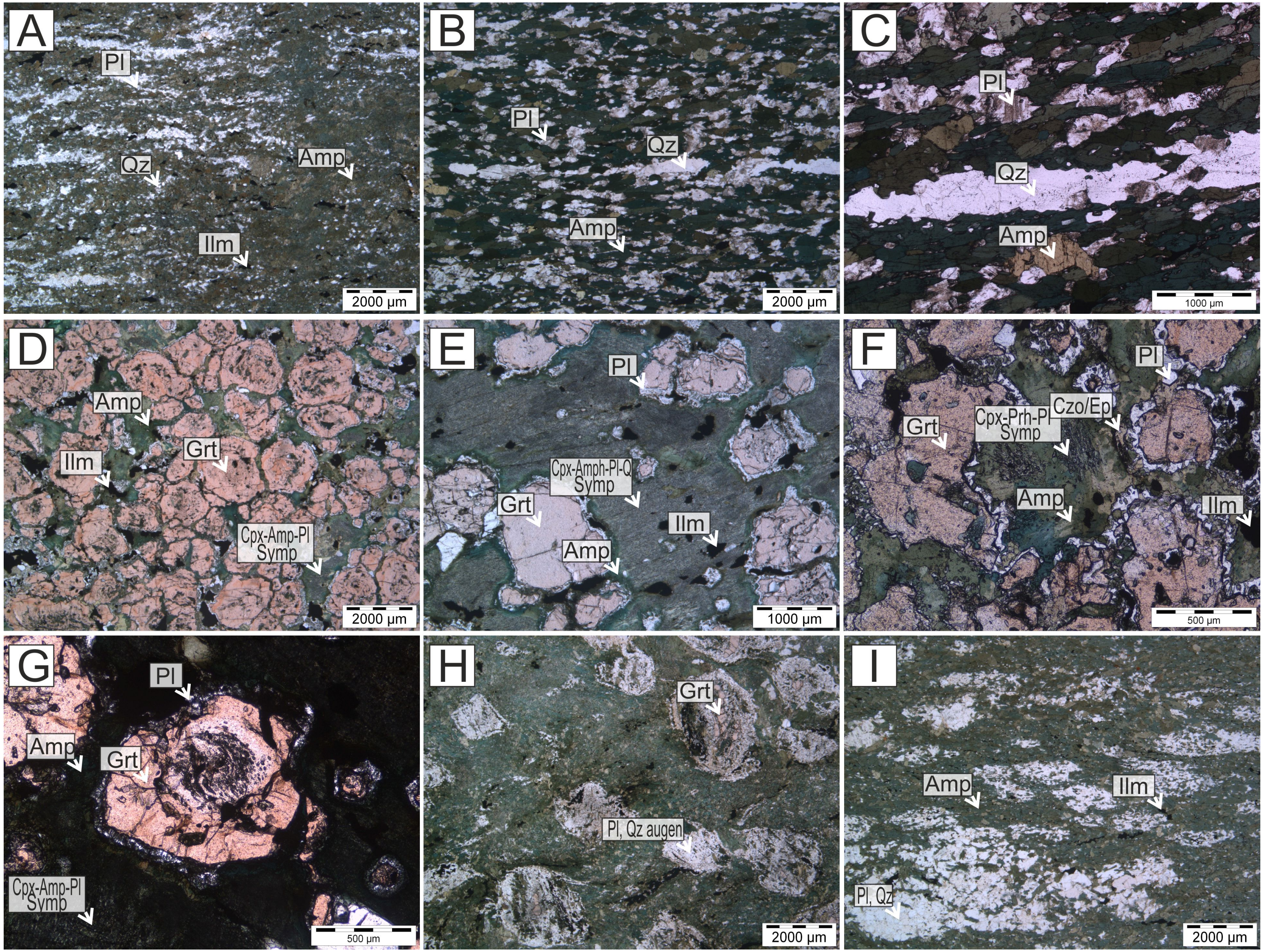

Fig. 4 Photomicrographs of metabasic rocks from the Songshugou metabasic unit. **(A)** Medium to fine grained schistose hornblende amphibolite sampled to the south of peridotitic unit. It mainly consists of green calcic Amp and Pl (white). To lesser amounts mineral phases like Qz, Czo/Ep and Ilm occur. Schistosity is shown by alignment of Pl-Qz layers. Q-Pl aggregates show granoblastic textures. Sample X32. **(B,C)** Coarse-grained schistose hornblende amphibolite from metabasites south of peridotitic unit. Green calcic Amp, Pl and Qz represent major mineral assemblage. To lesser amounts Ilm and Czo/Ep. Alignment of elongated Amp reveals strong schistosity. Qz appears frequently as ~ 300µm wide layers parallel to the alignment of nematoblastic green amphiboles. (Sample X33). **(D, E, F)** Grt-amphibolite consisting mainly of Grt (up to 60 vol.%), Amp and Cpx-symplectite. Garnet grains are subhedral and display 20µm – 200µm wide well organized coronal textures consisting of Pl ± Amp ± Prh ± Ilm ± Czo/Ep. Garnet cores contain many inclusions such as Amp, Ilm, Pl, Qz, Czo/Ep, Ap, Zrn, ± Spn. Rims in general contain fewer inclusions, such as Amp, Ru, Ap, Zrn. Cpx symplectites are rimmed by Amp and show a variety of exsolution textures. D and F are photomicrographs of Sample X37, E of X35. **(G)** Subhedral Grt grain with many inclusions of Amp, Qz, Czo/Ep, Ilm in the core. The rim is almost inclusion free. A Pl-Amp corona of about 50-100µm surrounds the garnet. Snowball texture observed in garnet core indicates synmetamorphic growth. (Sample X35) **(H)** Medium-grained augen amphibolite containing mineral assemblage of Amp, Pl, Grt, Qz to lesser amounts Czo/Ep, Ilm, and as accessory minerals monazite, zr, magnetite. Aggregates of Pl and q have mostly replaced garnet grains. Those aggregates show garnet-like outlines and granoblastic texture. (Sample X39) **(I)** Medium-grained augen amphibolite mainly consisting of Amp, Pl and q. To lesser amounts Ilm, Czo/Ep and sphene occur. In most cases, mineral aggregates of Pl and q have totally replaced preliminary Grt due to retrogression. Nematoblastic Amp grains are aligned along foliation. (Sample X42)

Garnets of sample X35 and X36 exhibit two different types of coronal structures around garnet: **(1)** narrow coronas (20 - 70 µm) which mostly consist of plagioclase (Fig. 5b), **(2)** wide (30 – 150 µm) vermicular Pl + Amp coronas (Fig. 5c,d). Sample X37 shows narrow coronas (20 – 40 µm), which in several cases are only partly evolved, and consist mainly of Pl. Certain coronas also contain prehnite, which always occurs adjacent to albitic Pl and was presumably formed during late stages of retrogression at very low PT conditions (Fig. 5e). Strongly retrograded samples (X38, X42, QS2D), where garnet is heavily or sometimes even entirely consumed, show up to 600 µm wide granular coronas/mineral aggregates of mainly Pl and to lesser extend Amp + Qz ± Ilm ± Czo/Ep (Fig. 5a). Fractures are common in garnet grains and typically filled by calcic Amp (tschermakite and/or hornblende).

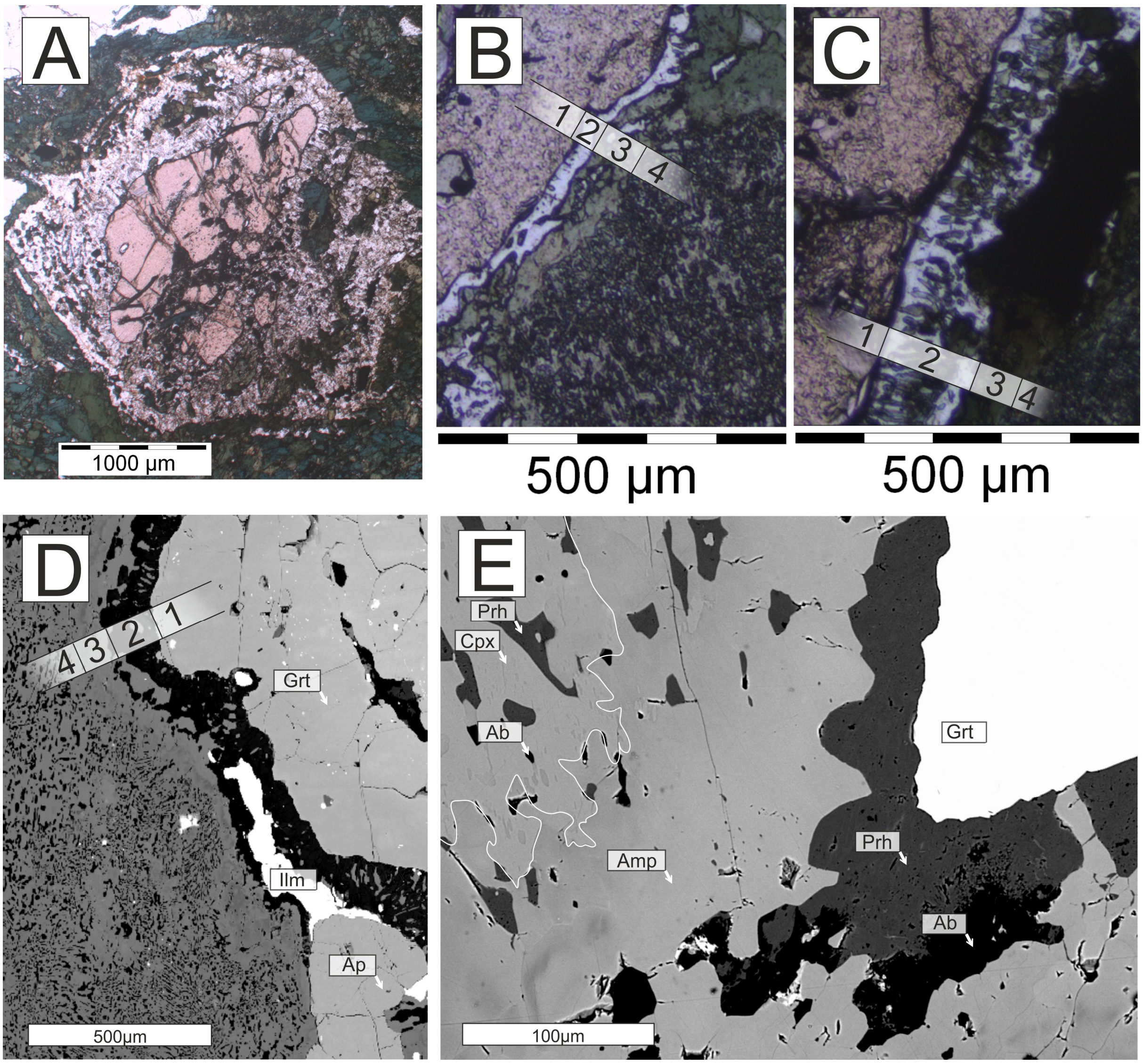

Fig. 5 Photomicrographs and BSE (Backscattered-electron) images of various garnet-omphacite reaction textures observed in Grt-amphibolites. Numerals in graphics divide reaction textures into 4 zones. (1 = Grt, 2 = coronal textures around garnet, 3 = Amp ± Ilm ± Ap ± Czo/Ep, 4 = Cpx-symplectite) **(A)** Photomicrograph of strongly retrograded garnet. Corona comprises mineral aggregates of granular Pl, Amp, Qz, Ilm, Czo/Ep. The approximate location of the original surface of a euhedral garnet grain is marked by hexagonal outlines of Pl-Amp-aggregates. **(B)** Photomicrograph of narrow ~30 µm wide Pl corona around garnet grain. Zone 2 consists of plagioclase and less Amp. Cpx-symplectites in zone 4 comprise very fine-grained ~20 µm Pl and Amp intergrowths evenly distributed. **(C)** Photomicrograph of Pl-Amp corona. Zone 2 is approximately 130 µm wide. Besides Pl, it contains vermicular grains of Amp; aligned perpendicular to the garnets surface. Zone 3 contains up to 500 µm long grains of Ilm (black in photomicrograph). **(D)** BSE image of reaction textures with Ilm and Ap included in zone 3. (E) BSE image. Garnet corona consists of Prh and albitic Pl. Prh is also occurs as intergrowths in nearby Cpx symplectites. Cpx grain is white rimmed for easier distinction. Prh probably evolved during very late stages of retrogression.

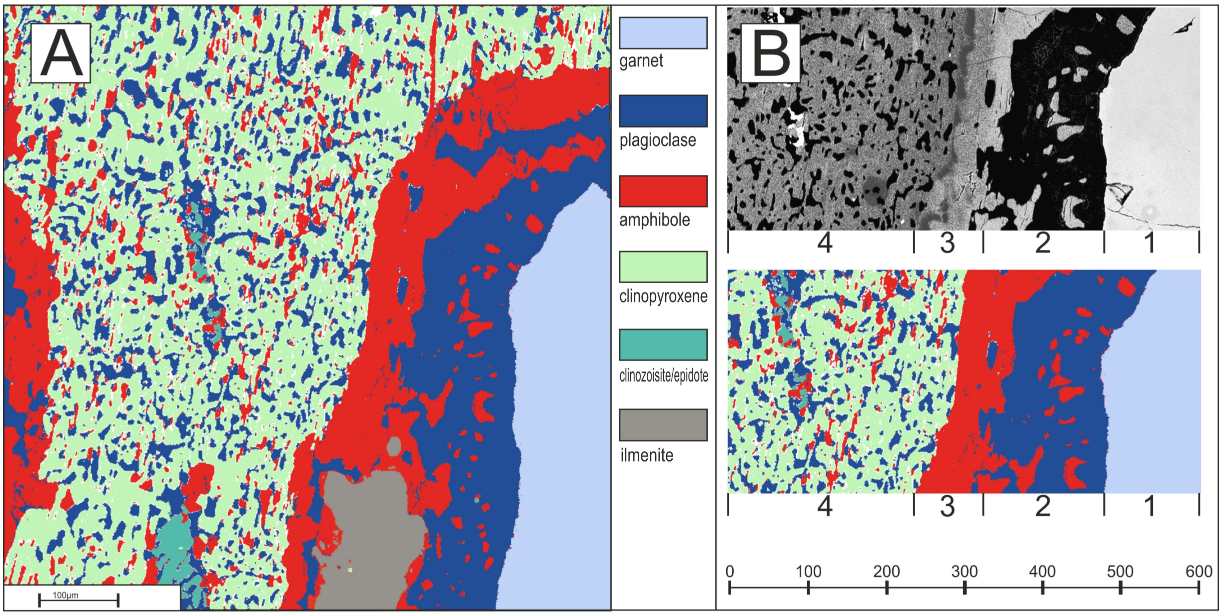

Fig. 6 Mineral map of Cpx-Grt reaction bands. (A) Element distribution images were used to generate mineral maps of Cpx-Grt reaction bands. Modes of intergrowths in Cpx-Pl-Amp symplectite have been calculated by segregating phases according to their specific element distribution signature in X-ray element distribution images; ustilizing the imageJ software package (58.9 vol.% Cpx, 24.4 vol.% Pl and 10.5 vol.% Amp). **(B)** BSE image and mineral map devided into 4 zones. Scale bar in µm at the bottom.

Element distribution images of Cpx-Grt reaction bands reveal chemical zoning of coronal plagioclase and amphibole. The X_{An} component in Pl in zone 2 increases towards Grt (X_{An} = 0.30–0.85). That is clearly displayed in element distribution images by elevated Ca and Al contents, and a drop in Na and Si towards Grt. This distribution pattern coincides with a change in the compositions of the associated amphibole. Na and Al of amphibole in zones 2 and 3 decrease towards Cpx-symp (pargasitic composition close to garnet and Mg-hornblende close to Cpx-symplectite) (Fig. 7). Symplectitic Pl, intergrown Cpx is albite rich with X_{Ab} >0.6. Similar Cpx-Grt reaction bands have been studied in mafic amphibolites of the Liano Uplift of central Texas (Carlson and Johnson.,1991; Wilkerson et al., 1988). Carlson and Johnson propose an open-system diffusion-controlled model for garnet-omphacite reaction bands based on material balance calculations. In quartz-rich regions, they observed an additional zone of Opx between zones 3 and 4. The stability of Opx is strongly regulated by the local activity of silicia in the intergranular fluid. However, Opx was not observed in Songshugou Grt-amphibolites which indicates that silica rich fluids were probably not present or that Opx was totally replaced by Amp during retrogression. The SiO_2 depleted whole rock composition and the absence of Qz in the samples, argue for lower SiO_2 activity in the fluid phase. Prehnite replacing plagioclase in certain coronas and Cpx-symplecitites, indicates retrogression at very low PT conditions which could also contribute to an Opx breakdown in presence of an aqueous fluid in favour of hornblende.

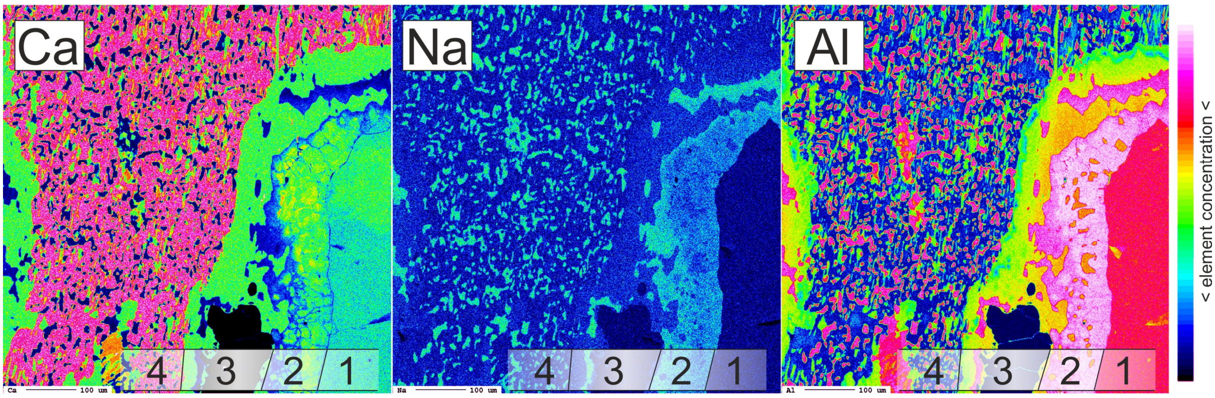

Fig. 7 Element distribution image of Cpx-Grt reaction bands. Pl in zone 2 increases in Na towards zone 3. Amp in zone 3 is richer in Al towards Grt.

Reaction bands between Grt and Cpx-symplectite have possibly arisen by reaction of garnet with omphacitic Cpx during the retrograde stage of metamorphism. This assumption is based upon the observations that in some areas of less retrograded samples (X36), where Cpx is less symplectitic and thus is richer in jadeite component, reaction bands are not always fully developed. Omphacitic Cpx still occurs as stable mineral phase adjacent to Grt.

In sample X37 amphibole is found in different microstructures with unusual Cl-rich composition. It either appears as ~ 20µm wide veinlets that crosscut matrix amphibole or as thin layers along the boundary of Pl-coronae and matrix-amphibole (Fig. 8). Significant Cl contents in amphiboles (2 – 3 wt.%) suggest that chlorine rich fluids attended the vein and corona formation. Hydration reactions in a closed fluid-rock system could lead to Cl richer fluids since Cl partitions strongly into an aqueous fluid relative to OH-bearing minerals. (Kullerud, 1995, 1996). Close to those Cl-amphibole veinlets, $CaCO_3$ occasionally appears as small inclusions in matrix hornblende (Fig. 8B).

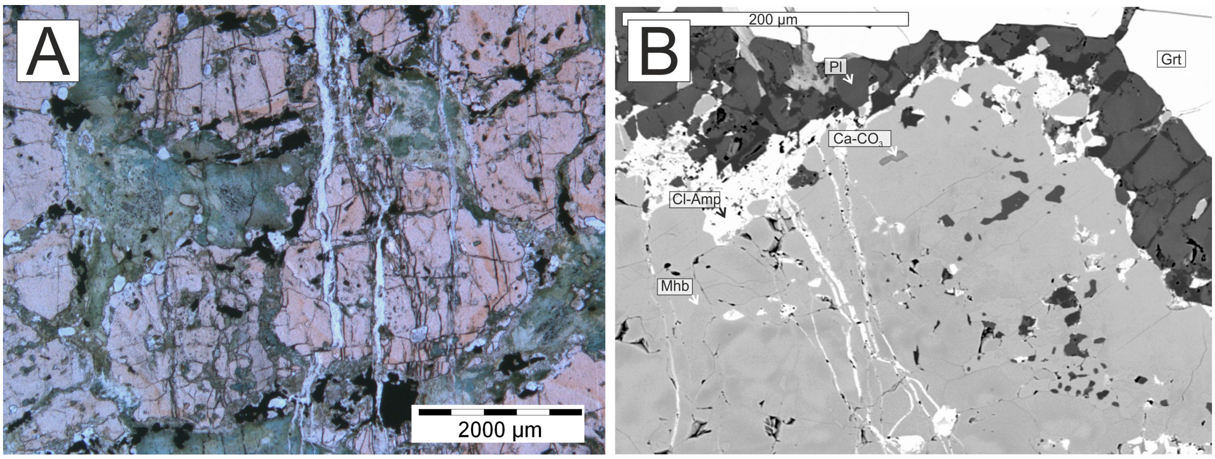

Fig. 8 **(A)** photomicrograph of Grt-amphibolite**.** Veins crosscutting garnet grains. **(B)** BSE image of Grt-amphibolite. Cl-amphibole appears as narrow veinlets crosscutting matrix amphibole and around coronal textures.

6.2 *Clinopyroxene-symplectites*

Symplectites of Cpx + Pl ± Amp ± Qz are evidence of prior eclogite-facies or high-pressure (HP) metamorphism caused by replacement of omphacite by a mineral assemblage of lower density. They commonly occur in metabasites from HP and UHP metamorphic belts; and are usually generated in response to post-peak decompression (Eskola, 1921; Griffin and Raheim, 1973; Wilkerson et al., 1988; O'Brien et al., 1990; Droop et al., 1990; Zhao et al., 2001). All Px found in the matrix exhibit these symplectitic features. Most likely, they developed simultaneously with the Grt-Cpx reaction bands; since both represent hydration and reequilibration at lower pressures. In contrast to Grt-Cpx reactionbands, Cpx symplectites have generated textures without strong spatial organization. They usually appear as larger grains with diameters up to 30 mm and are typically surrounded by Mhb. Various exsolution textures are observed including **(1)** Qz rods, compound inclusions composed of **(2)** Amp + Pl, **(3)** lamellar intergrowths of Pl + Cpx + Amp + Qz, **(4)** Cpx + Pl + Amp + Prh compounds, **(5)** Cpx + Pl + Amp + Pmp + Qz compounds and **(6)** Qz + Pl intergrowths. Most prominent are Pl + Amp intergrowths. There is a positive correlation between the grain size of intergrowths and their abundance. All observed Cpx showed exsolution textures; hence no pristine Cpx composition is preserved. In the literature symplectite-forming reactions are often assumed to behave isochemically; therefore, original Omp compositions are estimated by reintegration of symplectite phases. This assumption is controversial. Several authors postulate that fluid transport plays a major role in facilitating cations at nettransfer reactions, implying open-system behavior at the grain scale (Heinrich, 1982; Messiga and Bettini, 1990; Yang, 2004). Cpx in most symplectites is of diopsidic and augitic composition. Omphacite (X_{Na} = Na/(Na+Ca) = ~0.23) occurs in aggregates with very few intergrowths. Pl in Cpx symplectites (X_{Na} = Na/(Na+Ca) = <0.10) shows X_{Ab} = 0.5-0.8. Various Cpx symplectites occurring in Grt-amphibolites are displayed in Fig. 9.

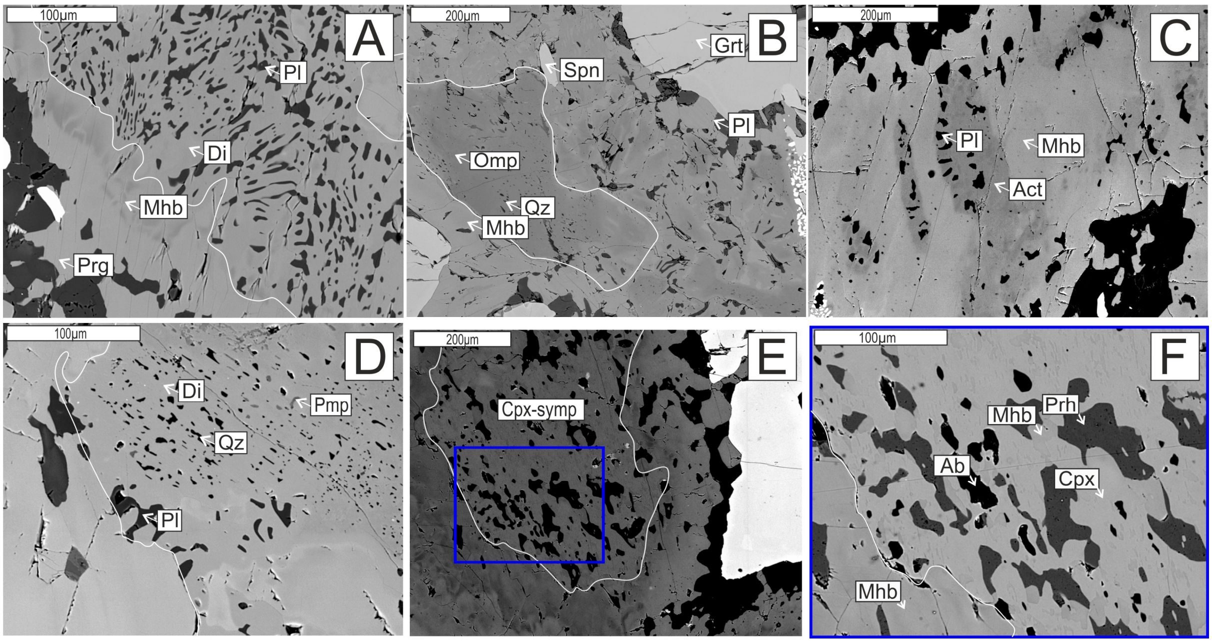

Fig. 9 various Cpx symplectites of metabasic Grt-amphibolites, BSE images. (A) Cpx-Pl-Amp symplectite, the most common type of Cpx exsolution texture found in Songshugou Grt-metabasites. Cpx grain is contoured by a white line. Pl intergrowths (X_{Ab} = 0.5-0.8) have vermicular shapes with lengths from 20 µm to 50 µm. Amp included in symplectite (difficult to distinguish from Cpx on BSE images) is Mg-Hbl. Amp in zone 3 increases in Al and Na and decreases in Si and Mg towards Grt, leading to pargasitic compositions. Cpx is mainly of diopsidic and augitic composition. **(B)** Symplectite with few Qz inclusions. Cpx, outlined by a white line, is of omphacitic composition. Coronas around garnet grains are marginally developed, which indicates less retrogression. **(C)** Amp-Pl symplectite. Actinolite and Pl intergrowths (X_{Ab} = 0.8) surrounded by Mg-Hbl. **(D)** Cpx-Qz-Pl-Pmp-Amp symplectite. Amp, Qz and Pmp appear as ~10µm round to elliptical intergrowths in diopsidic Cpx. Pl intergrowths are bigger in size (30µm – 100µm) and are chiefly observed along the grain boundary to surrounding Mg-hornblende. **(E,F)** Prh-Cpx-Pl-Amp symplectite. Pl is almost pure albite. Prh possibly replaced Pl during late stages of retrogression. Intergrowths of Pl and Prh are of vermicular to round shape with grain lengths up to 90µm.

The matrix assemblage which mainly consists of symplectitic Cpx and Amp also comprises Qz, Ilm, Czo/Ep, Zr ± Spn ±Prh ±Ap as subordinate phases. Sphene occurrence is restricted to certain samples (e.g., X36). Grain shapes are euhedral to subhedral, with grain sizes up to 500 µm. Sphene occurs as Grt inclusions, as well as in the matrix. Matrix Spn commonly shows reaction textures and is partly replaced by symplectites consisting of Ilm + Cpx (Fig. 10).

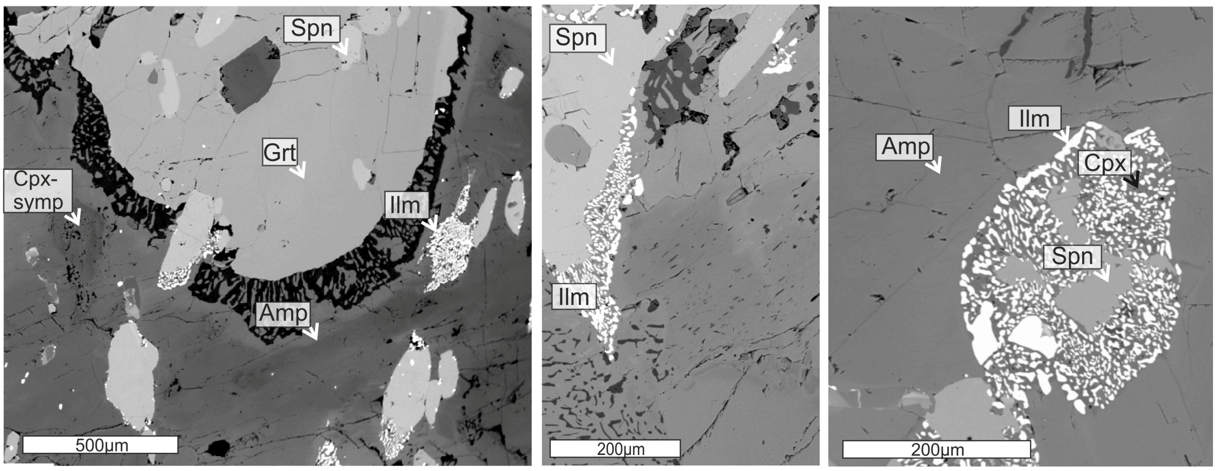

Fig. 10 Spn-Ilm-Cpx exsolution textures

Clinozoisite/epidote appears as Grt inclusions, in the matrix and sometimes included in zone 2 and 3 of Grt-Cpx reaction bands (Fig. 11a). Clinozoisite/epidote grains frequently show compositional zoning, clearly visible in BSE images where Ep rich areas containing REEs appear brighter. Ilmenite occurs included in Grt-cores, in zone 3 of reaction Grt-Cpx reaction bands and as matrix mineral (

Fig. **5**d). Ilmenite included in Grt shows significantly smaller grain size (< 80 µm) compared to grains found in matrix and Grt coronae (up to 600 µm). Apatite is commonly included in Grt as well as in the matrix. Grain shapes are euhedral to subhedral with grain sizes of 30 - 70 µm for grains included in Grt and 50 - 500 µm for matrix Ap (Fig. 11b).

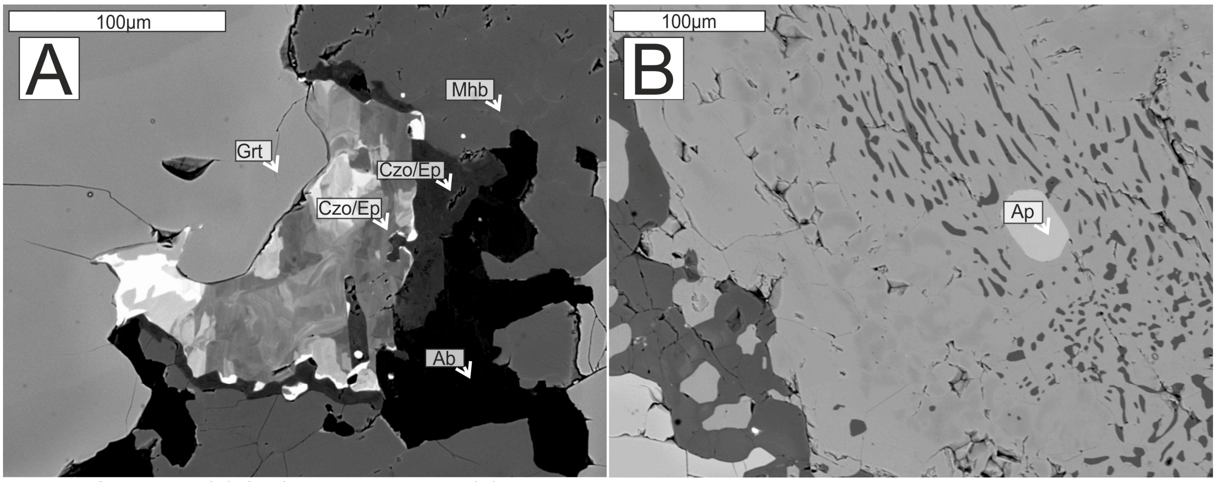

Fig. 11 BSE images (A) Czo/Ep rimming garnet (B) euhedral Ap grain in matrix

7 Mineral chemistry

7.1 Cpx-symplectites

Mineral data was processed using the mathematica based program PET (Dachs, 1998). Pyroxene formulae were calculated on the basis of six oxygens. Fe^{2+} and Fe^{3+} in pyroxene, garnet and Fe-Ti-oxides were calculated according to Droop 1987; and for amphibole, after Leake et al., 1997.

7.1.1 *Cpx-Amp-Pl symplectites*

The Cpx-Amp-Pl symplectite is the most common variety of cpx-symplectites in garnet amphibolites. Diopsidic or augitic Cpx functions as a host for round or vermicular Amp and Pl intergrowths. Plagioclase is Na rich with X_{ab} = 0.6-0.8. Amphibole is Mhb with X_{Mg} ranging from 0.5 to 0.6 and TiO_2 below 0.7 wt.% (Fig. 9a, table 6). Mineral modes of Cpx-Amp-Pl symplectites have been evaluated by analyzing phases according to their specific element distribution signature in X-ray element distribution images with the imageJ software package (Amp: 10.5 vol.%, Cpx: 58.9 vol.%, Pl: 24.4 vol.%). Pristine Cpx composition has been calculated converting the phase volume to wt.% with assumed densities of 2.70 g/cm³ for Pl, 3.23 g/cm³ for Amp and 3.28 g/cm³ for Cpx. Symplectite phase reintegration is only valid if the system behaved isochemically. Representative mineral compositions and reintegrated Cpx composition of Cpx-Amp-Pl symplectites are presented in table 6.

table 6 representative mineral compositions of Cpx-Amp-Pl symplectites.

representative mineral compositions of cpx-amph-plag symplectites													
	amphibole (O=23)				**clinopyroxene (O=6)**			**cpx**		**plagioclase (O=8)**			
Sample	Gt3-50	Gt3-54	3a21	3a26	Gt3-52	Gt3-55	Gt3-56	reintegrated		Gt3-59	Gt3-60	3a25	3c56
Mineral (IMA)		Mg-hornblende				diopside		omph					
SiO_2	45.19	45.59	46.59	48.21	51.77	52.83	53.27	51.02		63.44	62.94	62.37	63.17
TiO_2	0.64	0.57	0.47	0.40	0.17	0.00	0.00	0.34		-	-	-	-
Fe_2O_3	-	-	-	-	-	-	-	-		0.34	0.78	0.38	0.61
Al_2O_3	10.01	8.98	9.00	7.71	1.69	0.67	1.22	11.74		23.28	22.75	23.45	23.31
Cr_2O_3	<0.10	<0.10	<0.10	0.11	<0.10	<0.10	<0.10	<0.10		-	-	-	-
FeO	19.05	19.03	18.98	17.92	11.20	10.83	11.05	14.22		-	-	-	-
MnO	0.18	0.08	0.09	0.13	0.15	0.13	0.13	0.08		-	-	0.10	-
MgO	10.02	10.84	9.55	10.80	12.24	12.75	12.03	9.03		<0.10	0.38	<0.10	<0.10
CaO	11.49	11.71	11.14	11.44	22.50	22.70	22.67	10.84		4.66	6.72	4.98	5.87
Na_2O	2.00	1.71	2.00	1.43	0.69	0.38	0.55	3.06		8.67	7.19	9.04	7.60
K_2O	<0.10	<0.10	<0.10	<0.10	-	-	-	-		-	-	-	-
F	<0.10	0.15	0.36	0.24	<0.10	<0.10	<0.10	0.13		-	-	-	-
Total	**98.58**	**98.66**	**98.18**	**98.39**	**100.41**	**100.29**	**100.92**	**100.46**		**100.39**	**100.76**	**100.32**	**100.56**
Si	6.651	6.687	6.907	7.061	1.934	1.978	1.985	1.874		2.791	2.771	2.760	2.778
Ti	0.071	0.063	0.052	0.044	0.005	0.000	0.000	0.009		-	-	-	-
Al	0.577	0.748	0.378	0.413	0.098	0.043	0.016	0.508		0.011	0.026	0.013	0.020
Fe^{3+}	1.736	1.552	1.573	1.331	0.074	0.030	0.054	-		1.207	1.180	1.223	1.208
Cr	0.000	0.000	0.000	0.013	0.000	0.000	0.000	-		-	-	-	-
Fe^{2+}	1.768	1.586	1.975	1.782	0.252	0.296	0.328	0.437		-	-	-	-
Mn	0.022	0.010	0.011	0.016	0.005	0.004	0.004	0.003		-	-	0.003	-
Mg	2.199	2.370	2.111	2.358	0.682	0.712	0.668	0.495		0.000	0.025	0.000	0.000
Ca	1.812	1.840	1.770	1.795	0.901	0.910	0.905	0.427		0.220	0.317	0.236	0.277
Na	0.571	0.486	0.575	0.406	0.050	0.028	0.040	0.218		0.740	0.614	0.776	0.648
K	-	-	-	-	-	-	-	-		-	-	-	-
F	0.000	0.070	0.169	0.111	0.000	0.000	0.000	0.015		-	-	-	-
SumCat	**15.407**	**15.412**	**15.333**	**15.518**	**3.997**	**3.998**	**4.000**	**3.986**		**4.969**	**4.933**	**5.010**	**4.931**
X_{Mg}	0.554	0.599	0.570	0.517	0.723	0.704	0.671	0.531	X_{Ab}	0.771	0.659	0.765	0.701

7.1.2 *Cpx-Qz ± Pl symplectites*

Cpx-Qz symplectites usually contain less and smaller (~10 µm) intergrowths compared to all other symplectite varieties (Fig. 9b). They can also occur as small areas within Cpx-Pl-Amp symplectites. Minor amounts of albitic Pl do occasionally appear. However, the majority of Cpx is of omphacitic composition close to those of the reintegrated ones from Cpx-Amp-Pl symplectites with X_{Na}=0.20-0.24 and X_{Mg}=0.70-0.85. Representative analyses of Cpx are presented in table 7.

table 7 represantative analyses of Cpx in Cpx-Qz symplectites.

representative analyses of Cpx-Qz symplectites ± Pl						
			clinopyroxene (O = 6)			
Sample	a_3	a_15	a_16	4_29	4_27	4_28
Mineral (IMA)		omphacite			augite	diopside
SiO_2	54.74	54.35	54.38	53.86	53.80	54.07
TiO_2	0.14	< 0.10	< 0.10	< 0.10	< 0.10	0.10
Al_2O_3	3.77	3.80	3.61	3.94	4.10	4.30
FeO	7.51	7.76	7.62	8.31	9.25	8.78
MnO	< 0.10	0.10	< 0.10	< 0.10	< 0.10	< 0.10
MgO	12.03	11.92	11.30	11.07	11.20	11.40
CaO	18.95	19.61	19.36	18.35	18.36	18.87
Na_2O	2.98	3.13	3.30	3.01	2.63	2.59
Total	**100.12**	**100.67**	**99.68**	**98.54**	**99.62**	**100.55**
Si	1.998	1.972	1.994	2.005	1.983	1.974
Ti	0.004	0.000	0.000	0.000	0.002	0.003
Al	0.162	0.162	0.156	0.173	0.178	0.185
Fe^{3+}	0.045	0.114	0.080	0.034	0.083	0.062
Fe^{2+}	0.184	0.121	0.153	0.224	0.203	0.206
Mn	0.000	0.003	0.000	0.000	0.000	0.000
Mg	0.655	0.645	0.618	0.614	0.616	0.620
Ca	0.741	0.762	0.761	0.732	0.725	0.738
Na	0.211	0.220	0.235	0.217	0.188	0.183
SumCat	**4.000**	**3.999**	**3.997**	**4.000**	**4.000**	**4.000**
X_{Mg}	0.781	0.842	0.802	0.733	0.752	0.751
X_{Na}	0.222	0.224	0.236	0.229	0.206	0.199

7.1.3 Cpx-Amp-Prh-Pl symplectites

Cpx-Amp-Prh-Pl symplectites contain diopsidic Cpx with compositions similar to those of Cpx-Amp-Pl symplectites (Fig. 9ef). Pl is rich in X_{Ab} = 0.7-1.0. Green Amp is classified as Mhb with X_{Mg} ~0.6 and low TiO_2 (<0.25 wt.%). The close spatial relation of Pl and Prh indicates that Prh formed after Pl at low PT conditions. Representative mineral compositions are presented in table 8.

table 8 representative analyses of Prh-Cpx-Pl-Amp symplectites

representative analyses of pre-cpx-amph-plag symplectites																
	amphibole (O = 23)				**plagioclase (O = 8)**			**prehnite (O = 11)**						**clinopyroxene (O = 6)**		
Sample	3_6	3_7	3_8		3_10	3_11	3_15	3_1	3_2	3_4	3_9	3_14		X373_3	X373_5	X373_13
Mineral	Mg-hornblende				Pl (X_{Ab} > 0.7)			prehnite						diopside		
SiO_2	50.26	50.35	49.71		69.85	62.08	69.57	44.80	44.80	45.26	45.49	45.83		53.27	53.21	52.95
TiO_2	<0.10	0.16	0.22		-	-	-	-	-	-	-	-		<0.10	<0.10	<0.10
Fe_2O_3	-	-	-		0.35	0.38	0.24	0.79	0.46	0.47	0.71	0.36		-	-	-
Al_2O_3	6.71	5.90	6.89		19.75	24.11	19.89	24.89	24.76	24.83	25.20	25.28		1.05	0.59	0.91
Cr_2O_3	<0.10	<0.10	<0.10		-	-	-	-	-	-	-	-		<0.10	<0.10	<0.10
FeO	17.21	16.52	16.97		-	-	-	-	-	-	-	-		10.92	11.14	10.74
MnO	<0.10	<0.10	0.11		-	-	-	-	-	-	-	-		<0.10	0.13	0.10
MgO	11.80	12.60	11.78		-	-	-	-	-	-	-	-		11.82	12.31	11.26
CaO	11.29	11.24	11.31		0.15	5.20	0.26	25.80	25.56	25.67	25.46	25.46		22.05	22.20	22.05
Na_2O	0.79	0.82	0.88		10.36	7.77	10.17	0.04	0.18	0.07	<0.10	0.16		0.36	0.31	0.45
K_2O	<0.10	0.01	<0.10		<0.10	<0.10	<0.10	-	-	-	-	-		-	-	-
F	0.24	0.33	0.27		-	-	-	-	-	-	-	-		-	-	-
Cl	<0.10	<0.10	<0.10		-	-	-	-	-	-	-	-		-	-	-
Total	**98.3**	**98.18**	**98.48**		**100.46**	**99.54**	**100.13**	**96.32**	**95.76**	**96.3**	**96.86**	**97.09**		**99.47**	**99.89**	**98.46**
Si	7.308	7.323	7.226		3.015	2.754	3.012	3.039	3.052	3.063	3.058	3.070		2.006	2.002	2.016
Ti	0.000	0.018	0.024		-	-	-	-	-	-	-	-		0.001	0.000	0.003
Al	0.275	0.324	0.335		1.005	1.261	1.015	1.990	1.988	1.981	1.997	1.996		0.047	0.026	0.041
Fe^{3+}	1.150	1.011	1.180		0.011	0.013	0.008	0.040	0.024	0.024	0.036	0.018		-	-	-
Cr	0.000	0.000	0.009		-	-	-	-	-	-	-	-		0.002	0.003	0.000
Fe^{2+}	1.818	1.716	1.759		-	-	-	-	-	-	-	-		0.344	0.351	0.342
Mn	0.000	0.000	0.014		-	-	-	-	-	-	-	-		0.003	0.004	0.003
Mg	2.558	2.732	2.553		-	-	-	-	-	-	-	-		0.664	0.691	0.639
Ca	1.759	1.752	1.762		0.007	0.247	0.012	1.875	1.866	1.862	1.834	1.828		0.890	0.895	0.900
Na	0.223	0.231	0.248		0.867	0.668	0.854	0.005	0.024	0.009	0.000	0.021		0.026	0.023	0.033
K	-	-	-		-	-	-	-	-	-	-	-		-	-	-
F	0.110	0.156	0.124		-	-	-	-	-	-	-	-		-	-	-
Cl	-	-	-		-	-	-	-	-	-	-	-		-	-	-
SumCat	**15.201**	**15.263**	**15.234**		**4.905**	**4.943**	**4.901**	**6.949**	**6.954**	**6.939**	**6.925**	**6.933**		**3.983**	**3.995**	**3.977**
X_{Mg}	0.590	0.610	0.590	X_{An}	0.010	0.270	0.010						X_{Mg}	0.660	0.660	0.650
				X_{Ab}	0.990	0.730	0.980						x_{Na}	0.030	0.030	0.040

7.1.4 *Cpx-Qz-Pl-Pmp-Amp symplectites*

Cpx-Qz-Pl-Pmp-Amp symplectites contain diopsidic Cpx, Mhb, Pmp and Pl (X_{Ab} = 0.5 – 0.7) (Fig. 9d). Pumpellyite was presumably formed during late stages of retrogression similar to Prh. Representative mineral analyses are displayed in table 9.

table 9 representative analyses of Cpx-Qz-Pl-Pmp-Amp symplectites

representative analyses of Cpx-Qz-Pl-Pmp-Amp symplectites							
	Pl (O = 8)			**Cpx (O = 6)**		**Pmp (O = 24.5)**	
	s_1	s_5		s_3	s_7	s_2	s_6
Mineral	plagioclase			diopside		pumpellyite	
SiO_2	52.93	59.20		52.82	52.95	37.18	38.65
TiO_2	-	-		0.14	0.17	0.00	0.09
Fe_2O_3	0.48	0.35		-	-	-	-
Al_2O_3	28.73	24.84		2.93	1.87	24.60	24.32
FeO	-	-		10.30	10.37	2.92	3.86
MnO	0.04	0.00		0.11	0.06	0.08	0.00
MgO	0.07	0.00		10.66	11.09	2.17	2.44
CaO	11.96	6.93		21.35	22.03	22.15	20.11
Na_2O	5.89	9.12		1.29	0.86	0.13	0.38
Total	**100.09**	**100.44**		**99.60**	**99.40**	**89.23**	**89.85**
Si	2.407	2.645		1.983	1.996	6.176	6.345
Ti	-	-		0.004	0.005	0.000	0.011
Al	1.540	1.308		0.130	0.083	4.816	4.706
Fe^{3+}	0.016	0.012		-	-	-	-
Fe^{2+}	-	-		0.323	0.327	0.406	0.530
Mn	0.002	0.000		0.003	0.002	0.011	0.000
Mg	0.005	0.000		0.597	0.623	0.537	0.597
Ca	0.583	0.332		0.859	0.890	3.942	3.537
Na	0.519	0.790		0.094	0.063	0.042	0.121
SumCat	**5.072**	**5.087**		**3.993**	**3.989**	**15.930**	**15.847**
XAb	0.471	0.702	xMg	0.649	0.656		
Xan	0.529	0.295	xNa	0.099	0.066		

7.1.5 Mhb-Act-Pl symplectites

Within large Mhb grains, symplectites consisting of Act and albitic Pl (X_{Ab}~0.8) can be observed (Fig. 9c). Representative data of mineral compositions are displayed in table 10. Actinolite, typically abundant at greenschist facies conditions, is generated during the retrograde exhumation path. Chemical compositions of Act and Mhb are plotted in Fig. 13 (Al IV vs. A-site occupancy and Al VI vs. Si plots).

table 10 representative analyses of Amp-Pl symplectites

representative analyses of amph-plag symplectite							
	surrounding amph		**amph symplectite**			**plagioclase intergrowth**	
Sample	x353s_4	x353s_7	x353s_1	x353s_8		x353s_5	x353s_6
Mineral	Mg-horn		actinolite			plagioclase	
SiO_2	46.70	48.62	52.54	52.67		64.33	65.68
TiO_2	0.52	0.37	0.21	0.12		-	-
Fe_2O_3	-	-	-	-		0.69	0.52
Al_2O_3	8.35	6.89	3.94	3.91		22.57	21.35
Cr_2O_3	<0.10	<0.10	<0.10	<0.10		-	-
FeO	18.81	18.11	16.20	16.18		-	-
MnO	0.12	<0.10	<0.10	<0.10		-	-
MgO	10.48	11.30	13.26	13.29		-	-
CaO	11.14	11.27	11.07	11.21		3.81	2.50
Na_2O	1.65	1.60	0.70	0.72		9.25	9.73
F	0.32	<0.10	0.30	<0.10		-	-
Cl	<0.10	<0.10	<0.10	<0.10		-	-
Total	**98.09**	**98.16**	**98.22**	**98.10**		**100.65**	**99.78**
Si	6.895	7.117	7.612	7.615		2.818	2.889
Ti	0.057	0.041	0.023	0.013		-	-
Al	0.543	0.450	0.153	0.169		1.165	1.107
Fe^{3+}	1.453	1.189	0.673	0.667		0.023	0.017
Cr	0.000	0.000	0.000	0.000		-	-
Fe^{2+}	1.779	1.766	1.810	1.788		-	-
Mn	0.015	0.000	0.000	0.000		-	-
Mg	2.308	2.465	2.864	2.865		-	-
Ca	1.762	1.767	1.718	1.737		0.179	0.118
Na	0.471	0.453	0.197	0.202		0.786	0.830
F	0.151	0.000	0.137	0.000		-	-
Cl	0.015	0.000	0.000	0.000		-	-
SumCat	**15.449**	**15.246**	**15.186**	**15.056**		**4.971**	**4.961**
X_{Mg}	0.565	0.583	0.613	0.616	X_{Na}	0.815	0.876
Al(IV)	1.105	0.889	0.394	0.392	X_{Ca}	0.185	0.124
Al(VI)	0.349	0.299	0.279	0.274			

In Fig. 12 Cpx analyses of the various Cpx-symplectites are plotted into the J-Q and the ternary Q-Jd-Aeg diagram. Pyroxen occurring in highly developed symplectites e.g. (Cpx-Amp-Pl, Prn-Cpx-Amp-Pl, Cpx-Qz-Pl-Pmp-Amp) is of diopsidic and augitic composition and plots in the Quad area (Ca-Fe-Mg pyroxenes). Pyroxene of Cpx-Qz ± Pl symplectites, which is considered to be less influenced by retrogression, plots partly as omphacite in the ternary Q-Jd-Aeg diagram along with reintegrated Cpx compositions of Cpx-Pl-Amp symplectites.

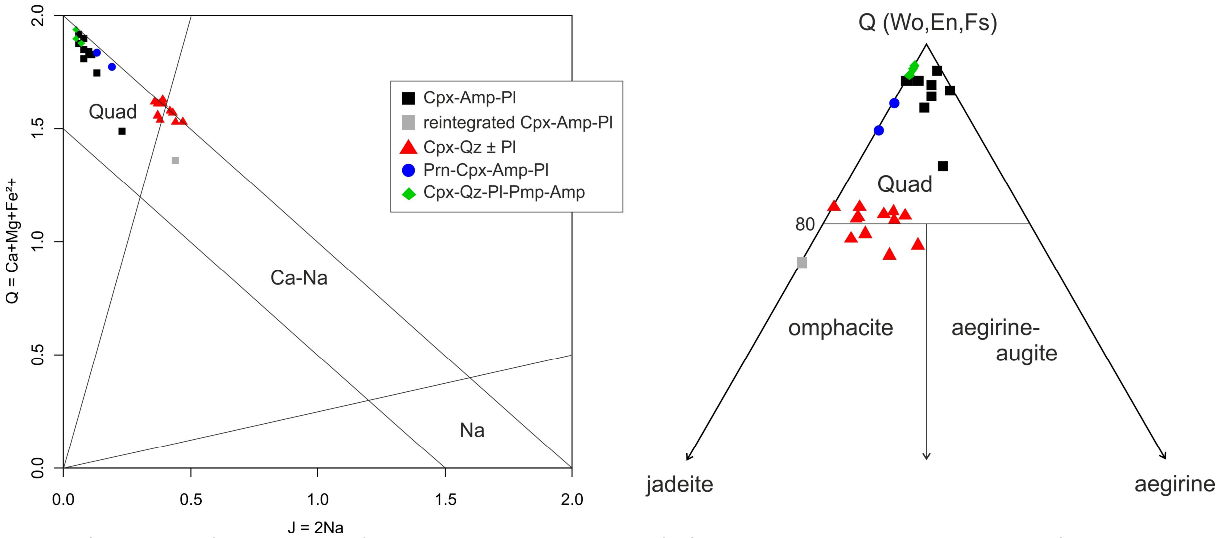

Fig. 12 Q-J diagram for pyroxenes of various symplectites on the left, Q-Jd-Ae ternary diagram on the right. Quad represents the Ca-Mg-Fe pyroxene area. (Morimoto, 1988)

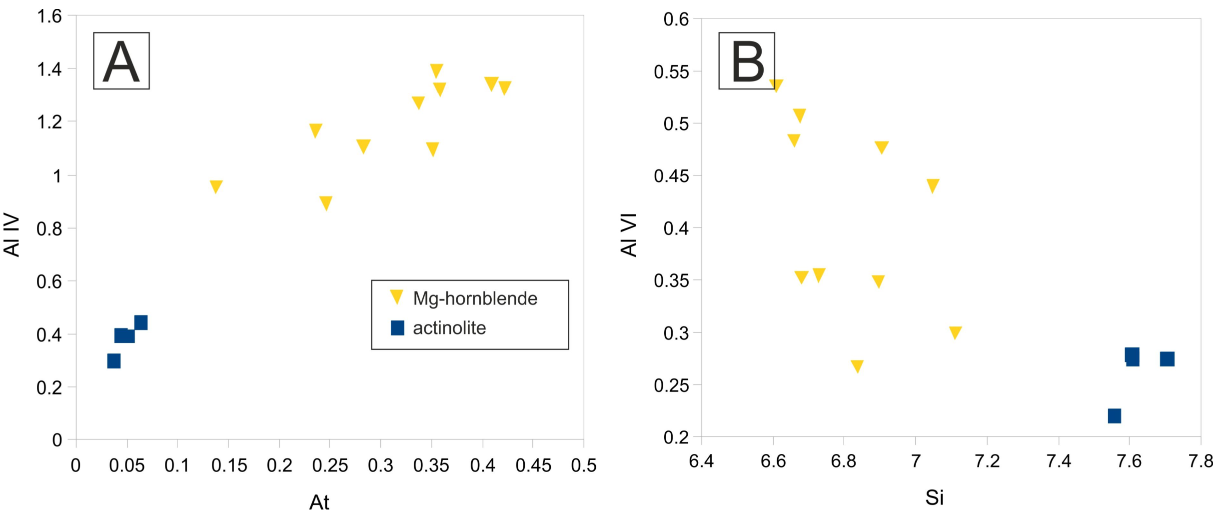

Fig. 13 Amp mineral data plots from Amp-Pl symplectites **(A)** Al IV vs. A-site occupancy, showing compositional gaps between actinolite and hornblende **(B)** Al VI vs. Si showing compositional gaps between actinolite and hornblende.

7.2 Reaction-bands between garnet and Cpx-symplectite

Amphiboles occuring in zone 2 and zone 3 of the Cpx-Grt reaction zones show variation in chemical compostion. Amphibole in zone 2 is of Fe-pargasitic composition. Reaction zone 3, which separates Cpx-symplectite from Grt-corona, consists mainly of Amp, which is compositionally zoned with increasing Al_2O_3 and Na_2O and decreasing SiO_2 towards Grt representing the edenite exchange vector. Thus Mhb compositions occur close to Cpx-symplectite and pargasitic to hastingsitic compositions occur towards garnet. In Fig. 14a the edenite-exchange substitution of Al_{IV}(+) $Na_{(A)}$(+) Si_{IV}(-) is clearly defined by plotting the relevant mineral chemical parameters of different Amp compositions from the reaction rims. Richterite-type substitution effects were eliminated by subtraction of $Na_{(M4)}$ (Czamanske et al., 1981). Consequent substitution of Al $_{IV}$ in tetrahedral sites (T1, T2) is chiefly compensated by partial occupancy of the 10 to 12-fold A-sites by Na; and to lesser amounts K, along with the substitution of Al_{VI} and Ti in octahedral sites (M1, M2, M3 and M4), as displayed by the linear relationship in Fig. 15b. Samples show a slight deficiency in $Al_{IV.}$ That indicates that the excess A-site and octahedral charge is not fully balanced by the Al_{IV} substitution, and might be balanced by the substitution of Na and K by $^{2+}$ charged elements at the M4 site. A binary total alkalis (At) vs. Si plot for chemical classification of amphiboles is displayed in Fig. 15a (Leake 1978). Plagioclase in reaction zone 2 is compositionally zoned, with increasing X_{An} = 0.35-0.85, towards Grt (Fig. 14b). Single idiomorphic grains of Amp, which occasionally appear in the matrix, are Mhb. Cl rich amphibole (Fig. 8) occurs as narrow veinlets crosscutting matrix amphibole and in coronal textures, and is of hastingsitic and pargasitic composition, strongly enriched in Fe, K, Cl, Na and Al compared to surrounding Mhb. Representative mineral analyses of Amp and Pl, in respect of their spatial distribution, are displayed in table 11 and table 12.

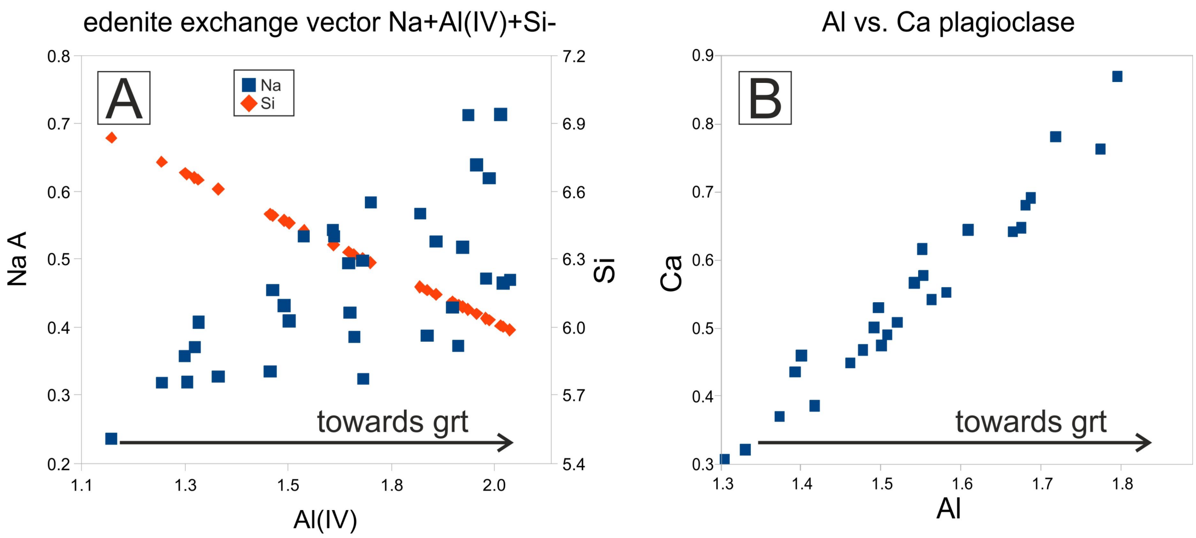

Fig. 14 (A) Al(IV) vs. Na(A) and Si plot of amphiboles occurring in reaction zones 2 and 3. **(B)** Ca vs. Al plot of plagioclase in reaction zone 2.

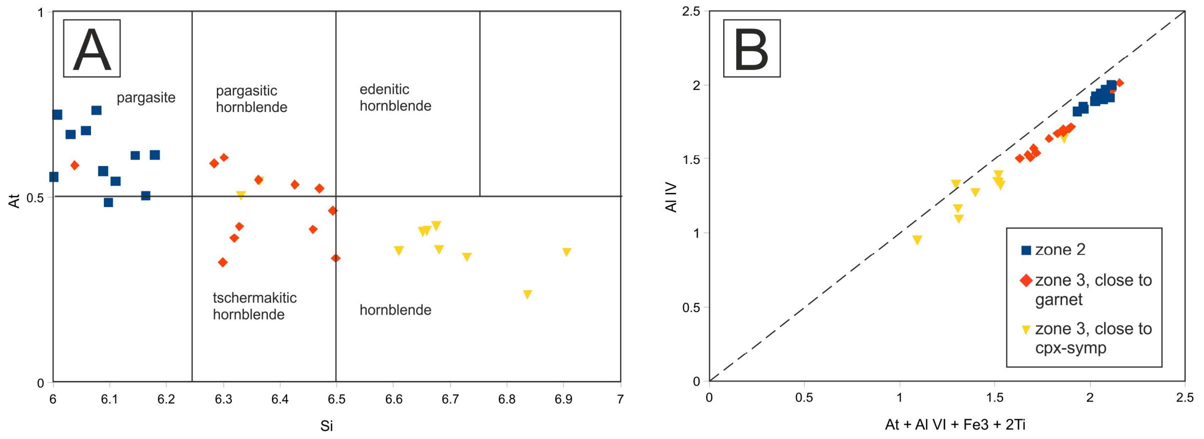

Fig. 15 (A) Binary plot A_{Na+K} vs Si. Nomenclature according to Leake (1978). Different symbols and colours indicate location of amphibole measurements in the reaction zone. **(B)** Plot of Al IV vs At + Al VI + Fe3+ + 2 Ti. Trend line indicates prognosticated values for perfect substitution. Trend line after Czamanske et al. (1981).

table 11 representative analysis of plagioclase in Grt-coronae

representative analysis of Pl (O = 8) of reaction zone 2

Spatial distrib.	**close to Grt**			**middle**		**close to Cpx**
sample	c35	4_40	a_25	Gt3-34	Gt3-40	7g212
SiO_2	49.46	48.72	46.82	56.28	56.64	56.93
Fe_2O_3	0.46	0.58	0.63	0.42	0.37	0.61
Al_2O_3	32.12	33.17	32.98	25.81	26.24	26.74
MnO	0.09	0.00	0.00	0.00	0.00	0.00
CaO	16.05	15.69	17.56	8.88	9.49	8.00
Na_2O	2.73	2.15	1.68	6.76	6.54	7.66
K_2O	0.00	0.00	0.00	0.01	0.00	0.00
Total	**100.91**	**100.63**	**99.67**	**98.18**	**99.31**	**99.97**
Si	2.246	2.212	2.164	2.576	2.565	2.561
Al	1.719	1.775	1.796	1.393	1.401	1.417
Fe^{3+}	0.016	0.020	0.022	0.014	0.013	0.021
Mn	0.003	0.000	0.000	0.000	0.000	0.000
Ca	0.781	0.763	0.870	0.436	0.460	0.386
Na	0.240	0.189	0.151	0.600	0.574	0.668
K	0.000	0.000	0.000	0.001	0.000	0.000
SumCat	**5.006**	**4.972**	**5.002**	**5.020**	**5.015**	**5.054**
X_{Ab}	0.235	0.199	0.148	0.579	0.555	0.634
X_{An}	0.765	0.801	0.852	0.420	0.445	0.366

table 12 representative mineral analysis of amphibole in reaction bands and matrix

representative analysis of amphibole (O = 23)													
	zone 2			zone 3 close to grt			zone 3 close to cpx			Cl-amph veins		matrix	
	d35	d38	c39	Gt3-61	5_30	5_26	d39	c59	4_35	4_26	4_27	4_31	4_24
IMA		Fe-Parg		Fe-Parg		Hast		Mg-Horn		FeParg	Hast	Mg-Horn	
SiO_2	39.79	40.78	40.00	42.63	40.13	39.87	44.46	45.30	45.27	36.88	37.03	49.15	49.52
TiO_2	0.80	0.70	0.73	1.05	0.67	1.18	0.26	0.29	0.32	0.63	<0.10	<0.10	<0.10
Al_2O_3	14.91	14.22	14.85	12.42	15.13	14.91	11.00	9.28	10.54	13.74	10.85	6.30	6.52
Cr_2O_3	<0.10	<0.10	<0.10	<0.10	<0.10	<0.10	<0.10	<0.10	<0.10	<0.10	<0.10	<0.10	<0.10
FeO	20.60	20.16	20.80	19.73	20.03	20.17	20.03	19.48	16.06	27.23	30.57	17.30	17.32
MnO	<0.10	<0.10	<0.10	0.13	0.12	<0.10	0.17	<0.10	<0.10	<0.10	0.15	0.13	0.13
MgO	6.92	7.23	6.93	8.40	7.53	7.70	8.64	9.84	10.92	0.98	1.02	11.92	11.79
CaO	11.83	11.81	11.77	11.52	11.34	11.20	11.75	11.83	11.51	11.16	10.85	11.45	11.57
Na_2O	2.38	2.21	2.48	2.38	2.13	2.21	1.59	1.51	1.75	0.25	0.31	0.87	0.82
K_2O	0.27	0.24	0.21	<0.10	0.60	0.65	0.14	0.10	0.55	3.21	3.39	<0.10	<0.10
F	0.19	0.12	0.16	0.16	0.24	0.16	0.19	0.18	0.23	0.36	0.29	0.24	0.33
Cl	<0.10	<0.10	0.19	<0.10	<0.10	<0.10	<0.10	<0.10	<0.10	2.63	2.85	<0.10	<0.10
Total	**97.69**	**97.48**	**98.12**	**98.43**	**97.91**	**98.04**	**98.22**	**97.81**	**97.15**	**97.06**	**97.31**	**97.36**	**97.99**
Si	6.041	6.179	6.058	6.362	6.038	5.997	6.612	6.737	6.717	6.148	6.239	7.222	7.240
Ti	0.091	0.079	0.084	0.118	0.075	0.134	0.029	0.032	0.036	0.078	0.000	0.000	0.000
Al	2.668	2.539	2.650	2.185	2.683	2.643	1.928	1.627	1.844	2.699	2.154	1.091	1.123
Cr	0.000	0.000	0.000	0.000	0.000	0.000	0.000	0.000	0.000	0.000	0.000	0.000	0.000
Fe^{3+}	0.504	0.443	0.500	0.456	0.659	0.639	0.570	0.610	0.371	0.165	0.659	0.480	0.413
Fe^{2+}	2.112	2.111	2.133	2.006	1.861	1.898	1.921	1.813	1.622	3.632	3.649	1.646	1.705
Mn	0.000	0.000	0.000	0.017	0.015	0.000	0.022	0.000	0.000	0.000	0.022	0.016	0.016
Mg	1.565	1.633	1.563	1.869	1.688	1.726	1.915	2.182	2.415	0.244	0.256	2.611	2.569
Ca	1.925	1.917	1.910	1.843	1.828	1.805	1.872	1.885	1.831	1.994	1.958	1.803	1.812
Na	0.700	0.650	0.729	0.690	0.622	0.645	0.457	0.435	0.503	0.082	0.102	0.248	0.232
K	0.051	0.047	0.041	0.000	0.114	0.124	0.027	0.019	0.103	0.683	0.730	0.000	0.000
F	0.093	0.058	0.077	0.076	0.115	0.077	0.090	0.085	0.109	0.192	0.156	0.112	0.154
Cl	0.000	0.000	0.049	0.000	0.000	0.000	0.000	0.000	0.000	0.742	0.813	0.000	0.000
SumCat	**15.750**	**15.656**	**15.794**	**15.622**	**15.698**	**15.688**	**15.443**	**15.425**	**15.551**	**16.659**	**16.738**	**15.229**	**15.264**
Al(IV)	1.969	1.821	1.942	1.638	1.962	2.013	1.391	1.271	1.325	1.862	1.765	0.790	0.768
Al(VI)	0.695	0.718	0.708	0.547	0.721	0.625	0.535	0.353	0.507	0.833	0.388	0.299	0.353
X_{Mg}	0.426	0.436	0.423	0.482	0.476	0.476	0.499	0.546	0.598	0.063	0.066	0.613	0.601

7.3 Matrix minerals

7.3.1 Apatite

Apatite found in matrix is fluorapatite, with F contents > 1 wt.% and F/Cl > 1. FeO contents in apatites are below 1 wt.% with Ca/P of ~ 1.65. MnO, Na_2O contents are below detection limit of microprobe analysis. Apatite grains show no compositional zoning of major elements. Mineral analysis of matrix apatite is presented in table 13. Trace-element contents of matrix apatites and amphiboles were measured by LA-ICP-MS and are displayed in table 16.

table 13 representative analysis of matrix apatite

representative matrix apatite analysis (O = 25)									
Sample	Gt3-48	Gt3-49	35d_31	35d_32	35c_46	35c_47	35c_48	7g2_20	7g2_21
Mineral					apatite				
P_2O_5	42.27	41.76	42.45	42.50	42.44	42.37	42.63	43.45	42.96
Al_2O_3	0.12	0.18	0.21	<0.10	0.11	<0.10	<0.10	<0.10	<0.10
Cr_2O_3	<0.10	<0.10	<0.10	<0.10	<0.10	0.10	<0.10	<0.10	<0.10
FeO	0.21	0.14	0.38	0.10	0.15	0.36	0.31	0.28	0.05
CaO	56.12	56.30	55.41	55.65	56.11	55.58	55.69	54.14	54.18
F	1.16	1.35	1.49	1.57	1.30	1.45	1.12	1.81	1.95
Cl	<0.10	<0.10	0.16	0.16	0.19	0.19	0.17	<0.10	<0.10
Total	**99.88**	**99.73**	**100.10**	**99.98**	**100.30**	**100.05**	**99.92**	**99.68**	**99.13**
P	5.965	5.926	5.994	6.010	5.978	5.993	6.009	6.123	6.102
Al	0.024	0.036	0.041	0.000	0.022	0.000	0.000	0.000	0.000
Cr	0.000	0.000	0.000	0.000	0.000	0.013	0.000	0.000	0.000
Fe^{2+}	0.029	0.020	0.053	0.014	0.021	0.050	0.043	0.039	0.007
Ca	10.023	10.111	9.901	9.960	10.002	9.949	9.935	9.654	9.739
F	0.612	0.715	0.786	0.829	0.684	0.766	0.590	0.952	1.034
Cl	0.000	0.000	0.045	0.045	0.054	0.054	0.048	0.000	0.000
SumCat	**16.653**	**16.808**	**16.820**	**16.858**	**16.761**	**16.825**	**16.625**	**16.768**	**16.882**

7.3.2 *Sphene*

Sphene occurs as accessory mineral in sample X36. Sphene is compositionally homogenous, without obvious zoning. The Al and Fe contents are relatively low with ~ 0.05 apfu (atoms per formula unit), with small amounts of F. Representative mineral analyses are given in table 14.

table 14 representative analysis of matrix sphene

representative matrix sphene analysis (O = 5)						
	b_23	b_25	4_24	36x4	36x5	36x15
			sphene			
SiO_2	30.77	30.62	30.46	30.89	31.12	31.12
TiO_2	37.97	37.24	38.11	37.26	37.11	37.11
Fe_2O_3	0.53	0.92	0.82	0.97	0.78	0.78
Al_2O_3	1.46	1.81	1.32	1.40	1.82	1.82
Cr_2O_3	0.11	<0.10	0.12	0.11	<0.10	<0.10
MgO	<0.10	<0.10	0.00	0.12	<0.10	<0.10
CaO	27.71	27.63	27.58	27.35	27.13	27.13
F	0.60	0.45	0.38	0.54	0.70	0.70
Total	**99.15**	**98.67**	**98.80**	**98.64**	**98.66**	**98.66**
Si	1.015	1.013	1.007	1.023	1.029	1.029
Ti	0.941	0.927	0.948	0.928	0.923	0.923
Al	0.057	0.071	0.052	0.055	0.071	0.071
Fe^{3+}	0.013	0.023	0.020	0.024	0.019	0.019
Cr	0.003	0.000	0.003	0.003	0.000	0.000
Mg	0.000	0.000	0.000	0.006	0.000	0.000
Ca	0.979	0.980	0.977	0.970	0.961	0.961
F	0.063	0.047	0.040	0.056	0.073	0.073
SumCat	**3.071**	**3.061**	**3.047**	**3.065**	**3.076**	**3.076**
$Al+Fe^{3+}$	0.070	0.094	0.072	0.079	0.090	0.090

7.3.3 *Clinozoisite/epidote, Chlorite, Ilmenite*

Czo/Ep occurs in reaction zone 2, as well as in matrix; and shows compositional zoning. Brighter zones in BSE images probably contain substantial amounts of REEs (Fig. 11a). All epidote compositions belong to the clinozoisite/epidote solid solution series. The pistacite content ($Fe^{3+}/(Fe^{3+}+Al)$), varies from 15 to 30%. Small grains of chlorite (~ 20 µm) rarely occur around Grt in reaction zone 2 and are of Fe-rich chamositic composition. Ilmenite contains minor amounts of MnO and MgO. Fe^{3+} Recalculation for ilmenite was carried out according to Droop (1987). Representative mineral analyses are displayed in table 15.

table 15 representative analyses of matrix Czo/Ep, Chl and Ilm.

representative analyses of Czo/Ep (O = 12.5), Chl (O = 14), Ilm (O = 3)						
	X375_10	37g3_12	Gt3-33	x37g221	x353c9	x353c10
mineral	clinozoisie epidote		chlorite		ilmenite	
SiO_2	38.93	34.97	26.33	0.25	0.28	0.27
TiO_2	0.00	0.00	0.00	51.52	51.37	51.05
Al_2O_3	30.35	20.93	19.56	-	-	-
Fe_2O_3	5.36	12.13	-	-	-	-
V_2O_3	-	-	-	<0.10	0.37	0.50
FeO	-	-	30.96	47.97	47.42	47.57
MnO	-	-	<0.10	0.41	0.57	0.67
MgO	<0.10	0.55	11.47	0.19	0.29	0.00
CaO	23.26	18.93	0.16	0.08	0.10	0.16
F	<0.10	0.30	-	0.46	-	-
Total	**97.9**	**87.8**	**88.6**	**100.4**	**100.4**	**100.2**
Si	2.995	3.084	2.827	0.006	0.007	0.007
Ti	0.000	0.000	0.000	0.953	0.967	0.965
Al	2.752	2.175	2.475	0.000	0.000	0.000
Fe^{3+}	0.310	0.805	0.000	0.153	0.044	0.047
V	0.000	0.000	0.000	0.000	0.007	0.010
Fe^{2+}	0.000	0.000	2.780	0.834	0.949	0.953
Mn	0.000	0.000	0.000	0.009	0.012	0.014
Mg	0.000	0.072	1.836	0.007	0.011	0.000
Ca	1.917	1.789	0.018	0.002	0.003	0.004
F	0.000	0.084	0.000	0.036	0.000	0.000
CatSum	**7.974**	**7.993**	**9.932**	**1.847**	**2.007**	**2.008**

7.4 *Trace elements and REE of matrix amphibole and apatite*

Trace elements and REEs of matrix apatite and amphibole were measured with LA-ICP MS. REE were normalized to chondritic values after Nakamura, 1974. Apatite contains minor amounts of Mn (900 ppm), Sr (60 – 110 ppm) and Y (< 220 ppm) and displays REE abundances of $\sum REE_N$ 200 – 260 with REE patterns peaking at Tb. Concerning chondrite normalized REE patterns, no Eu or Ce anomaly can be located (Fig. 16). Amphibole contains variable amounts of REE with abundances of $\sum REE_N$ from 60 to 130. Chondrite normalized REE patterns display ascending LREEs (Eu_N/La_N = 20 – 27). Cr contents are fairly low with ~20 ppm. Low LREE concentrations in matrix Amp could be due to the presence of Ep, Spn and Ap which preferably partition LREEs. Representative trace element analysis of matrix Amp and Ap are shown in table 16.

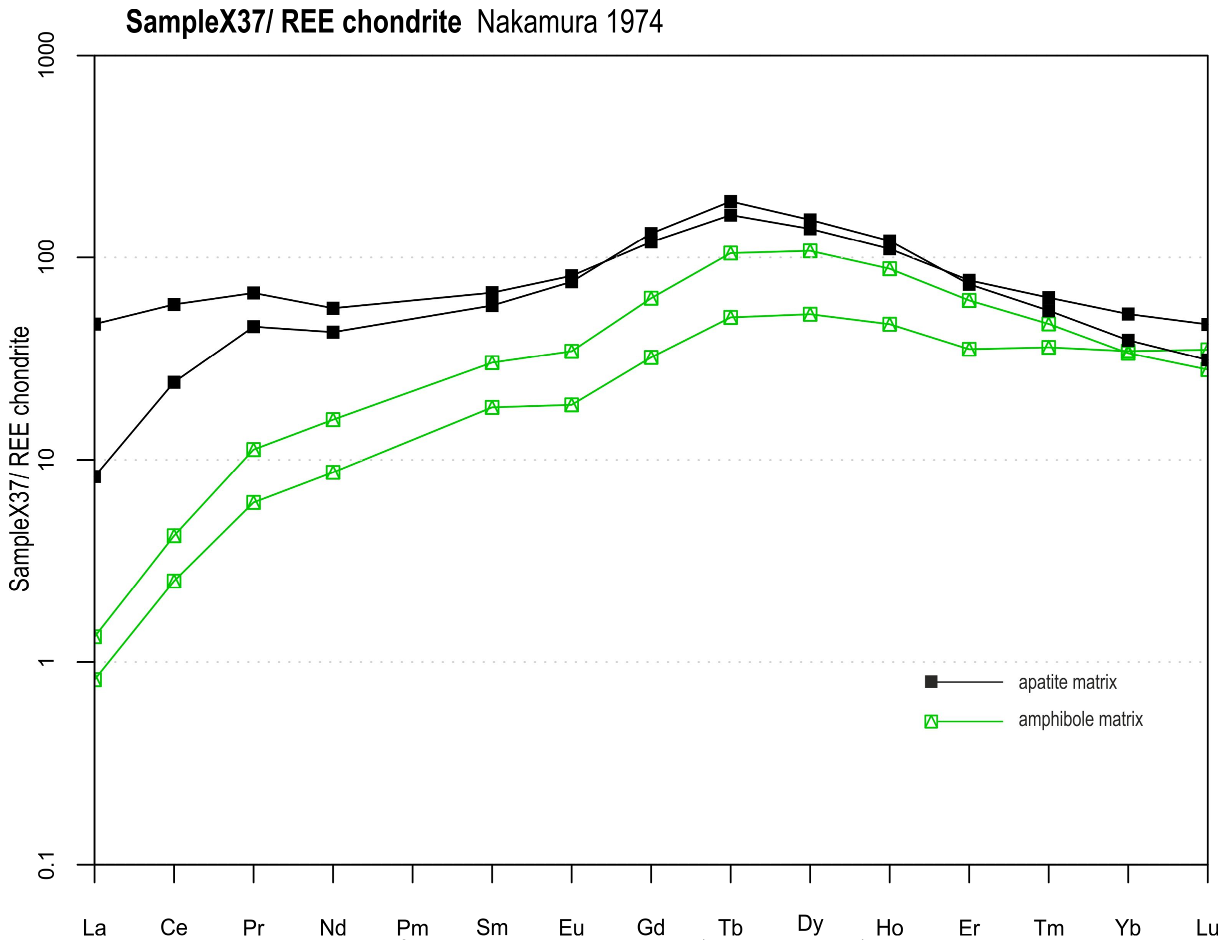

Fig. 16 chondrite normalized REE plot of matrix amphibole and apatite (Nakamura 1974)

table 16 trace element concentrations of matrix apatite and amphibole, quantified by LA-ICPMS

Trace element concentrations of matrix apatite and amphibole				
	apatite		amphibole	
Sample	059XS48	062XS51	060XS49	061XS50
^{7}Li	55.5	1.37	2.39	7.45
^{9}Be	<0.05	0.07	0.38	0.76
^{49}Ti	45.9	37.8	348	646
^{51}V	5.25	7.44	240	180
^{53}Cr	0.77	1.89	18.6	19.4
^{55}Mn	829	756	1110	806
^{59}Co	17.6	3.60	56.4	60.7
^{60}Ni	11.9	6.37	50.2	40.1
^{66}Zn	38.9	19.0	178	180
^{71}Ga	3.63	1.89	8.69	12.77
^{85}Rb	0.06	0.26	0.24	0.68
^{88}Sr	101	68.6	2.49	4.73
^{89}Y	201	199	80.0	141
^{90}Zr	37.0	4.29	51.8	20.3
^{93}Nb	<0.05	<0.05	1.81	0.71
^{133}Cs	0.22	0.06	0.27	0.45
^{137}Ba	0.69	1.33	1.91	9.64
^{139}La	15.5	2.73	0.27	0.44
^{140}Ce	50.7	20.9	2.18	3.65
^{141}Pr	7.48	5.10	0.69	1.26
^{146}Nd	35.4	27.0	5.47	9.96
^{147}Sm	13.6	11.8	3.69	6.14
^{153}Eu	6.25	5.84	1.44	2.65
^{157}Gd	32.9	36.3	8.86	17.37
^{159}Tb	7.63	8.92	2.38	4.94
^{163}Dy	47.6	52.7	18.0	37.0
^{165}Ho	7.72	8.46	3.28	6.16
^{166}Er	17.4	16.6	7.93	13.8
^{169}Tm	1.90	1.64	1.08	1.41
^{172}Yb	11.6	8.59	7.58	7.41
^{175}Lu	1.59	1.06	1.19	0.95
^{178}Hf	1.74	0.32	1.10	0.80
^{181}Ta	<0.05	0.05	0.07	0.05
^{208}Pb	2.46	2.76	0.64	1.47
^{232}Th	0.11	0.12	<0.05	<0.05
^{238}U	0.98	1.51	<0.05	<0.05

All values are reported in ppm

8 Garnet Chemistry and Zoning Patterns

Garnet is considered as a valuable mineral, since its composition shows a very sensitive response to pressure and temperature changes; but also, because cation diffusion functions sufficiently slow to preserve compositional differences within a grain at PT conditions below granulite facies. Growth zoning essentially depends on temperature, pressure, growth rate and the interaction with surrounding matrix minerals that are in equilibrium with the garnets surface (Spear, 1993; Menard and Spear, 1993). Therefore studying chemical zoning of garnet grains can reveal important information in order to reconstruct the rock's evolutionary history. Within the garnet amphibolite of the Songshugou metabasic unit, garnets play an important role in understanding the evolutionary history, since it is the only mineral which remained mostly unaltered during retrogression. In general, Grt of the Songshugou metabasic unit is almandine-rich (X_{Alm} > 0.55). Most grains show a characteristic chemical zoning pattern, particularly remarkable in X_{Grs}, which depicts a sharp boundary between Grt core and rim1 with an abrupt rise, and between rim1 and rim 2 with a sharp decline. Cation-diffusion experiments investigating cations that occupy the dodecahedral X site of garnet such as Mn, Mg, Fe and Ca have shown that volume diffusion of Ca in Grt functions remarkably slower (by an approximated factor of 5) than volume diffusion of Mg, Fe, and Mn, not least because of the larger ionic size of Ca. (Chakraborty and Ganguly 1991; Tracy 1992, Schwandt et al., 1996). Therefore distribution of Ca and other slow diffusing trace elements such as Y and P offer a convenient way to identify and determine compositional zones throughout Grt grains. Steep compositional gradients observed in the zoning pattern are diagnostic of discontinuous growth, and permit to subdivide garnets of the Songshugou metabasic unit into 3 distinctive compositional zones: Core, Rim1, and Rim2. Sluggish element supply to the garnets surface could cause growth interruption, and consequently steep compositional gradients (Spear and Daniel, 2001). Representative garnet analysis from the different growth zones of the least retrogressed samples X35, X36 and X37 are given in table 17, table 18 and table 19. X_{Sps} decreases from core to rim. In sample X35 a drop in X_{Sps} is observed at the core rim boundary. In X37 X_{Sps} contents are low with X_{Sps} <0.26 and show flat distributions. Garnet cores are approximately homogeneous with X_{Alm}~0.60 in X35 and X37 and X_{Alm}~0.53 in X36, X_{Prp}~0.10 in X35 and X37 and X_{Prp}~0.15 in x36 and X_{Grs} =0.23–0.28. Rim1 exhibits a remarkably high plateau in X_{Grs} =0.29–0.35. Rim2 has similar composition to garnet core but significantly less X_{Sps}. In sample X35 X_{Prp} increases towards rim, in some cases stepwise in others gradually, in the contrary to X36 and X37 where X_{Prp} decreases in rim1 and increases in rim2. The most conspicuous feature is the abrupt increase of X_{Grs} between core and rim1, and the drop of X_{Grs} between rim1 and rim2; which is ubiquitously in all garnets. Ternary Fe^{2+} - Ca – Mg plots in Fig. 17 illustrate chemical differences of garnet zones. In general, FeO contents of garnet from sample X36 are ~ 3 wt.% lower than in X35 and X37, reflecting its different chemical composition.

Garnet zoning profiles and 2D X-ray element distribution maps were produced to reveal characteristic zoning patterns of major elements in garnet. Trace elemental data along transects across selected garnet grains was obtained by LA-ICPMS. Garnet zoning profiles of samples X35, X36 and X37 are presented in Fig. 18. Garnet grains from sample X37 show a Mn enrichment at the outmost area of the outer rim which might indicate garnet resorption during retrogression where Mn is retained or re-enters the residual garnet.

table 17 representative garnet mineral analysis of sample X35

sample X35, representative garnet mineral analysis (O = 13)						
	core		**rim1**		**rim2**	
sample	14	15	6	7	xd4	xd33
SiO_2	37.88	37.68	38.17	37.99	38.14	37.85
TiO_2	0.15	0.18	<0.10	0.19	<0.10	<0.10
Al_2O_3	20.91	20.89	20.86	20.73	20.65	20.09
FeO	28.10	28.04	27.30	27.03	28.97	29.91
MnO	1.82	3.58	0.69	0.98	0.29	0.77
MgO	2.81	2.18	3.12	2.94	4.30	3.11
CaO	8.45	8.28	10.61	10.36	7.42	7.90
Total	**100.12**	**100.83**	**100.84**	**100.22**	**99.78**	**99.63**
Si	3.003	2.983	2.988	2.995	3.012	3.019
Ti	0.009	0.011	0.000	0.011	0.000	0.000
Al	1.954	1.949	1.925	1.926	1.922	1.889
Fe^{2+}	1.840	1.794	1.688	1.720	1.858	1.922
Fe^{3+}	0.023	0.062	0.099	0.062	0.055	0.073
Mn	0.122	0.240	0.046	0.065	0.019	0.052
Mg	0.332	0.257	0.364	0.346	0.506	0.370
Ca	0.718	0.702	0.890	0.875	0.628	0.675
SumCat	**8.001**	**7.998**	**8.000**	**8.000**	**8.000**	**7.996**
X_{Alm}	0.611	0.599	0.565	0.572	0.617	0.637
X_{Grs}	0.238	0.235	0.298	0.291	0.209	0.224
X_{Prp}	0.110	0.086	0.122	0.115	0.168	0.123
X_{Sps}	0.041	0.080	0.015	0.022	0.006	0.017

table 18 representative garnet mineral analysis of sample X36

sample X36, representative garnet mineral analysis (O = 13)						
	core		**rim1**		**rim2**	
sample	62	67	111	125	1133	1120
SiO_2	38.16	38.39	38.57	38.13	38.53	38.63
TiO_2	<0.10	<0.10	0.26	<0.10	0.10	<0.10
Al_2O_3	20.74	21.36	20.39	20.62	20.74	21.25
FeO	24.95	25.05	23.99	24.54	25.93	25.15
MnO	2.87	2.33	0.98	0.23	0.70	0.22
MgO	3.85	3.97	3.26	3.83	3.78	3.79
CaO	9.13	9.17	12.25	11.45	10.53	10.63
Total	**99.79**	**100.28**	**99.70**	**98.80**	**100.31**	**99.76**
Si	3.010	3.004	3.035	3.000	3.035	3.016
Ti	0.000	0.000	0.015	0.002	0.015	0.000
Al	1.928	1.970	1.891	1.912	1.891	1.923
Fe^{2+}	1.594	1.618	1.570	1.460	1.570	1.579
Fe^{3+}	0.052	0.022	0.009	0.155	0.009	0.045
Mn	0.192	0.154	0.065	0.015	0.065	0.015
Mg	0.453	0.463	0.382	0.449	0.382	0.452
Ca	0.772	0.769	1.033	0.965	1.033	0.970
SumCat	**8.000**	**8.000**	**8.000**	**7.958**	**8.000**	**7.989**
X_{Alm}	0.529	0.539	0.515	0.505	0.515	0.524
X_{Grs}	0.256	0.256	0.339	0.334	0.339	0.322
X_{Prp}	0.150	0.154	0.125	0.155	0.125	0.150
X_{Sps}	0.064	0.051	0.021	0.005	0.021	0.005

table 19 representative garnet mineral analysis of sample X37

sample X37, representative garnet mineral analysis (O = 13)						
	core		**rim1**		**rim2**	
sample	57	5_1	149	153	1143	1119
SiO_2	37.97	37.63	38.02	37.70	37.87	38.16
TiO_2	<0.10	<0.10	0.28	0.31	<0.10	<0.10
Al_2O_3	20.49	20.05	19.33	19.14	20.65	20.82
FeO	28.10	27.34	27.65	27.56	28.78	28.22
MnO	1.16	2.78	1.06	1.04	0.82	0.86
MgO	2.51	2.06	2.62	2.67	2.97	3.85
CaO	9.74	9.15	11.98	12.11	8.53	8.41
Total	**99.99**	**99.09**	**100.94**	**100.53**	**99.68**	**100.39**
Si	3.015	3.028	2.989	2.975	3.013	2.999
Ti	0.006	0.000	0.017	0.018	0.000	0.000
Al	1.913	1.963	1.791	1.780	1.937	1.929
Fe^{2+}	1.651	1.649	1.619	1.586	1.879	1.783
Fe^{3+}	0.046	0.000	0.199	0.233	0.037	0.072
Mn	0.046	0.015	0.071	0.070	0.055	0.057
Mg	0.441	0.443	0.307	0.314	0.352	0.451
Ca	0.883	0.893	1.009	1.024	0.727	0.708
SumCat	**8.000**	**7.990**	**8.000**	**8.000**	**8.000**	**8.000**
X_{Alm}	0.547	0.550	0.539	0.530	0.624	0.595
X_{Grs}	0.292	0.298	0.336	0.342	0.241	0.236
X_{Prp}	0.146	0.148	0.102	0.105	0.117	0.150
X_{Sps}	0.015	0.005	0.024	0.023	0.018	0.019

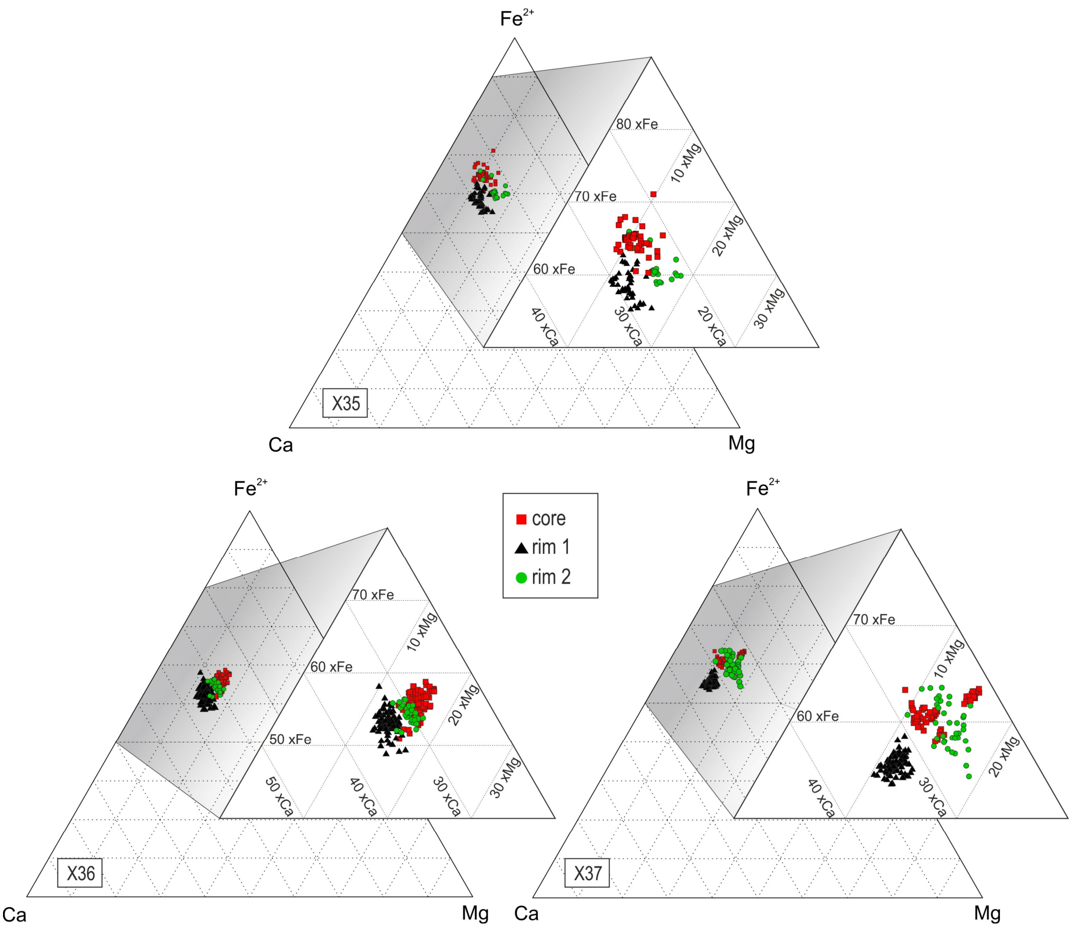

Fig. 17 ternary Fe^{2+} - Ca - Mg plot of garnets. XFe = 100* $Fe^{2+}/(Fe^{2+}$ + Ca + Mg); XCa = 100*Ca/(Fe^{2+} + Ca + Mg); XMg = 100* Mg/(Fe^{2+} + Ca + Mg). Red, black and green symbols represent garnet core, rim1 and rim2 compositions.

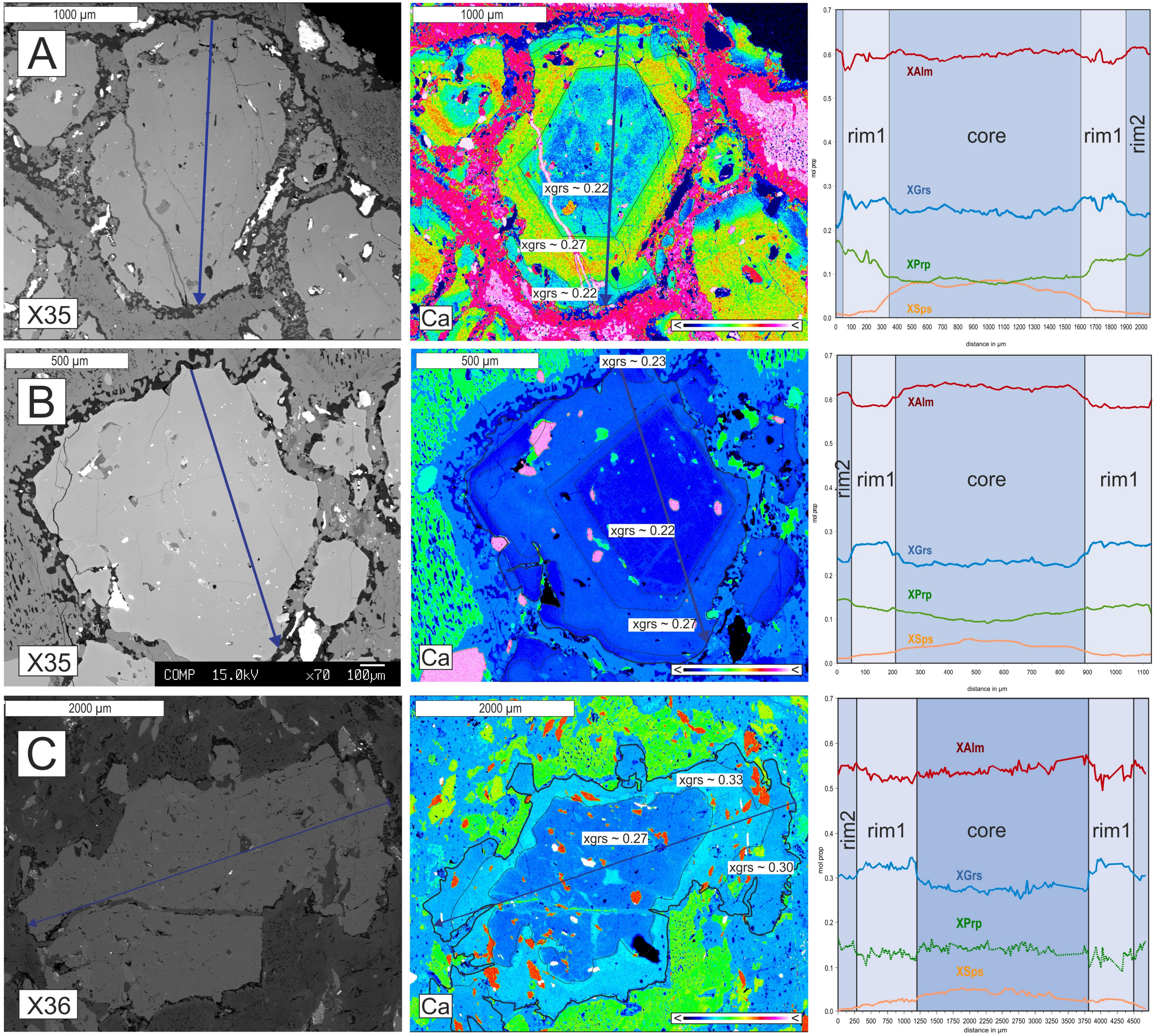

Fig. 18 Various garnet zonation profiles of garnet amphibolite samples, X35, X36 and X37. From left to right: BSE image, Ca-distribution image and profile are displayed. Profile line is drawn into BSE and Ca-distribution image. Garnet grains of Ca-distribution images were contoured for easier differentiation between garnet grain and matrix minerals. **(A)** Garnet profile of sample X35. X_{Sps} is enriched in core with values of ~ 0.09 and decreases with a steep compositional gradient at the core-rim1 boundary before continuously decreasing at a remarkably lower gradient. X_{Grs} shows enrichment in rim1, which is the most prominent feature in garnet zonation profiles and appears ubiquitous in all measured garnet profiles. X_{Alm} has almost constant values throughout the whole garnet profile with a slight moat in rim1. X_{Prp} increases stepwise at core – rim1 boundary and rim1 - rim2 boundary. **(B)** Sample X35. Garnet zoning pattern is very similar to profile A, with the characteristic X_{Grs} plateau in rim1. X_{Alm} shows an inverse X_{Grs} pattern with a compositional moat marking rim1. This might be caused by less overall MnO in the garnets chemistry, and therefore less X_{Sps} in the core. In contrast to profile A, where X_{Prp} increases stepwise, it increases in a continuous manner. **(C)** Garnets of rock sample X36 contain lower amounts of FeO, resulting in lower X_{Alm} contents around 0.55 instead of 0.60 which is oberserved in the garnet compositions of samples X35 and X37. X_{Sps} shows a roughly bell shaped distribution. X_{Grs} component is commonly elevated compared to X35 profiles, and displayes the same plateau like patterns in rim1. Differently to X35 profiles, X_{Prp} decreases in rim1 before it increases again in rim2.

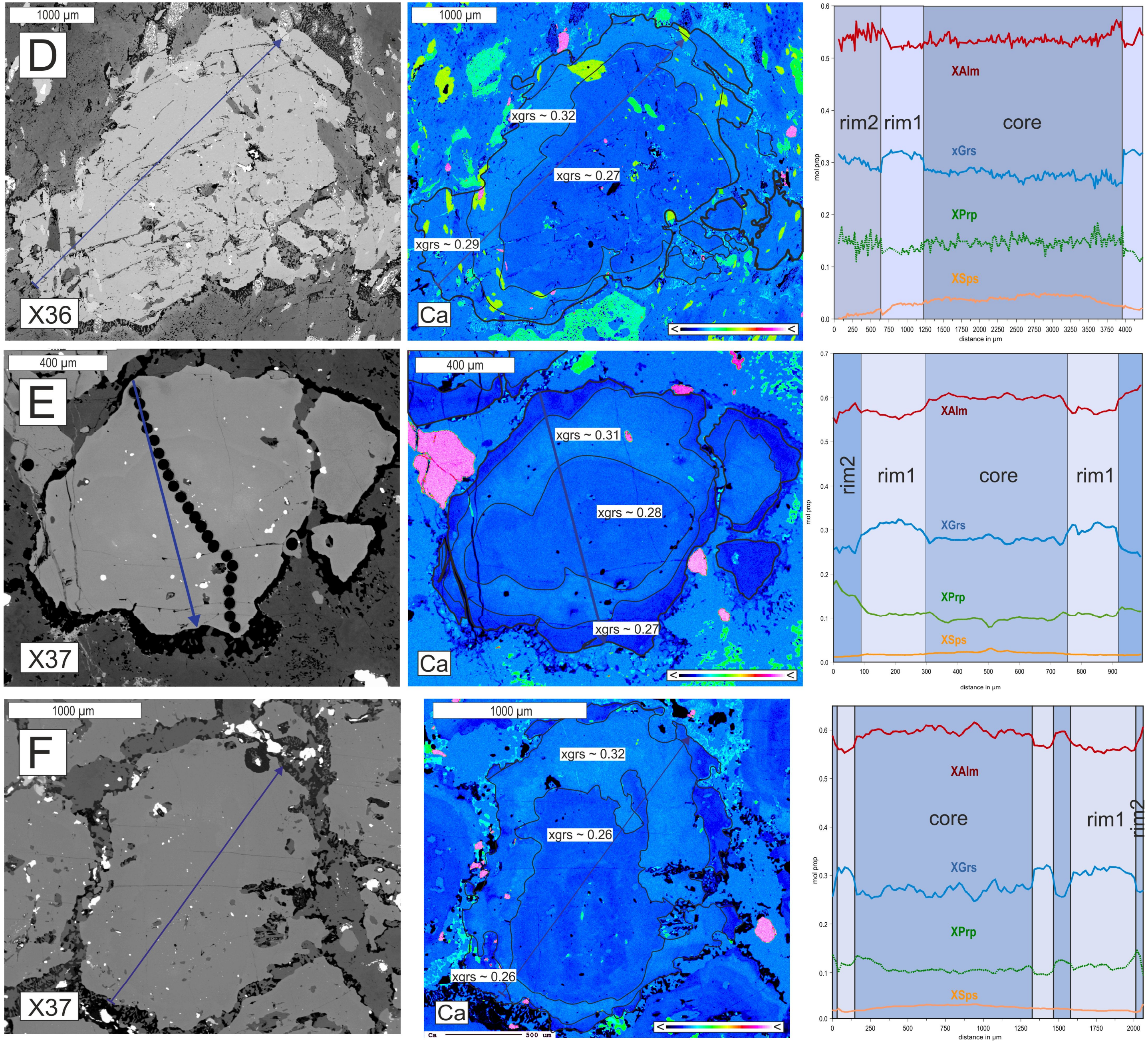

(D) Sample X36. Profile D shows similar characteristics like profile C. Again with X_{Grs} plateaus in rim1 and increasing X_{Prp} in rim2. **(E)** Garnet profile of sample X37. Black dots in BSE image were generated by laser ablation. Profiles of X37 are similar to those of X35 but slightly einriched in X_{Grs} and contain less amounts of X_{Alm}. There is a X_{Grs} plateau marking rim1. X_{Sps} decreases almost gradually towards the rim. X_{Prp} shows constant values in core and rim1 and increases in rim2. X_{Alm} shows a inverse X_{Grs} zoning, with enriched cores and usually also an increase in rim2. **(F)** Garnet zonation profile of sample X37 shows very similar zoning patterns compared with profile E. A X_{Grs} plateau and a X_{Prp} moat indicates rim1. X_{Alm} component shows inverse X_{Grs} zoning patterns. X_{Sps} displays a flat distribution from core to rim.

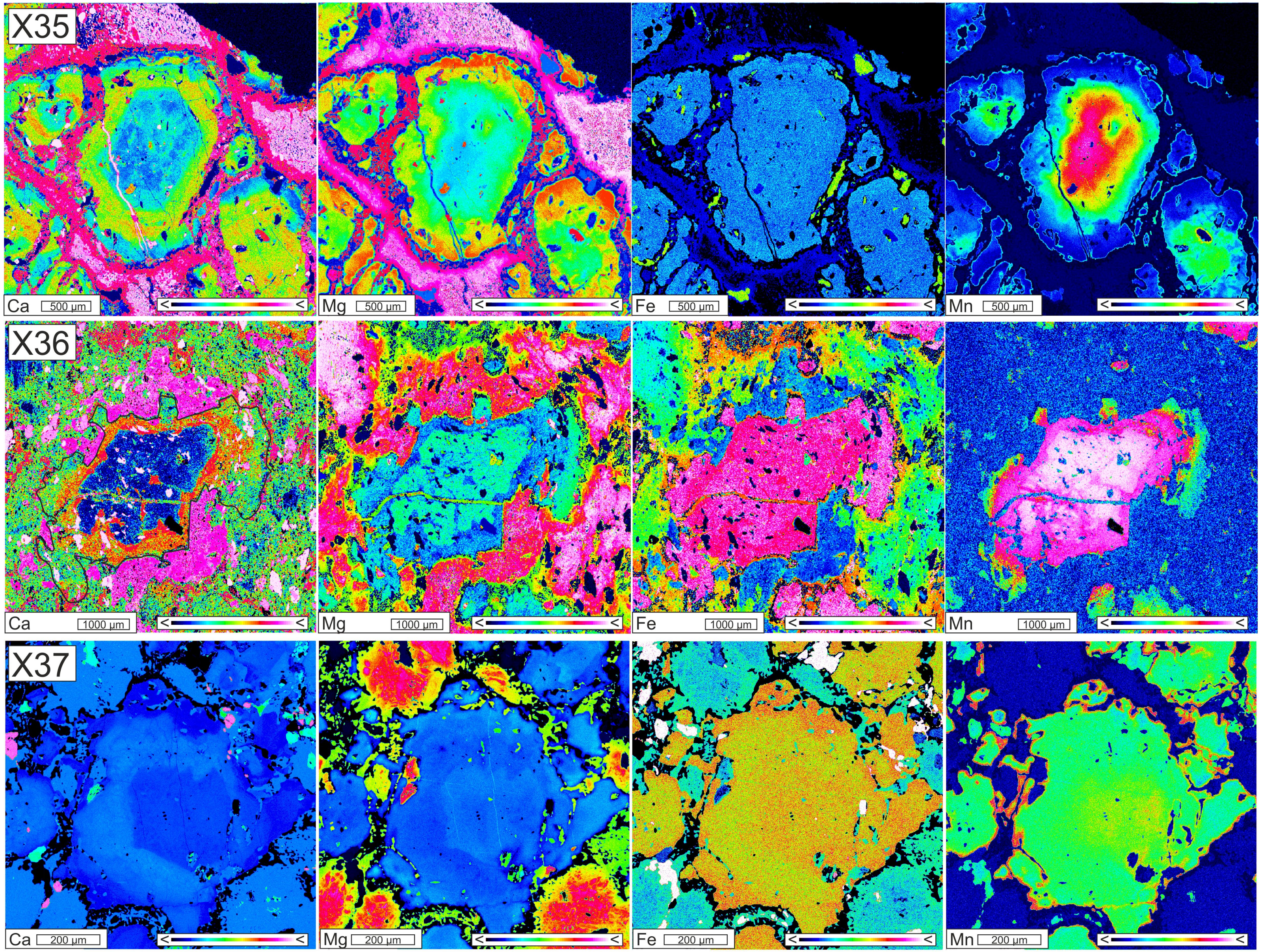

Fig. 19 element distribution images of samples X35, X36 and X37. Garnet grain displayed in Ca-distribution image of X36 is contoured for more convenient discrimination with adjacent matrix mineral phases**.**

8.1 Trace and REE chemistry of garnet

The distribution of trace elements and REEs in metamorphic minerals can reveal important information of the rocks metamorphic history when coupled with the fact that diffusion of trace elements and REEs functions, in general, are considerably slower than diffusion of major elements (Volkova et al., 2014). Concerning REEs, garnets show increasing partition coefficients along with higher atomic number. That usually leads to typical chondrite normalized REE patterns with highly enriched HREEs. Nevertheless, breakdown of surrounding minerals while garnet growth could introduce REEs into the system and consequently contribute to a change of chondrite normalized REE distribution patterns. In metabasic rocks, substantial amounts of REEs are incorporated into Grt, Cpx, Amp, and Czo/Ep. But also accessory minerals such as Ap and Spn partition decent quantities of LREEs and traces and therefore should not be neglected. In basic rocks, amphibole shows remarkably higher partition coefficients for light HREEs such as Sm and Nd compared to garnet. Therefore Amp breakdown could cause an enrichment of those elements in garnet REE distribution patterns which might be the case in the trends observed in garnet grains of the Songshugou garnet amphibolites. Partition coefficient data of elements for all types of rocks and minerals were taken from http://earthref.org. For LA ICPMS analysis, inclusion- and crack-poor garnets were chosen. BSE images with major element zoning patterns and selected trace and REE profiles of garnet grains from sample X35, X36 and X37 are displayed in Fig. 21, Fig. 22 and Fig. 23. In the following, trace and REE geochemistry of a garnet grain of sample X37 (Fig. 23) is described in detail. V, Ni and Cr show remarkable zoning patterns with very low abundances in the core and a sudden increase in rim1. Ilmenite occurs as a prominent mineral included in garnet cores, but is hardly existant, if at all, in rims. This indicates that garnet rims evolved at PT conditions beyond Ilm stability. Ilmenite usually contains significant amounts of Cr, Ni, Sc, and V. Thus the observed increase in V, Ni and Cr in garnet rim1 points to a breakdown of Ilm to Grt and Rt.

LREE (Sc, La, Ce, Pr, Nd, Pm, Sm, Eu, Gd) **:** The elements La to Pr are typically very low or not detectable in garnets. Neodymium, Sm, Eu and Gd show similar zoning trends with low abundances in the core and an abrupt increase at rim 1, which would be symptomatic for the breakdown of Amp, which preferentially incorporates these elements. The absence of a negative Eu anomaly in the chondrite normalized REE pattern of garnet indicates that Pl did not play a role in the distribution of Eu.

HREE (Y, Tb, Dy, Ho, Er, Tm, Yb, Lu): the elements Er, Tm, Yb and Lu show typical Rayleigh fractionation. Yttrium, Tb, Dy and Ho have similar zoning patterns like Nd, Pm, Sm, Eu, Gd. Contents are significantly increasing towards the garnet rims. Again, the breakdown of amphibole would account for the observed distribution pattern. Representative trace element and REE data of garnets from samples X35, X36 and X37 is given in Table 20, Table 21 and Table 22. Garnet of sample X35 and X37 is strongly depleted in LREE with average chondrite-normalized (Nakamura 1974) La_N of <0.05 – 0.06 but enriched in HREE with Yb_N up to 640 in sample X37 and Yb_N up to 352 in sample X35. Garnets of sample X36 show similar fractionation trends but with significantly lower overall REE abundances (Yb_N < 60).

Chondrite normalized REE patterns from the core, rim 1 and rim 2 of samples X35, X36 and X37 are shown in Fig. 24, Fig. 25 and Fig. 26. Garnet core measurements (red lines) show typical HREE enrichments of garnet. Concerning Grt of sample X37, Grt rim measurements (black lines for rim 1, green lines for outermost rim 2) are slightly enriched in the lighter HREEs (Tb, Dy, Ho) with $(Dy/Yb)_N$ = 1.0 – 1.5 for rim1 and $(Dy/Yb)_N$ = 2.0 – 3.6 for rim2, in contrast to garnet core with $(Dy/Yb)_N$ = 0.08 – 0.5. Same trends are observed in samples X35 and X36 with $(Dy/Yb)_N$ =0.20 – 0.60 for grt core, $(Dy/Yb)_N$ = 0.70 - 2.50 for rim1 and $(Dy/Yb)_N$ = 1.90 – 3.60 for rim2 and $(Dy/Yb)_N$ =0.30 – 1.00 for grt core, $(Dy/Yb)_N$ = 0.50 - 4.00 for rim1 and $(Dy/Yb)_N$ = 4.00 – 12.16 for rim2, respectively. The elements Sm, Tb, Dy, Ho and Er are preferably incorporated in Amp and Ep. Breakdown of Amp and/or Ep during garnet rim growth could nourish the system with those elements leading to the observed distribution pattern. Epidote also incorporates Y. Therefore at phase breakdown Y would be available for garnet. Fig. 20 displays a calculated pseudosection of sample X37. Amp modes, plotted as orange lines, decrease towards higher PT conditions. Hence, increasing PT conditions lead to Amp breakdown which could result in the observed chondrite normalized REE patterns of Grt rims with enriched Sm, Eu, Gd, Tb and Dy.

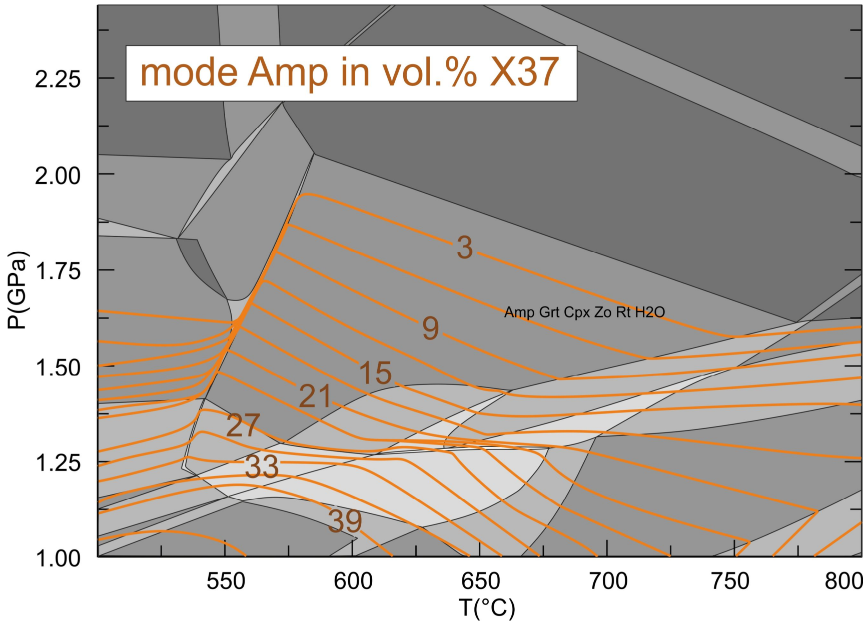

Fig. 20 Pseudosection calculated for sample X37. Orange lines represent Amp mode in vol.%.

In all rock samples, garnets show a general rimward decrease in heavy HREE, with Lu_N up to 360 in garnet core to 6 in the outmost rim for X35, with Lu_N up to 60 in garnet core to 4 in the outmost rim for X36 and Lu_N up to 760 in garnet core to 30 in the outmost rim for X37, which can be explained by HREE depletion of the matrix during garnet growth in a closed system.

Concerning REE and trace element distribution, garnet grains of sample X35 and X36 show similar zoning patterns like sample X37. LREEs such as: Nd, Sm, Eu, Gd and Tb are enriched in garnet rim compared to core. Ho, Er, Tm, Yb and Lu show typical Rayleigh distribution. In contrast to sample X36 and X37, grains of X35 do not show a clear zoning pattern in V and Cr but the garnet cores are enriched in Li.

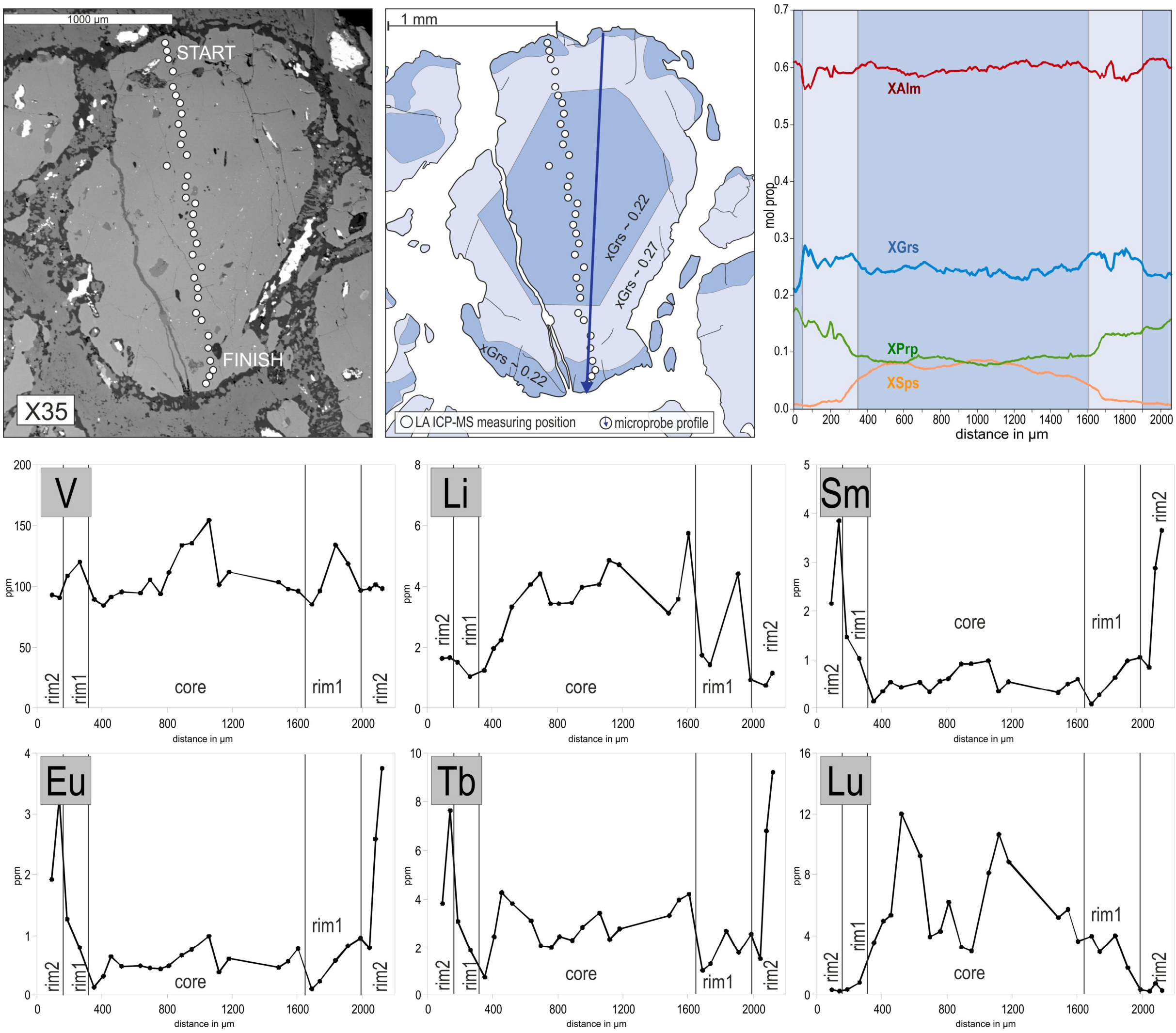

Fig. 21 Top left: BSE image of garnet grain (sample X35). **Top centre**: redrawn garnet grain, zones: core, rim1, and rim2 are contoured after Ca-element distribution image to clearly correlate LA ICP-MS measurements with corresponding garnet zones. Top right: major element zoning pattern, with ubiquitous X_{Grs} plateau marking rim1. **Bottom**: Trace element and REE zoning patterns.

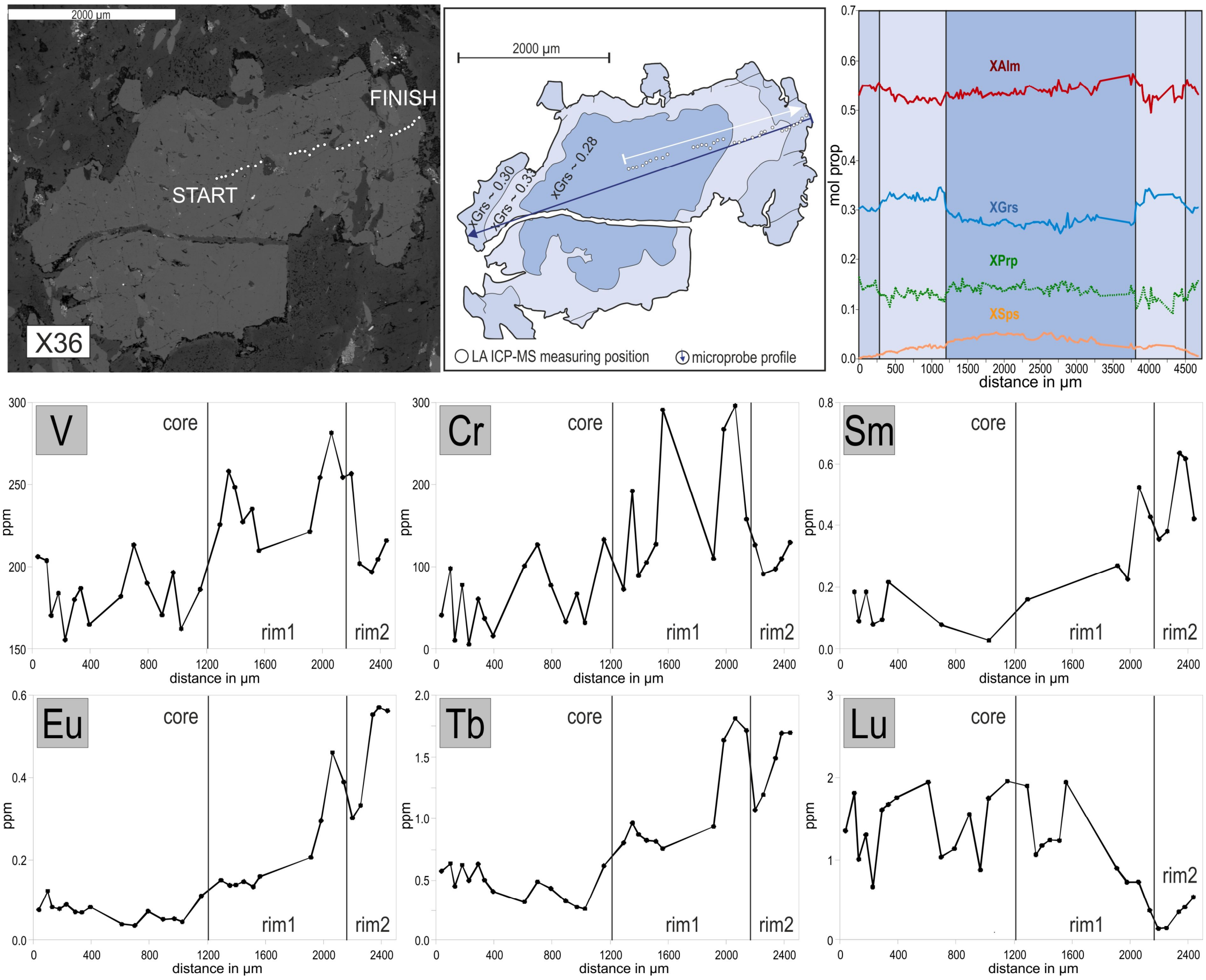

Fig. 22 Top left: BSE image of garnet grain (sample X36). **Top centre**: redrawn garnet grain, zones: core, rim1, and rim2 are contoured after Ca-element distribution image to clearly correlate LA ICP-MS measurements with corresponding garnet zones. Top right: major element zoning pattern, with ubiquitous X_{Grs} plateau marking rim1. **Bottom**: Trace element and REE zoning patterns.

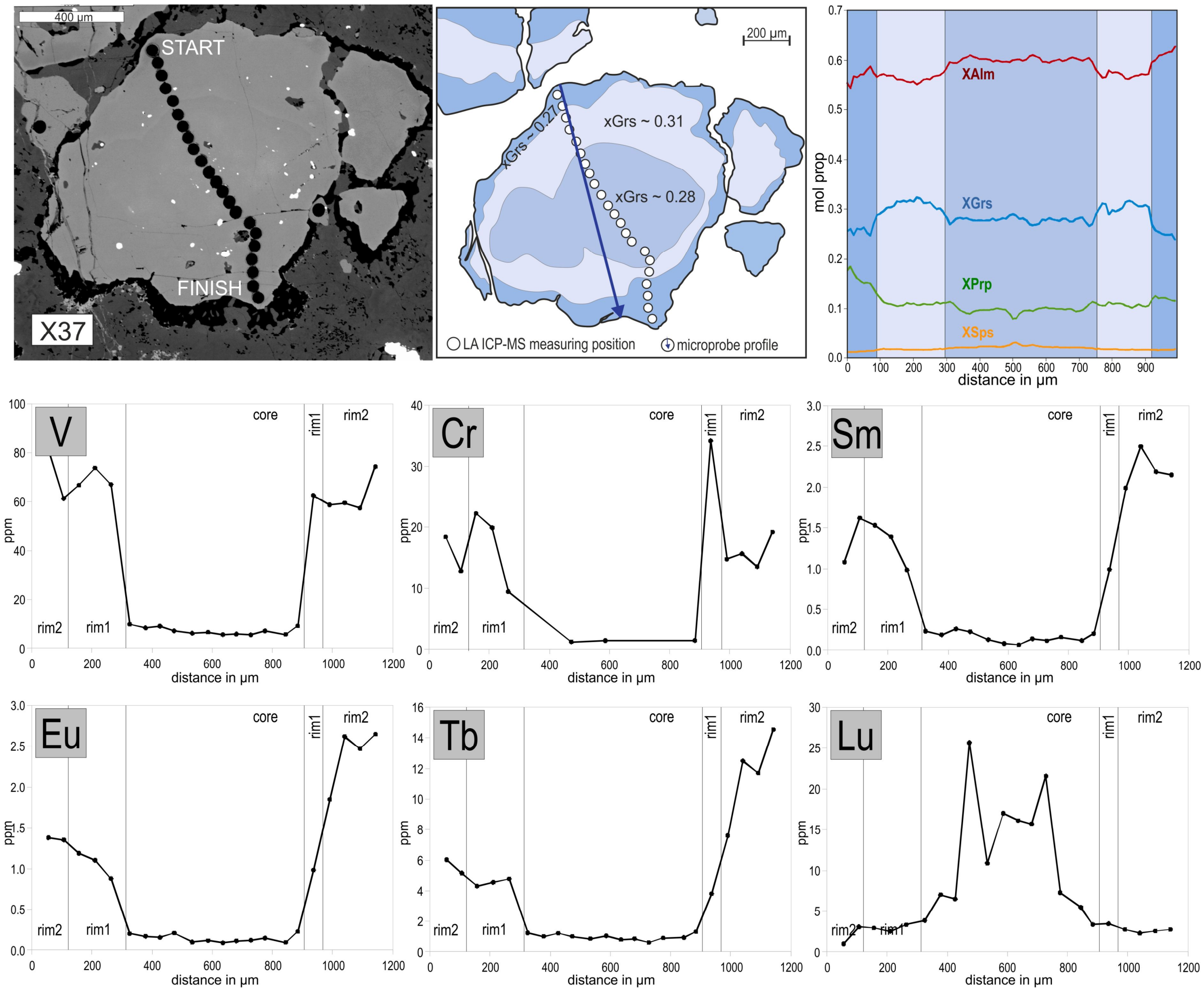

Fig. 23 Top left: BSE image of garnet grain (sample X37). **Top centre:** redrawn garnet grain, zones: core, rim1, and rim2 are contoured after Ca-element distribution image to clearly correlate LA ICP-MS measurements with corresponding garnet zones. **Top right:** major element zoning pattern, with ubiquitous X_{Grs} plateau marking rim1. **Bottom:** Trace element and REE zoning patterns.

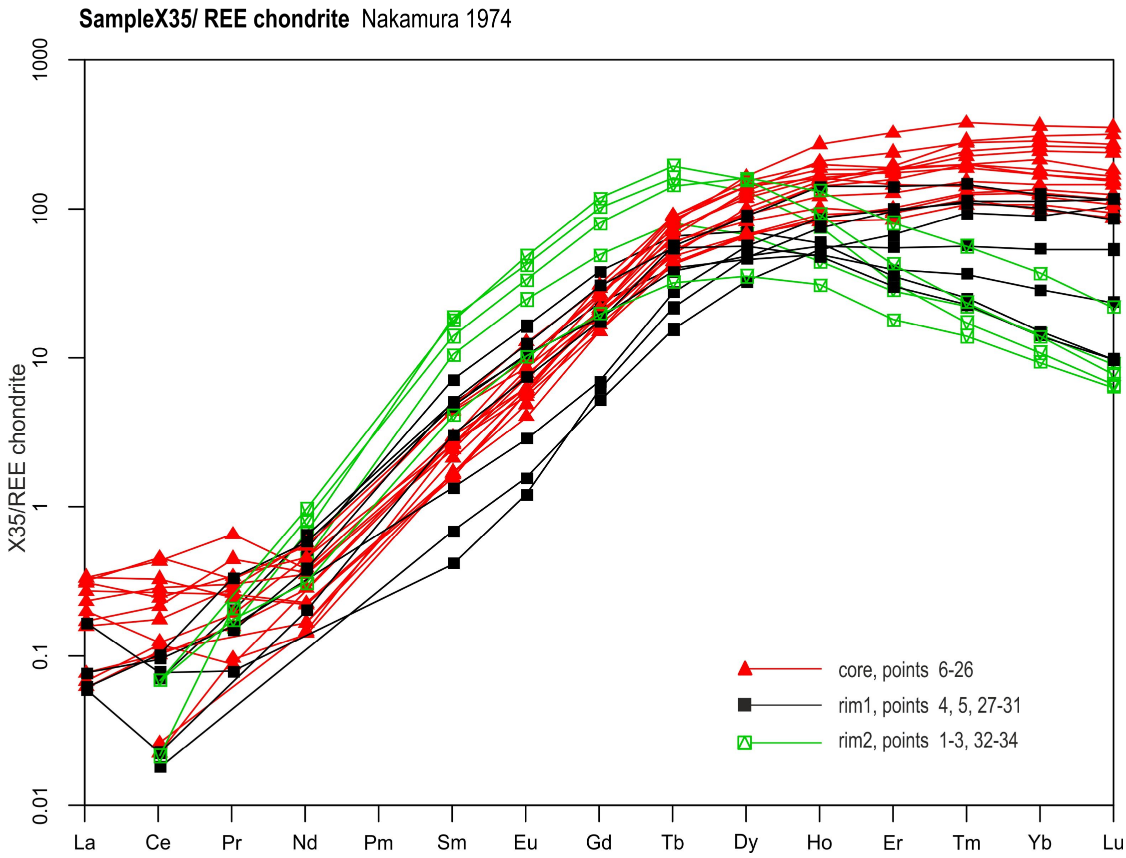

Fig. 24 chondrite normalized REE plot of garnet after Nakamura 1974 (sample X35). Garnet-core, rim1 and rim2 are plotted as red, black and green lines.

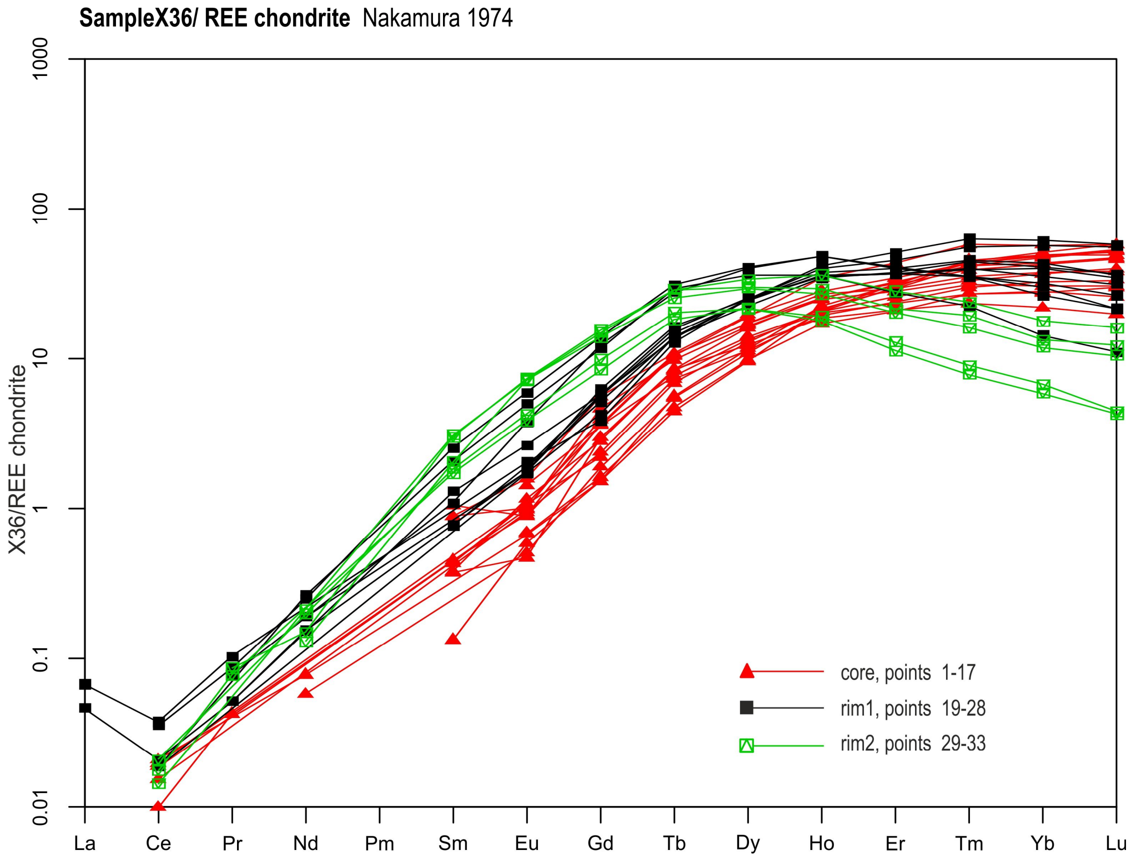

Fig. 25 chondrite normalized REE plot of garnet after Nakamura 1974 (sample X36). Garnet-core, rim1 and rim2 are plotted as red, black and green lines.

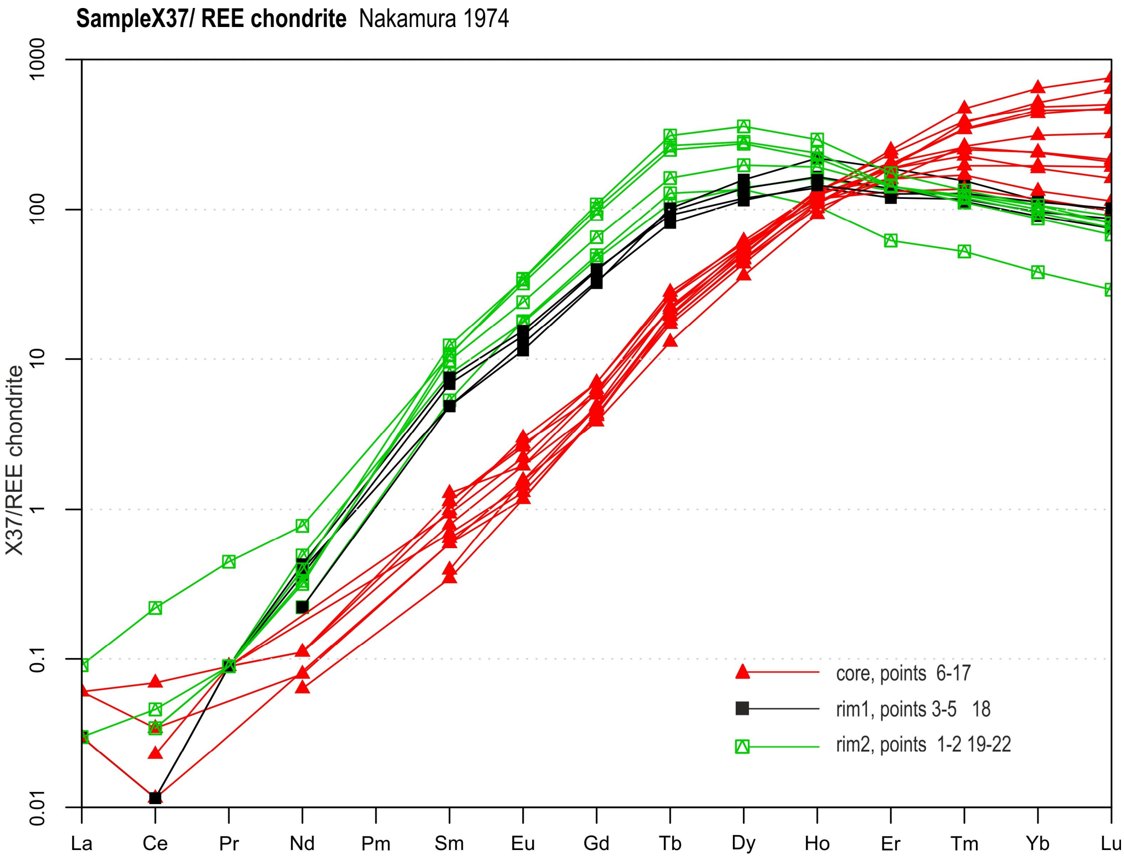

Fig. 26 chondrite normalized REE plot of garnet after Nakamura 1974 (sample X37). Garnet-core, rim1 and rim2 are plotted as red, black and green lines.

Table 20 representative garnet analyses of trace elements and REEs obtained by LA-ICP-MS. Sample X35

representative analysis of trace elements and REEs, sample X35						
	core		**rim1**		**rim2**	
Point	*8*	*25*	*3*	*4*	*1*	*2*
^{7}Li	3.32	3.59	1.52	1.05	1.64	1.67
^{31}P	41.5	31.3	43.8	51.7	54.4	45.3
^{49}Ti	713	795	285	337	430	310
^{51}V	95.6	97.9	109	120	93.2	91.0
^{53}Cr	<0.05	<0.05	2.93	11.1	7.76	1.94
^{59}Co	21.7	22.6	33.2	31.4	47.4	43.6
^{60}Ni	1.00	0.91	1.40	2.01	0.75	1.00
^{66}Zn	99.2	97.5	96.9	94.9	83.9	101.7
^{71}Ga	13.3	13.9	18.2	18.3	11.5	17.4
^{88}Sr	0.07	0.10	0.06	0.20	<0.05	<0.05
^{89}Y	549	382	97.1	89.8	80.4	140
^{90}Zr	33.8	11.5	1.01	1.79	2.47	1.25
^{139}La	<0.05	0.08	<0.05	<0.05	<0.05	<0.05
^{140}Ce	<0.05	0.25	<0.05	0.06	<0.05	<0.05
^{141}Pr	<0.05	<0.05	<0.05	<0.05	<0.05	<0.05
^{146}Nd	0.11	0.23	0.33	0.41	0.29	0.43
^{147}Sm	0.43	0.50	1.46	1.02	2.15	3.84
^{153}Eu	0.48	0.57	1.27	0.80	1.92	3.27
^{157}Gd	5.97	7.13	10.6	6.53	13.6	28.5
^{159}Tb	3.82	3.97	3.08	1.90	3.82	7.6
^{163}Dy	57.0	48.8	24.5	16.0	23.6	45.8
^{165}Ho	19.04	13.08	4.22	3.45	3.12	5.34
^{166}Er	72.2	41.3	8.08	8.86	6.45	7.33
^{169}Tm	11.2	5.97	0.76	1.11	0.68	0.52
^{172}Yb	79.4	40.1	3.35	6.33	3.21	2.42
^{175}Lu	11.98	5.72	0.34	0.81	0.32	0.23
^{178}Hf	0.74	0.35	0.11	0.07	0.09	0.21
^{181}Ta	0.12	0.09	<0.05	<0.05	<0.05	<0.05

data in ppm, beam size diameter 35 µm, 0.6 C He, 11 Hertz, irradiance 1.71 gW/cm², Fluence 9 J/cm²

Table 21 representative garnet analyses of trace elements and REEs obtained by LA-ICP-MS. Sample X36

representative analysis of trace elements and REEs, sample X36						
	core		**rim1**		**rim2**	
Point	*17*	*8*	*20*	*23*	*31*	*32*
^{7}Li	1.13	1.69	1.54	1.43	0.83	0.91
^{31}P	39.2	36.2	36.5	38.9	32.0	42.3
^{49}Ti	748	1015	673	530	424	485
^{51}V	186	165	258	235	197	204
^{53}Cr	133	15.8	192	127	97	109
^{59}Co	43.0	35.0	36.5	39.9	41.8	45.3
^{60}Ni	1.35	1.24	2.15	2.02	1.58	1.25
^{66}Zn	65.9	43.8	58.0	62.3	67.7	72.1
^{71}Ga	12.4	12.8	13.7	13.7	12.8	14.1
^{88}Sr	0.06	0.14	<0.05	0.07	<0.05	<0.05
^{89}Y	62.2	44.0	70.6	76.3	49.3	51.6
^{90}Zr	4.93	4.81	3.55	3.47	2.44	2.25
^{139}La	<0.05	<0.05	<0.05	<0.05	<0.05	<0.05
^{140}Ce	<0.05	<0.05	<0.05	<0.05	<0.05	<0.05
^{141}Pr	<0.05	<0.05	<0.05	<0.05	<0.05	<0.05
^{146}Nd	<0.05	<0.05	0.12	<0.05	0.14	0.10
^{147}Sm	<0.05	<0.05	<0.05	<0.05	0.63	0.62
^{153}Eu	0.11	0.08	0.14	0.13	0.55	0.57
^{157}Gd	1.00	0.62	1.74	1.18	3.84	4.28
^{159}Tb	0.49	0.33	0.77	0.65	1.19	1.35
^{163}Dy	6.47	4.43	8.60	8.59	10.10	10.29
^{165}Ho	2.42	1.52	2.46	2.60	1.87	2.04
^{166}Er	9.74	6.58	8.31	9.05	4.51	4.88
^{169}Tm	1.71	1.26	1.19	1.36	0.48	0.58
^{172}Yb	12.5	10.3	7.82	9.48	2.63	2.94
^{175}Lu	1.96	1.76	1.06	1.23	0.36	0.42
^{178}Hf	0.06	<0.05	0.18	0.08	0.09	0.06
^{181}Ta	<0.05	<0.05	<0.05	<0.05	<0.05	<0.05

data in ppm, beam size diameter 35 µm, 0.6 C He, 11 Hertz, irradiance 1.71 gW/cm², Fluence 9 J/cm²

Table 22 representative garnet analyses of trace elements and REEs obtained by LA-ICP-MS. Sample X37

representative analysis of trace elements and REEs, sample X37						
	core		rim1		rim2	
Point	*11*	*12*	*4*	*5*	*2*	*20*
^{7}Li	2.17	0.77	1.10	1.81	1.05	2.95
^{31}P	18.5	17.2	25.5	23.5	21.4	21.9
^{49}Ti	392	297	363	887	298	245
^{51}V	6.6	5.6	73.7	67.0	61.3	59.4
^{53}Cr	1.45	<0.05	19.9	9.45	12.8	15.7
^{59}Co	13.3	12.7	20	21.1	23.8	28.3
^{60}Ni	1.09	1.00	1.82	1.75	1.31	1.42
^{66}Zn	138	134	106	105	89.8	85.1
^{71}Ga	12.6	11.1	10.1	14.0	12.7	14.9
^{88}Sr	0.06	0.08	<0.05	<0.05	<0.05	0.23
^{89}Y	281	232	291	374	284	404
^{90}Zr	28.6	98.5	3.35	3.96	1.17	10.9
^{139}La	<0.05	<0.05	<0.05	<0.05	<0.05	<0.05
^{140}Ce	<0.05	<0.05	<0.05	<0.05	<0.05	<0.05
^{141}Pr	<0.05	<0.05	<0.05	<0.05	<0.05	<0.05
^{146}Nd	<0.05	<0.05	0.23	0.14	0.31	0.25
^{147}Sm	0.08	0.07	1.39	0.99	1.62	2.50
^{153}Eu	0.12	0.09	1.10	0.88	1.35	2.62
^{157}Gd	1.35	1.19	10.8	8.91	12.9	28
^{159}Tb	1.05	0.8	4.56	4.78	5.15	12.5
^{163}Dy	18.9	14.9	47.4	54.1	47.9	96.5
^{165}Ho	9.24	7.59	11.6	15.3	11.4	16.6
^{166}Er	52.7	44.5	31.0	42.1	30.1	32.5
^{169}Tm	11.6	10.2	3.39	4.66	3.76	3.34
^{172}Yb	106	95.7	19.9	25.3	23.4	19.1
^{175}Lu	17.02	16.13	2.54	3.34	3.08	2.31
^{178}Hf	0.67	2.25	0.28	0.33	0.29	0.74
^{181}Ta	0.07	0.05	0.06	0.09	0.07	0.09

data in ppm, beam size diameter 35 µm, 0.6 C He, 11 Hertz, irradiance 1.71 gW/cm², Fluence 9 J/cm²

8.2 Mineral Chemistry of garnet inclusions

Garnet grains have grain sizes up to 5 mm, and are typically inclusion rich. Metamorphic rocks such as the metabasic unit of the Songshugou ophiolite were exposed to recrystallization processes under changing PT conditions. Therefore mineral assemblages related to an early metamorphic overprint may only be preserved in Grt as mineral inclusions (Chopin, 1984; Zhang et al., 1997; Perchuk et al., 1998). The abundance and distribution of garnet inclusions is not uniform in all Grt amphibolite rock samples of the Songshugou ophiolite. The most common inclusions include Amp, albitic Pl, Qz, Czo/Ep, Ilm, Ap, Zrn and in some samples, Spn. Other mineral phases like Cpx, Bt, Rt, and sulfides are rarely found. Few grains show snowball-like inclusion alignments in their cores, which is indicative of syntectonic growth of the garnet core (Fig. 4g). Sketch maps of garnets redrawn after BSE images of samples X35, X36 and X37 are located in Fig. 27, Fig. 28 and Fig. 29. Different shades of blue represent garnet zones, contoured according to their Ca content. As mentioned earlier, most garnets comprise 3 different zones: 1) core, 2) X_{Grs} rich rim1 and 3) slightly less X_{Grs} rich rim2. In some cases rim 2 is entirely consumed due to retrogression (Fig. 27, left garnet). Cracks are usually filled by Amp. Some minerals like Ilm, Pl, Qz, ± Prh are restricted to garnet cores whereas Ap, Zrn, Amp ±Cz/Ep occure in all zones.

Amphibole, both in core and rim1, is of pargasitic composition. There is significant chemical variation among samples with respect to weight percent Al_2O_3 (15 – 20), MgO (5 – 10), FeO (15 – 22), Na_2O (2 – 3.5). Amphibole inclusions in rim1 and rim2 as well as Amp inclusions in the core are not distinctively different in composition. Only a slight elevation in MgO and CaO conjoined with lower FeO is sometimes observed in rim1. However, Amp grains enclosed in Grt cores adjacent to Czo/Ep contain less Al_2O_3. Representative mineral analyses are displayed in table 23. Plagioclase inclusions are restricted to Grt cores and almost purely of albitic composition (X_{Ab} ~ 0.99). In seldom cases polyphase inclusions of albitic Pl and Kfs are found. Representative microprobe data of Pl is presented in table 23. Sphene occurance is observed in sample X36 as inclusions in rim and core. Sphene shows a positive compositional correlation between F and Al + Fe^{3+} and a negative linear correlation between Ti and Al + Fe^{3+}, indicating the coupled substitution: Ti^{4+}+O^{2-} = (Al, Fe^{3+})+ (F, OH)- (Enami et al., 1993). Thin rods of Rt sometimes occur within Grt rims. Representative microprobe data of Spn is presented in table 24. Apatite found as inclusions in Grt rim and core is Fluorapatite with F/Cl > 1. FeO contents are below 1 wt.%. Core Ap shows higher F contents (2 – 2.5 wt.%) than Ap included in the rim (F = 1.2 – 1.5 wt.%). Ca/P is slightly higher for Ap included in Grt rim with ~ 1.7 compared to ~ 1.6 for those found in core. Small Ca/P ratios trigger the augmentations of vacancies in the apatitic structure. Microprobe analyses are presented in table 25. Clinozoisite/epidote occurs commonly in Grt cores and sometimes rim1 and rim2. Grains display a strong zoning in Al_2O_3 and Fe_2O_3 varying from 21 to 27 wt.% and 9 to 12 wt.%, respectively. REEs were not quantitatively analyzed but were observed in EDX spectrum when total sum was low. Clinozoisite/epidote microprobe analyses are given in table 24. Zircon occurs in all Grt zones, with grain sizes usually smaller than 20 µm. Sample X37 exhibits an exceedingly amount of Zrn inclusions compared to other samples. Rutil rarely appears as thin rods in Grt rim. Quartz occurs as small rounded or rod shaped grains in Grt core or in aggregates together with Amp and Pl.

Chemical zoning patterns in garnets (REEs and majors) and different mineral assemblages associated with core and rim compositions indicate a poly-phase metamorphic history.

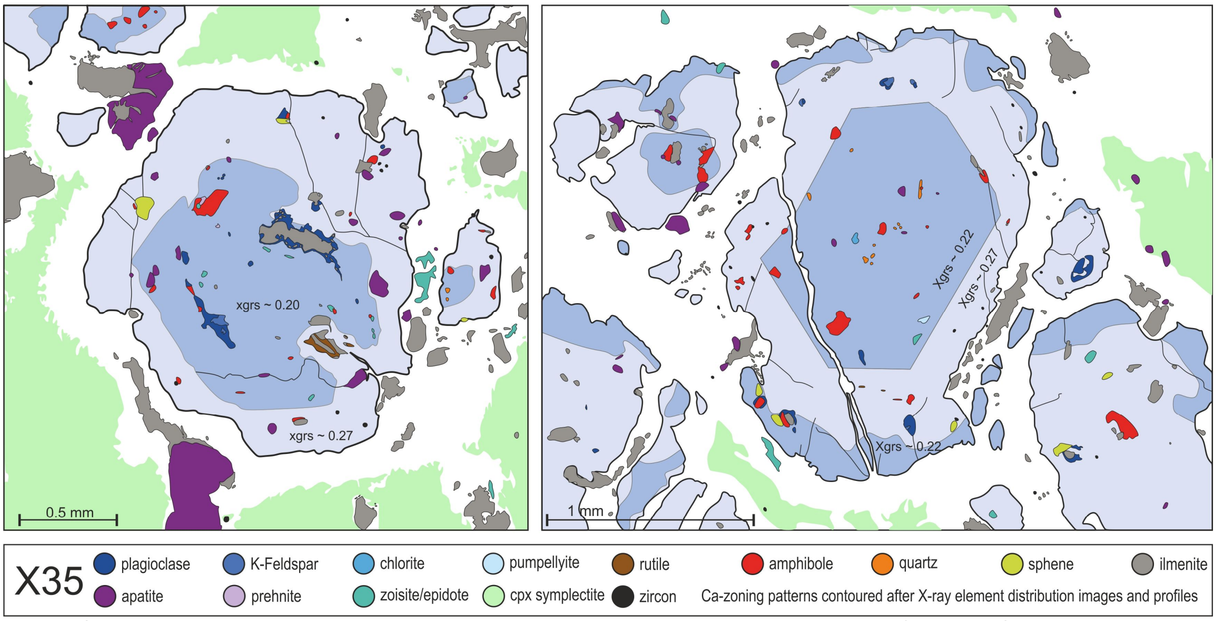

Fig. 27 Sample X35. Redrawn garnet grains. Blue areas represent garnet zones contoured after X-ray Ca-distribution images.

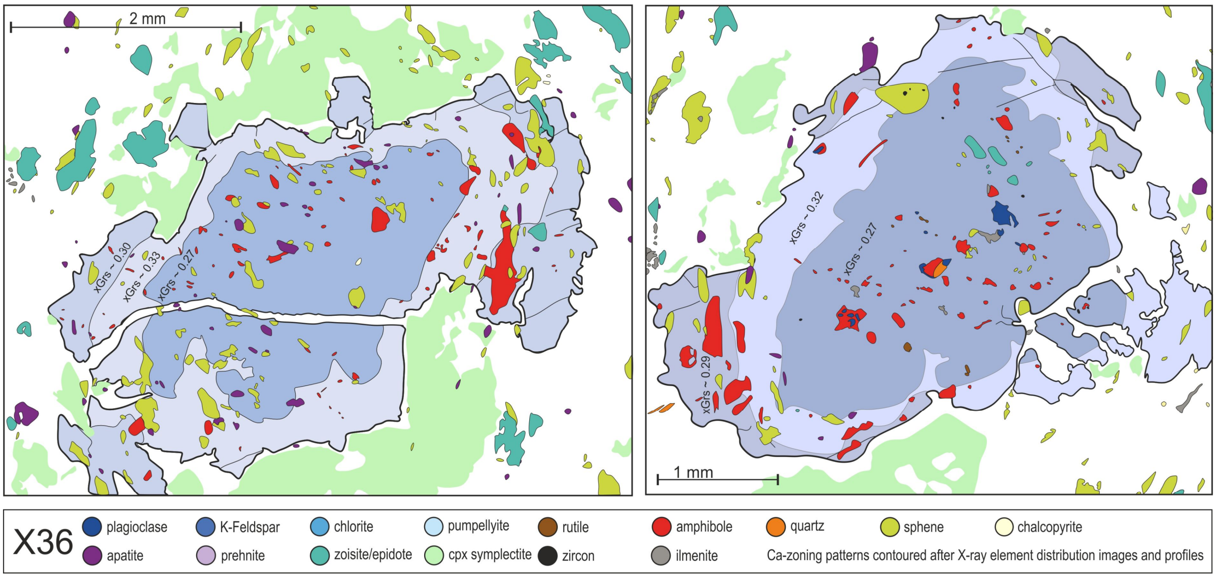

Fig. 28 Sample X36. Redrawn garnet grains. Blue areas represent garnet zones contoured after X-ray Ca-distribution images.

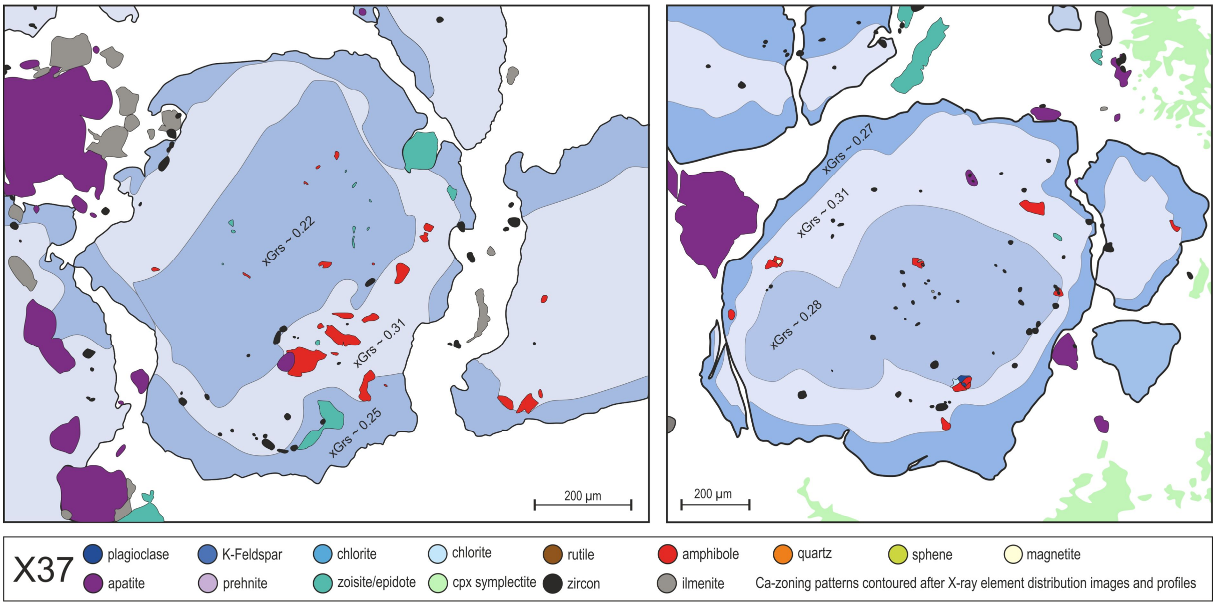

Fig. 29 Sample X37. Redrawn garnet grains. Blue areas represent garnet zones contoured after X-ray Ca-distribution images.

table 23 representative microprobe analysis of amphibole included in garnet

representative analysis of amphibole included in garnet (O = 23)									
	core			adjacent to epidote			rim1		
	x353d8	4_54	x36a_31	x33d12	x33d13	x33d14	4_55	37g1_3	x353d_26
IMA	pargasite			pargasite			pargasite		
SiO_2	38.68	37.90	38.29	41.55	40.46	39.12	39.20	39.66	38.70
TiO_2	0.26	0.17	0.38	0.76	0.29	0.36	1.50	0.32	0.86
Al_2O_3	18.63	20.63	19.15	14.63	15.94	17.36	18.94	18.70	18.41
Cr_2O_3	<0.10	<0.10	<0.10	<0.10	<0.10	<0.10	<0.10	<0.10	<0.10
FeO	18.71	19.68	17.23	16.73	18.50	18.48	16.27	16.57	16.97
MnO	0.15	0.16	0.13	0.11	0.13	<0.10	<0.10	<0.10	<0.10
MgO	7.32	5.87	8.78	9.60	8.75	7.69	8.26	8.66	8.52
CaO	10.88	10.85	11.76	11.01	10.96	10.85	11.74	11.10	11.44
Na_2O	3.08	2.29	2.56	2.96	3.05	3.10	2.24	2.88	2.64
K_2O	<0.10	<0.10	<0.10	<0.10	<0.10	<0.10	<0.10	<0.10	<0.10
F	<0.10	0.17	<0.10	0.25	0.38	0.27	0.20	<0.10	0.17
Cl	<0.10	<0.10	<0.10	0.11	<0.10	<0.10	<0.10	0.18	<0.10
Total	**97.70**	**97.72**	**98.29**	**97.70**	**98.46**	**97.23**	**98.36**	**98.07**	**97.72**
Si	5.785	5.688	5.629	6.174	5.999	5.887	5.763	5.849	5.742
Ti	0.030	0.019	0.042	0.084	0.032	0.040	0.166	0.035	0.096
Al	3.283	3.648	3.317	2.562	2.786	3.079	3.282	3.251	3.219
Fe^{3+}	0.536	0.461	0.810	0.486	0.675	0.548	0.476	0.480	0.616
Cr	0.000	0.000	0.000	0.000	0.000	0.000	0.000	0.000	0.000
Fe^{2+}	1.804	2.009	1.308	1.593	1.619	1.778	1.524	1.563	1.489
Mn	0.019	0.021	0.016	0.014	0.017	0.000	0.000	0.000	0.000
Mg	1.632	1.313	1.925	2.126	1.934	1.725	1.811	1.904	1.885
Ca	1.743	1.745	1.852	1.752	1.740	1.750	1.849	1.754	1.819
Na	0.892	0.667	0.728	0.852	0.877	0.905	0.640	0.824	0.758
K	0.000	0.000	0.000	0.000	0.000	0.000	0.000	0.000	0.000
F	0.000	0.082	0.000	0.118	0.177	0.126	0.095	0.000	0.081
Cl	0.000	0.000	0.000	0.028	0.000	0.000	0.000	0.045	0.000
SumCat	**15.724**	**15.653**	**15.627**	**15.789**	**15.856**	**15.838**	**15.606**	**15.705**	**15.705**
X_{Mg}	0.475	0.395	0.595	0.572	0.544	0.492	0.543	0.549	0.559
Al(IV)	2.215	2.312	2.371	1.826	2.001	2.113	2.237	2.151	2.258
Al(VI)	1.067	1.336	0.946	0.736	0.784	0.966	1.045	1.100	0.961

table 24 representative microprobe analysis of sphene and clinozoisite/epidote included in garnet

representative sphene (O = 5) and Czo/Ep (O = 12.5) analysis included in garnet									
		core		rim1		rim2		core	
sample	b_20	4_58	7_15	f_9	4_59	4_60	7_8	7_9	Gt3-24
Mineral		sphene			sphene			clinozoisite/epidote	
SiO_2	30.21	30.37	30.56	30.54	30.75	30.16	38.18	37.87	34.55
TiO_2	37.43	37.96	37.37	37.95	38.08	38.14	0.12	0.28	0.18
Fe_2O_3	0.83	0.88	1.00	0.70	0.69	1.10	9.40	10.23	11.90
Al_2O_3	1.40	1.59	1.48	1.30	1.59	1.83	26.75	25.89	21.85
Cr_2O_3	<0.10	<0.10	<0.10	<0.10	<0.10	<0.10	<0.10	<0.10	<0.10
MnO	<0.10	<0.10	<0.10	<0.10	<0.10	<0.10	0.14	0.14	<0.10
MgO	0.00	0.00	0.10	0.11	0.00	0.00	0.12	0.00	0.25
CaO	27.61	27.43	27.29	27.48	27.88	27.42	22.18	21.97	18.34
F	0.41	0.44	0.47	0.29	0.42	0.22	0.13	0.21	0.00
Total	**97.97**	**98.91**	**98.32**	**98.45**	**99.73**	**99.21**	**97.05**	**96.64**	**87.06**
Si	1.009	1.005	1.016	1.012	1.010	0.995	3.011	3.013	3.053
Ti	0.940	0.945	0.934	0.946	0.941	0.946	0.007	0.017	0.012
Al	0.021	0.022	0.025	0.017	0.017	0.027	0.558	0.612	0.791
Fe^{3+}	0.055	0.062	0.058	0.051	0.062	0.071	2.486	2.427	2.276
Cr	0.000	0.000	0.000	0.000	0.000	0.000	0.000	0.000	0.000
Mn	0.000	0.000	0.000	0.000	0.000	0.000	0.009	0.009	0.000
Mg	0.000	0.000	0.005	0.005	0.000	0.000	0.014	0.000	0.033
Ca	0.988	0.973	0.972	0.976	0.981	0.969	1.874	1.873	1.736
F	0.043	0.046	0.049	0.030	0.044	0.023	0.032	0.053	0.000
SumCat	**3.057**	**3.048**	**3.061**	**3.039**	**3.041**	**3.027**	**7.992**	**8.006**	**7.892**
Al+Fe3	0.076	0.084	0.083	0.068	0.079	0.098			

table 25 representative microprobe analysis of apatite and ilmenite included in garnet

representative apatite analysis (O = 25) included in garnet						
	core		rim		core	
sample	4_46	4_47	Gt3-46	Gt3-47	x353c7	x353c8
Mineral	apatite		apatite		ilmenite	ilmenite
P_2O_5	42.94	42.45	41.61	41.40	-	0.25
TiO_2	-	-	-	-	50.99	51.10
V_2O_3	-	-	-	-	0.50	0.61
Al_2O_3	0.22	0.00	0.29	0.18	-	-
FeO	0.30	0.38	0.35	0.53	47.85	47.40
MnO	-	-	-	-	0.61	0.74
MgO	-	-	-	-	-	-
CaO	53.86	53.80	55.73	56.01	<0.10	0.30
F	2.18	2.47	1.44	1.26	-	-
Cl	0.14	<0.10	<0.10	<0.10	0.16	0.25
Total	**99.64**	**99.10**	**99.42**	**99.38**	**100.11**	**100.65**
P	6.090	6.079	5.927	5.905	0.000	0.005
Ti	0.000	0.000	0.000	0.000	0.964	0.959
Fe^{3+}	0.000	0.000	0.000	0.000	0.075	0.075
V	0.000	0.000	0.000	0.000	0.010	0.012
Al	0.043	0.000	0.058	0.036	0.000	0.000
Fe^{2+}	0.042	0.054	0.049	0.075	0.931	0.914
Mn	0.000	0.000	0.000	0.000	0.013	0.016
Mg	0.000	0.000	0.000	0.000	0.000	0.000
Ca	9.668	9.750	10.047	10.110	0.000	0.008
F	1.155	1.321	0.766	0.671	0.000	0.000
Cl	0.040	0.000	0.000	0.000	0.007	0.011
SumCat	**17.038**	**17.204**	**16.847**	**16.797**	**2.000**	**2.000**
Ca/P	1.588	1.604	1.695	1.712		

table 26 representative microprobe analysis of plagioclase included in garnet cores.

representative plagioclase analysis (O = 8) included in garnet core				
	Gt3-6	Gt3-19	Gt3-20	Gt3-21
Mineral	plagioclase			
SiO_2	67.22	63.52	66.50	66.55
Al_2O_3	20.50	17.80	19.98	19.68
Fe_2O_3	0.90	0.41	0.40	0.81
CaO	0.44	0.00	0.82	0.80
Na_2O	11.35	0.12	11.13	11.23
K_2O	0.03	16.76	0.01	0.04
Total	**100.48**	**98.62**	**98.88**	**99.16**
Si	2.935	2.993	2.947	2.948
Al	1.055	0.989	1.044	1.027
Fe^{3+}	0.029	0.015	0.013	0.027
Ca	0.021	0.000	0.039	0.038
Na	0.961	0.011	0.956	0.964
K	0.002	1.007	0.001	0.002
SumCat	**5.0**	**5.0**	**5.0**	**5.0**
X_{Ab}	0.98	0.01	0.96	0.96
X_{An}	0.02	0.00	0.04	0.04
X_{Or}	0.00	0.99	0.00	0.00

9 Geochemistry

9.1 Major and trace element geochemistry

Metamafic rocks from the Songshugou ophiolite exhibit a wide range of whole rock compositions. All analyzed samples are of basic to ultrabasic composition. Metabasic rocks were subdivided according to their whole rock chemistry and mineralogy into Grt amphibolites and amphibolites. Amphibolites, which were subdivided into schistose amphibolites and augenamphibolites by previous authors, are herein combined, by reason of their geochemic similarity. Amphibolites contain SiO_2 ranging from 45 wt.% to 49 wt.%, whereas Grt-amphibolites contain less SiO_2 varying from 38 wt.% to 42 wt.%. Loss on ignition (LOI) is fairly low with values less than 0.7 wt.% in all samples. Whole rock data from previous studies by Zhang et al. (1999), Dong et al. (2008) and Li Tang et al. (2016) is plotted along with the data from this study, for comparative reasons (Fig. 40).

Amphibolites show a wide variation in Fe_2O_3t (12 - 17 wt.%) and have low P_2O_5 with ~ 0.15 wt.%. CaO varies from 8.5 wt.% to 13.5 wt.% and TiO_2 ranges from 1.4 wt.% to 1.8 wt.%. Grt-amphibolites contain elevated TiO_2 (2.3 - 3.3 wt.%), P_2O_5 (0.3 – 0.8 wt.%) and Fe_2O_3t (18 - 25 wt.%) values. Concerning amphibolites, CaO plotted against MgO shows a positive correlation whereas Na_2O, SiO_2, TiO_2, P_2O_5 correlates negatively, which is typical for tholeiitic differentiation (Fig. 30). Trace elements like Ni and Cr decrease with increasing MgO, which is symptomatic for Ol and Cpx or spinel fractionation. LILE and HFSE are incompatible in most minerals and therefore accumulate in the residual liquid. That trend is well established with increasing Zr, Ba, Ce and Th conjoint with decreasing MgO. Sc shows a positve correlation with MgO which could be an indication of pyroxene fractionation (Fig. 31).

Garnet amphibolites show different trends with MgO correlating positively with Na_2O and K_2O whereas TiO_2, FeOt and P_2O_5 show a negative trend (Fig. 32). A negative correlation between Zr, Ce, Th, Y, Yb vs. MgO is observed. Ni, Cr, V, Rb, Sr, Sc and Ba show a positive correlation (Fig. 33). The fractionation of Amp could contribute to the positive trend observed for Na_2O, K_2O, Rb, and Sr. Sc shows a positve correlation with MgO which can also be contributed to Amp or probably Px fractionation.

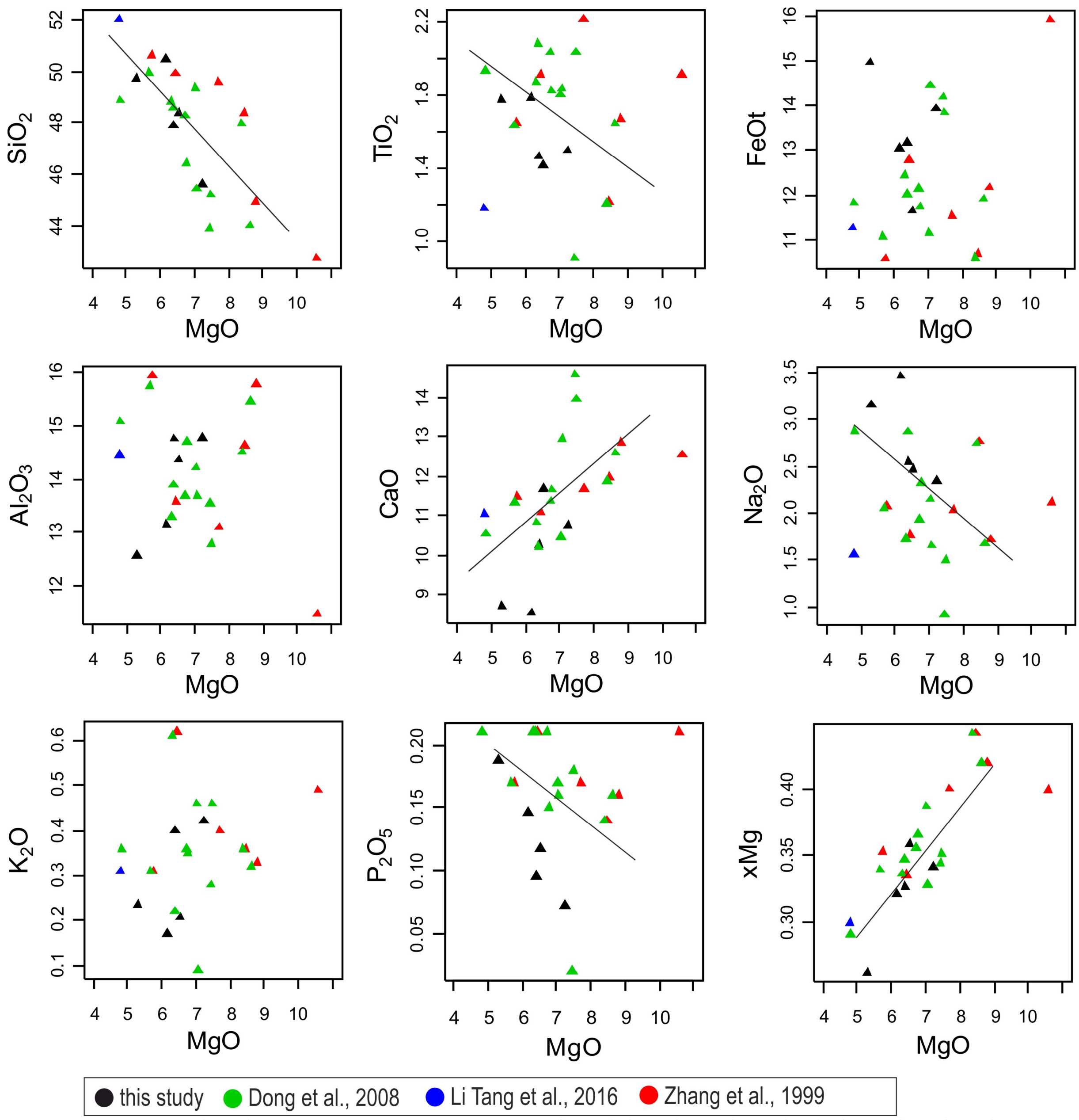

Fig. 30 amphibolites of the Songshugou ophiolite, majors vs MgO i.e. SiO_2, TiO_2, FeO_t, Al_2O_3, CaO, Na_2O, K_2O, P_2O_5, XMg.

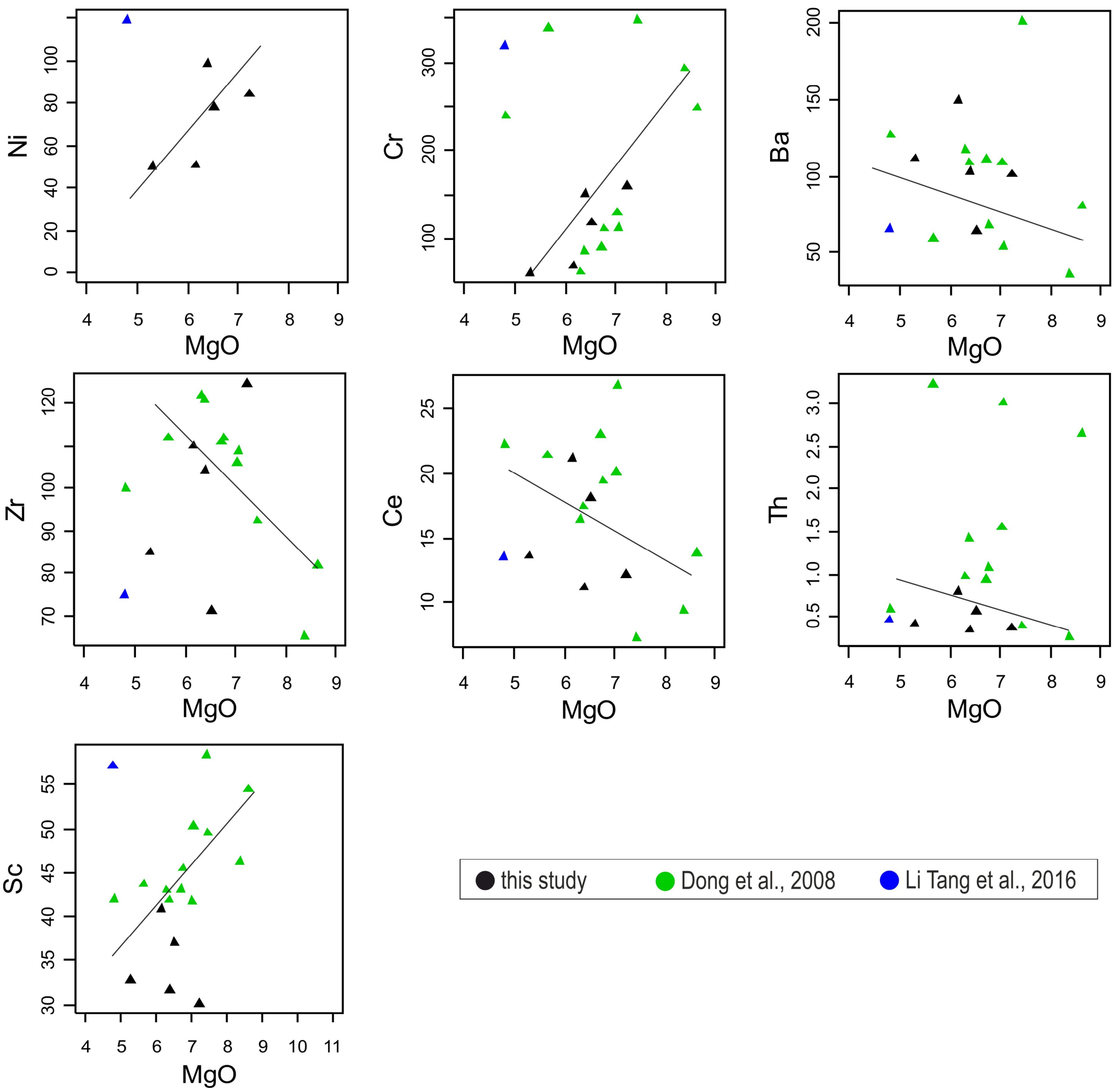

Fig. 31 amphibolites of the Songshugou ophiolite, traces vs MgO i.e. Ni, Cr, Ba, Zr, Ce, Th, Sc.

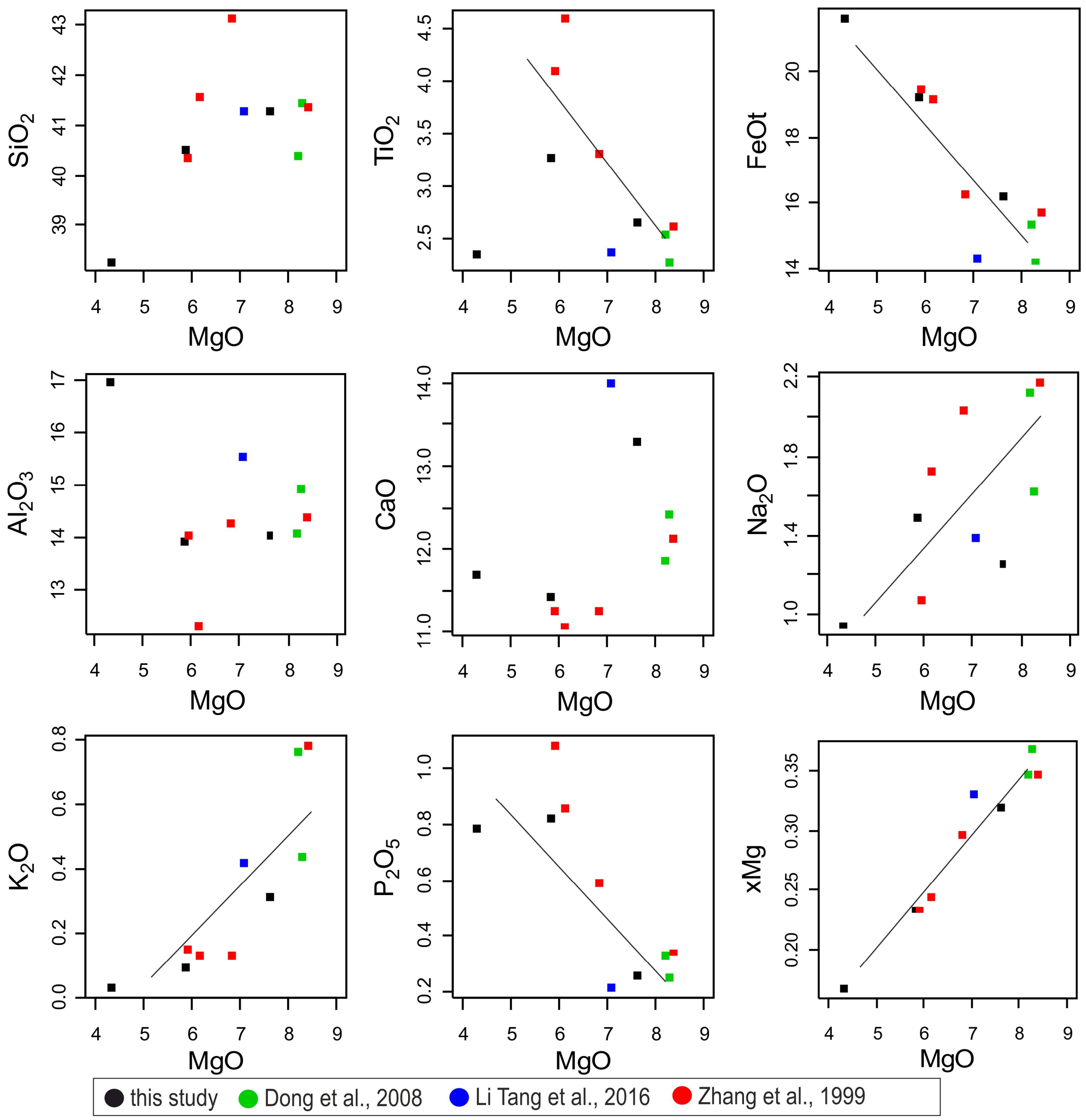

Fig. 32 Grt amphibolites of the Songshugou ophiolite, majors vs MgO i.e. SiO_2, TiO_2, FeO_t, Al_2O_3, CaO, Na_2O, K_2O, P_2O_5, XMg.

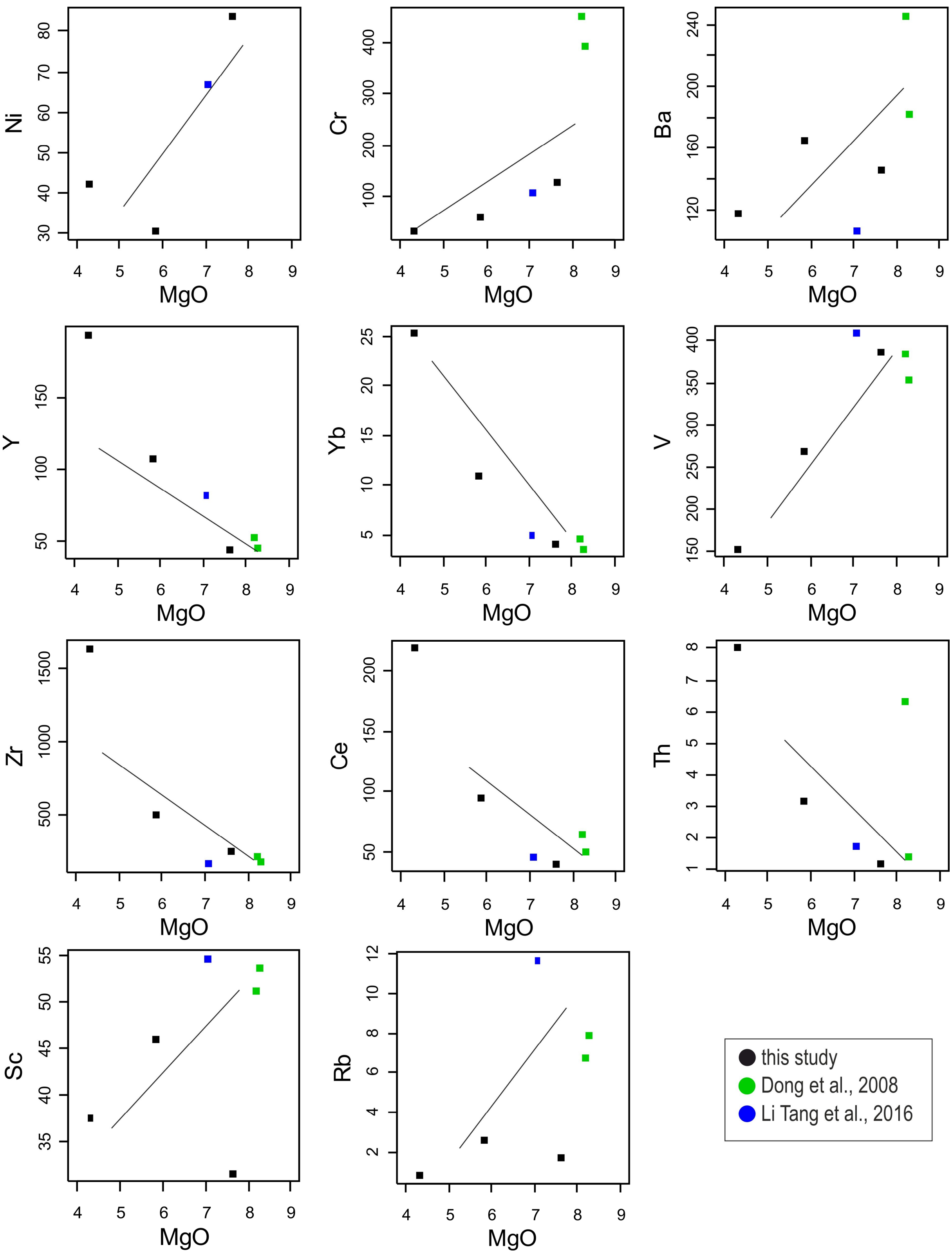

Fig. 33 Grt amphibolites of the Songshugou ophiolite, traces vs MgO i.e. Ni, Cr, Ba, Yb, Y, V, Zr, Ce, Th, Sc, Rb.

9.2 REE geochemistry and spider diagrams

The REE patterns of metamorphic rocks might be affected by metamorphism, however, HFSE including the REEs are considered as immobile elements even during metamorphic overprint. REE plotted against Zr is considered as one of the most valid tests to assess possible alteration or metamorphic effects on the REE geochemistry (Fig. 34) (Pearce and Cann, 1973; Pearce, 1975; Frey, 1983; Frey and Green, 1974; Frey et al., 1978). REE abundances increase systematically along with increasing Zr, suggesting that REE patterns haven't changed significantly by alteration and metamorphism.

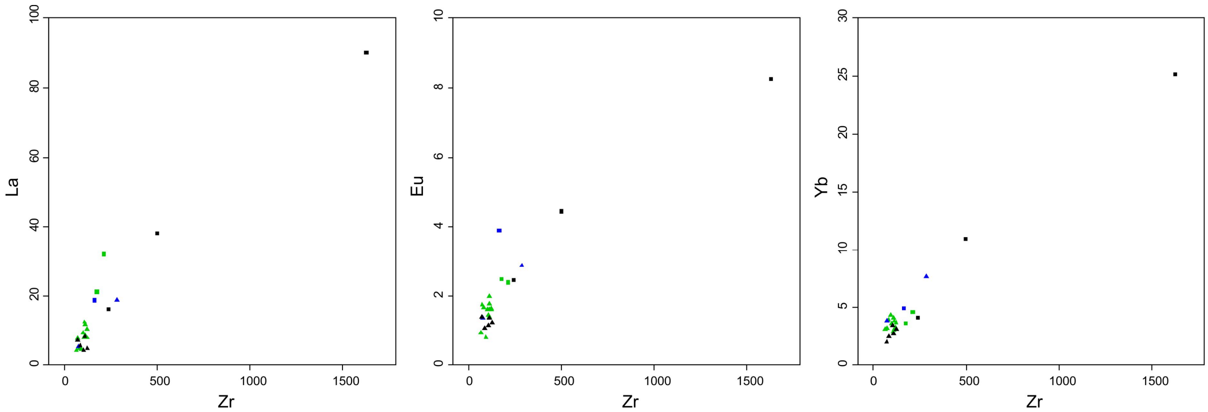

Fig. 34 Zr vs REE (in ppm) of metabasic rocks from the Songshugou ophiolite

REE were normalised to chondritic values after Nakamura 1974, who used the average value of ten common stony chondrites (3 carbonaceous (Orgueil C1, Murchison C2 and Allende C3) and 7 ordinary olivine-bronzite H chondrites). Normalisation to chondritic standards eliminates the Oddo-Harkins effect and the resulting REE diagram can directly be compared to primordial solar system composition. Grt amphibolites and amphibolites show distinctive REE_N patterns and distributions. Grt amphibolites show higher abundances of REE with $\sum REE_N$ of 130 – 700 and show higher overall REE fractionation with La_N/Yb_N of 2.3 – 4.6. Amphibolites have $\sum REE_N$ of 48 – 70 with a lower La_N/Yb_N 0.8 – 2. Those fractionation patterns are visualized in chondrite normalized REE plots (Fig. 35) where Grt-amphibolites in general show a stronger enrichment of REEs with highly enriched LREEs similar to trends observed in EMORB and OIB but with higher overall REE abundance. In most Grt amphibolites, heavy LREEs and HREEs display a plateau like pattern with Tb_N/Yb_N = 1 – 2. Amphibolites are far less enriched in REEs and hardly show overall REE fractionation. The REE concentrations of Grt amphibolites also increase along with increasing differentiation; which is shown in the $\sum REE_N$ vs. MgO diagram, in contrast to amphibolites that retain constant values of $\sum REE_N$ along with increasing MgO (Fig. 36). Grt-amphibolites are enriched in LREE as well as in other HFSE such as TiO_2 and P_2O_5. These enrichment patterns of LREE could not be easily caused by partial melting, or fractional crystallization, to that extent; and therefore, a different mantle source for Grt amphibolites seems very likely. Grt amphibolites exhibit stronger LREE fractionation with La_N/Sm_N ratios of 1.4 – 2.6. This is typical of E-MORB in contrast to amphibolites with lower La_N/Sm_N ratios of 0.8-1.3, and is supported by the Zr-Nb-Y discrimination plot after Meschede, where the majority of Grt-amphibolites plot in the E-MORB field (Fig. 46c). Some of the Grt-amphibolites show an insignificant negative Eu anomaly probably attributed to minor Pl fractionation. Crustal contamination causing elevated LREEs seems very unlikely since Grt-amphibolites are very low in SiO_2, K_2O, Na_2O, K and Rb, but they exhibit higher FeOt and account of high Ni contents in some low MgO samples. Furthermore rocks affected by crustal contamination usually show a trough in Nb and Ta in chondrite normalized spider plots, which is not observed in garnet amphibolites of the Songshugou metabasic unit. The phenomenon of Nb and Ta troughs occurs in all crustal contaminated rocks as well as subduction related magmatic rocks, since Nb and Ta often is locked into Ti bearing phases such as Ilm and Spn which hardly play a role in crustal contamination due to their refractory nature. Suspicious troughs of Rb, K, Sr in the chondrite normalized spider plot of Grt amphibolites could be caused by Amp fractionation (Fig. 37).

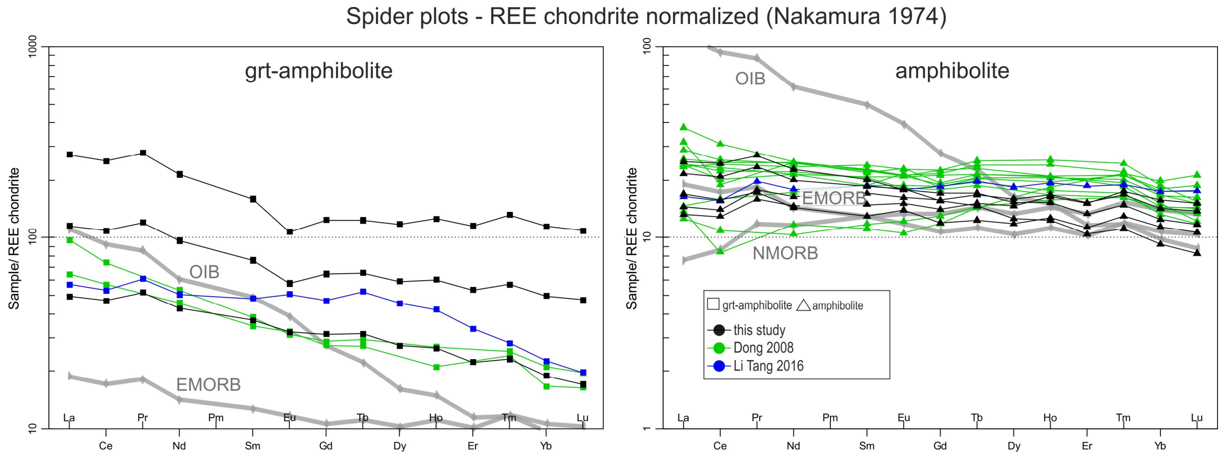

Fig. 35 REE chondrite normalized spider plots of Grt-amphibolites and amphibolites from the Songshugou metabasic unit (Nakamura 1974)

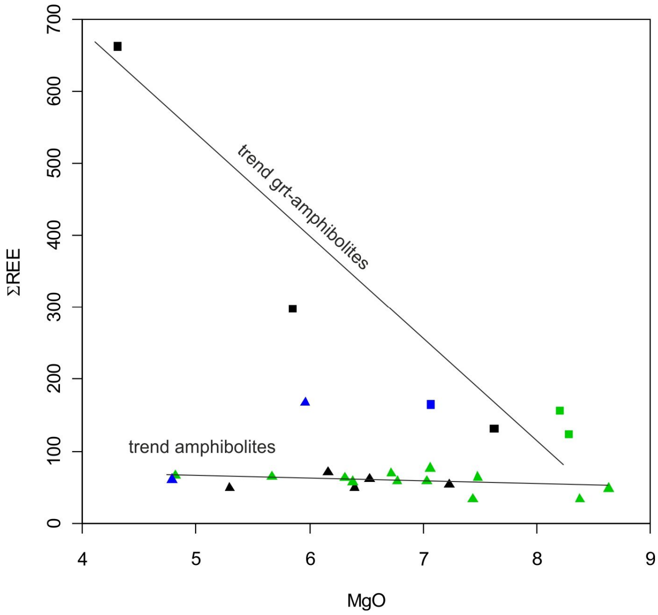

Fig. 36 MgO vs sum_REE$_N$ (Nakamura 1976)

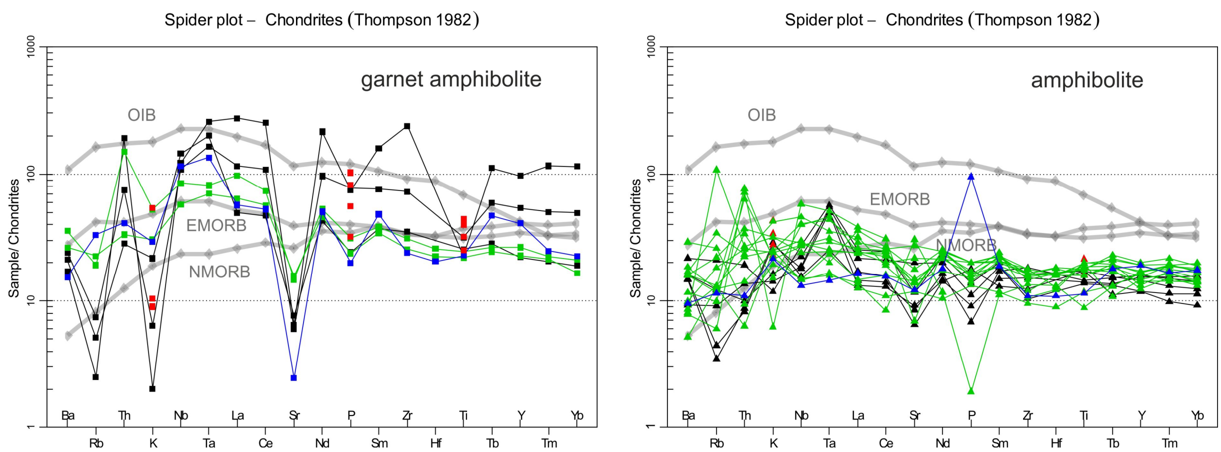

Fig. 37 chondrite normalized spider plot after Thompson 1982

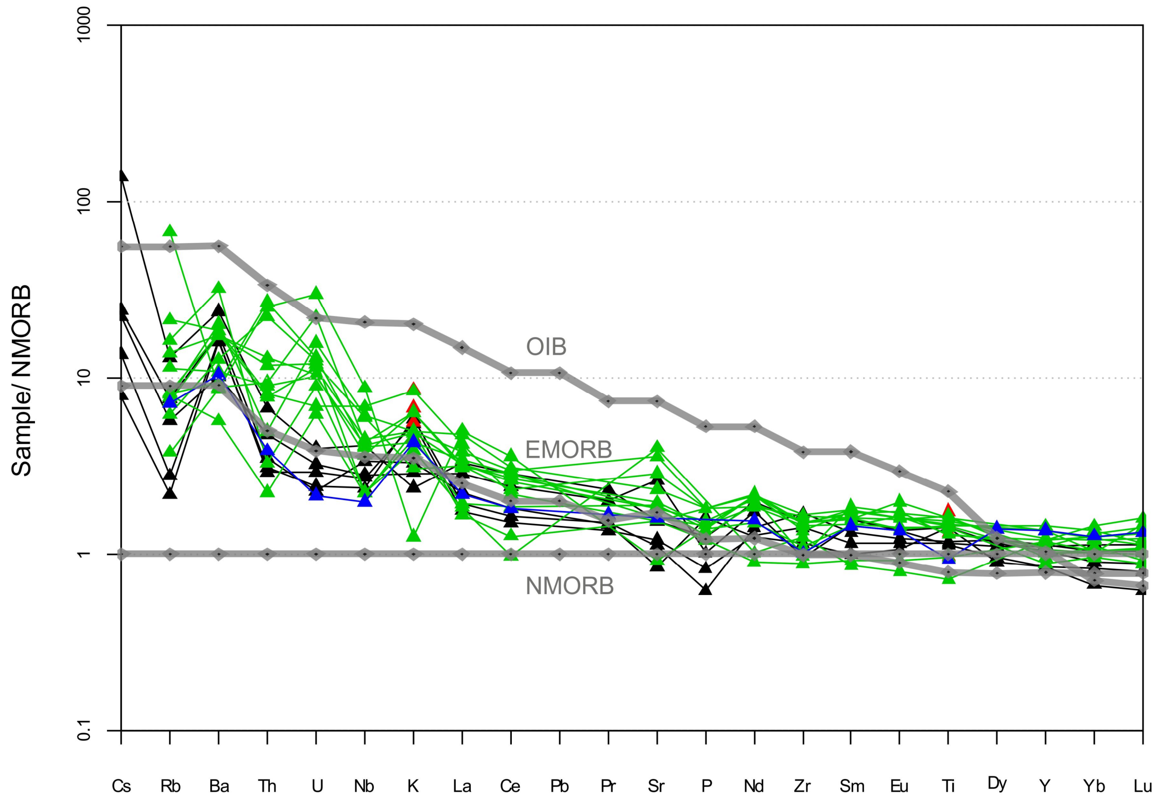

Fig. 38 Amphibolite NMORB normalized after Sun and McDonough 1989. NMORB, EMORB and OIB data after Sun and McDonough 1989

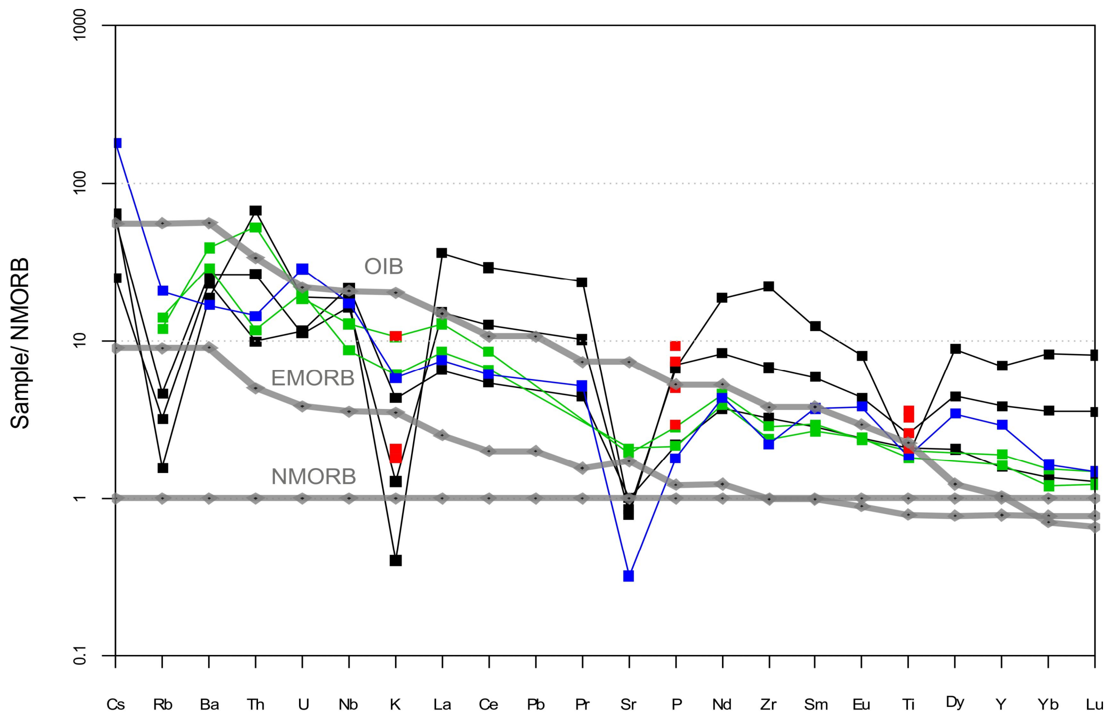

Fig. 39 Garnet amphibolite NMORB normalized after Sun and McDonough 1989. NMORB, EMORB and OIB data after Sun and McDonough 1989.

9.3 Discrimination diagrams

In the TAS diagram, amphibolites plot in the field of subalkaline basalt; the majority of Grt-amphibolites in the alkaline field (Fig. 40, Fig. 44b). In the Al_2O_3 - TiO_2 discrimination diagram after Pearce 1983, amphibolite data plot as basalt and garnet-amphibolite data mainly as Fe-Ti basalt (Fig. 41). None of the samples fall in the cumulate field. In the TiO_2-K_2O-P_2O_5 discrimination diagram proposed by Pearce 1975 most samples plot into the field of oceanic basalts (Fig. 42). This diagram is only effective for primitive basalts; therefore all analyses were plotted in the AFM diagram (Fig. 44a) where an isoalkaline line of 20 % functions as recommended upper limit (Pearce et al., 1975). On the triangular 100 mg – c – al+alk (mg = MgO/(FeO+MnO+2Fe_2O_3+MgO), other Niggli values are oxides converted to their equivalent molecular numbers i.e. CaO = c, Al_2O_3 = al and SrO, BaO, Li_2O, Rb_2O, Na_2O and K_2O = alk) diagram after Leake et al. 1964, all samples plot along the basic igneous trend line between middle and late stage differentiation (Fig. 43).

Post-depositional processes can also affect the mobility of certain elements. Therefore data was plotted in the CaO/Al_2O_3-MgO-SiO_2 diagram proposed by Schweitzer and Kröner 1985 (Fig. 44b). All samples plot in the field of 'unaltered basalts'. The ternary AFM diagram suggests an association of a tholeiitic magmatic trend for all samples, which is typically observed at mid ocean ridge submarine volcanism (Fig. 44). That is substantiated by the ternary Zr+Y-Cr-TiO_2 plot after Davies et al. 1979 where most samples plot close to the tholeiitic trend line (Fig. 44c). REE, HFSE (high field strength elements) as well as some transition metals remain immobile during most hydrothermal alterations in contrary to LIL (large ion lithophile) elements like Na, K, Sr, Rb, Ba, U being mobile even under low-grade metamorphic conditions. (Pearce, 1984; Camire et al., 1995; Swinden et al., 1990; Schiano et al., 1993). Hence, Davies diagram might be of more significance than the AFM diagram, as it is based on immobile trace elements which more likely represent original igneous trends. The discrimination scheme of Jensen 1976 allows subdividing the samples furthermore. The majority of samples plot in the field of 'high Fe tholeiite basalt' (Fig. 45). Discrimination diagrams after Pearce & Cann1973, Wood 1980 and Meschede 1986, employing immobile trace elements, classify most metabasic samples of the Songshugou ophiolite as E-MORB (Fig. 46). That is substantiated by the Ta/Yb vs. Th/Yb plot after Pearce 1983. Vectors drawn into the diagram illustrate the influence of subduction components (S), within-plate enrichment (W), crustal contamination (C) and fractional crystallization (f). Most of the samples follow the mantle array (Fig. 47).

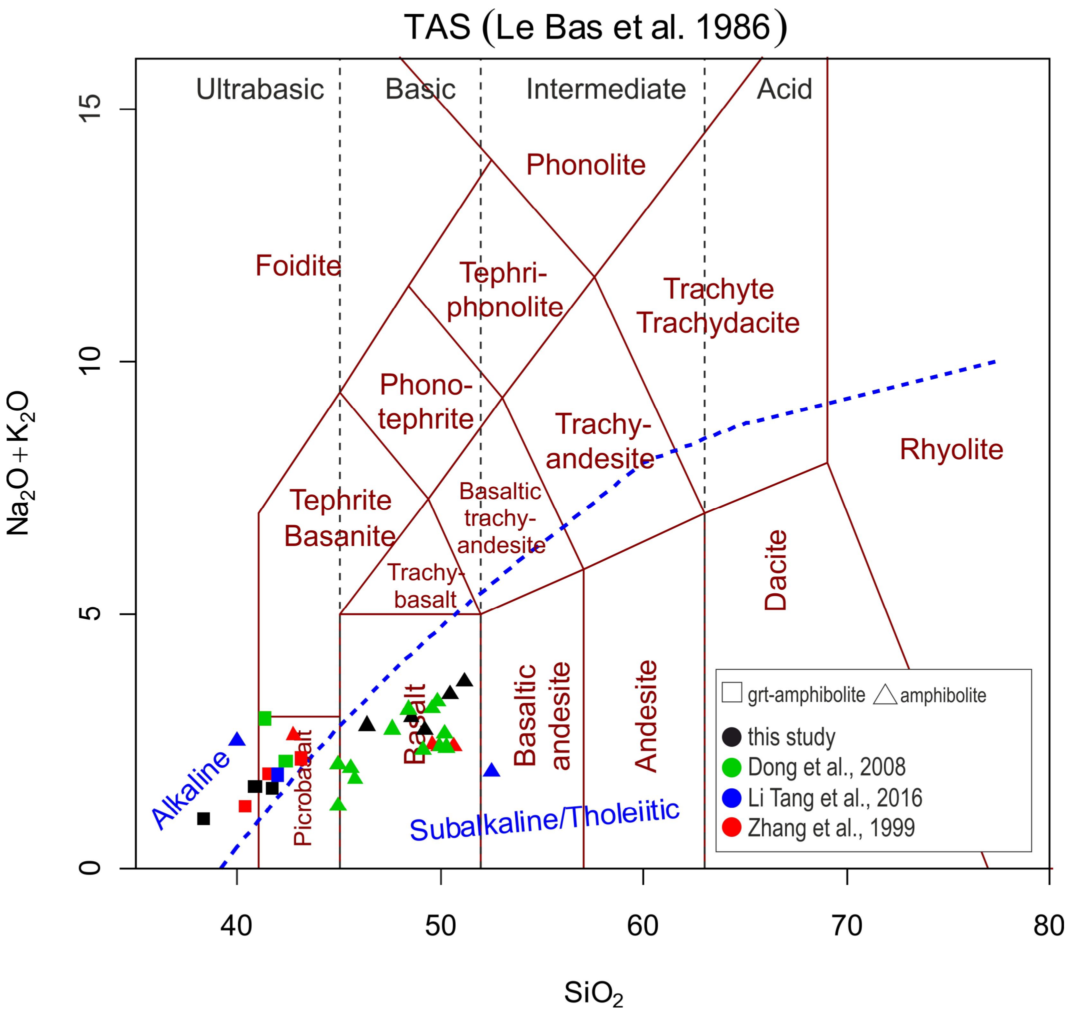

Fig. 40 TAS diagram after le Bas et al. 1986. Plots with rectangular shape represent Grt amphibolites, and triangular ones amphibolites.

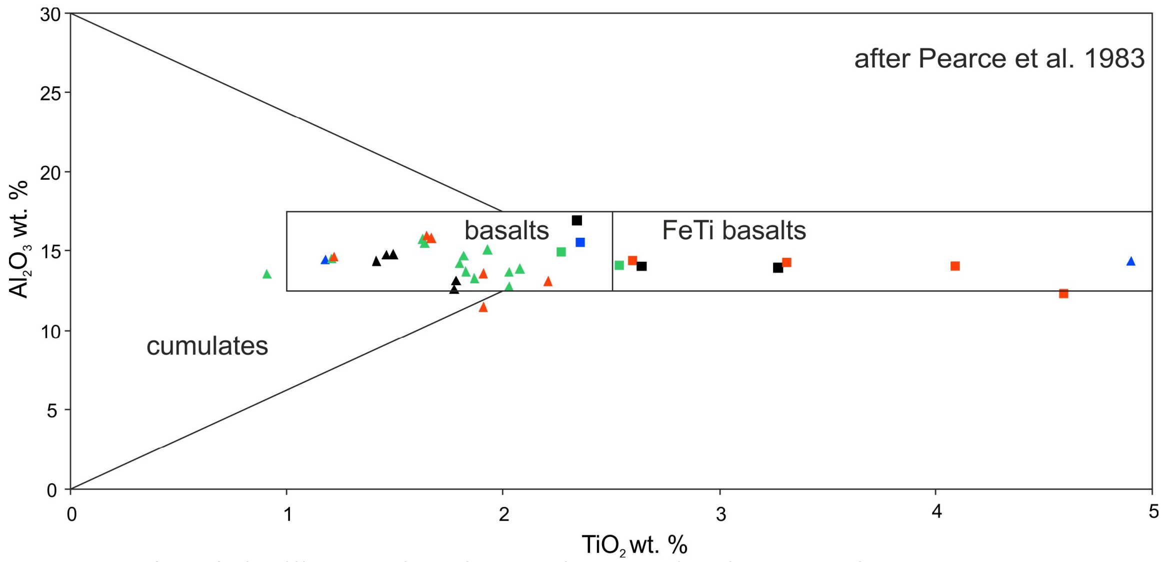

Fig. 41 binary Al_2O_3 - TiO_2 (wt. %) diagram for mafic rocks after Pearce (1983). The area of cumulates represents a mixture of Ol, Pl and basaltic melt. Whole rock analyses of the Songshugou metabasites are plottet into the diagram. Sympology of data points according to legend in **Fig. 40**.

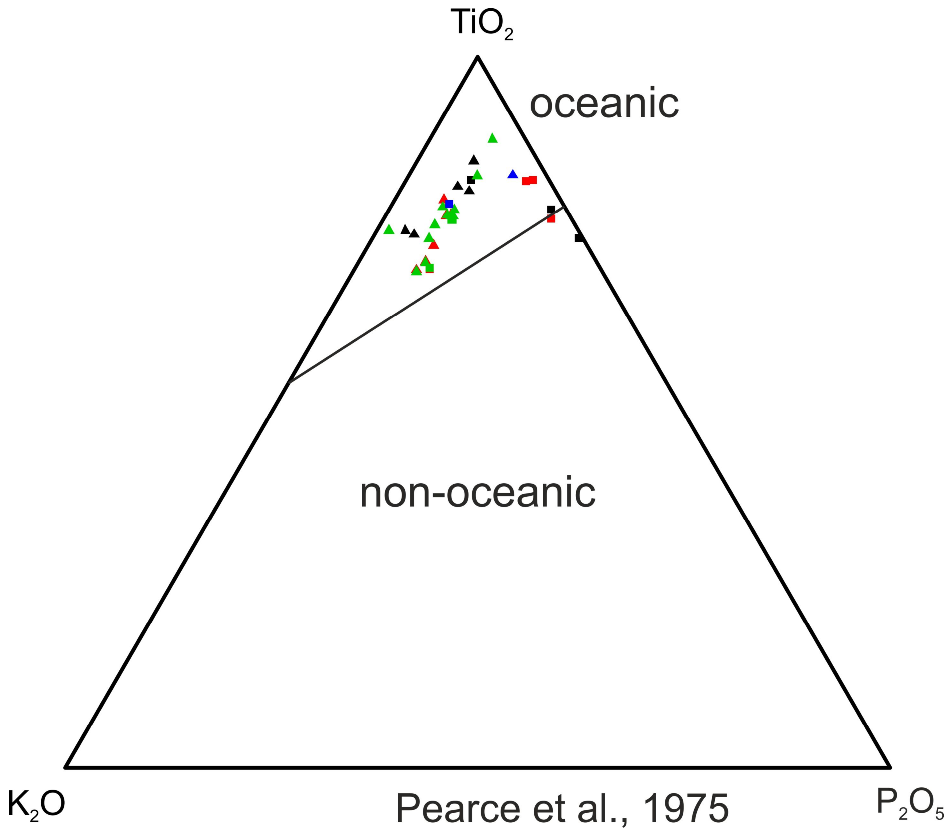

Fig. 42 Proposed ternary TiO_2-K_2O-P_2O_5 plot for discrimination between oceanic and continental basalt after Pearce et al., 1975. The separating line has the following coordinates: TiO_2 54.5%, and TiO_2 79.6%, P_2O_5 20.4 %. Alteration and metamorphism of oceanic basalts generally contribute to enrichment of K_2O relative to TiO_2 and P_2O_5.

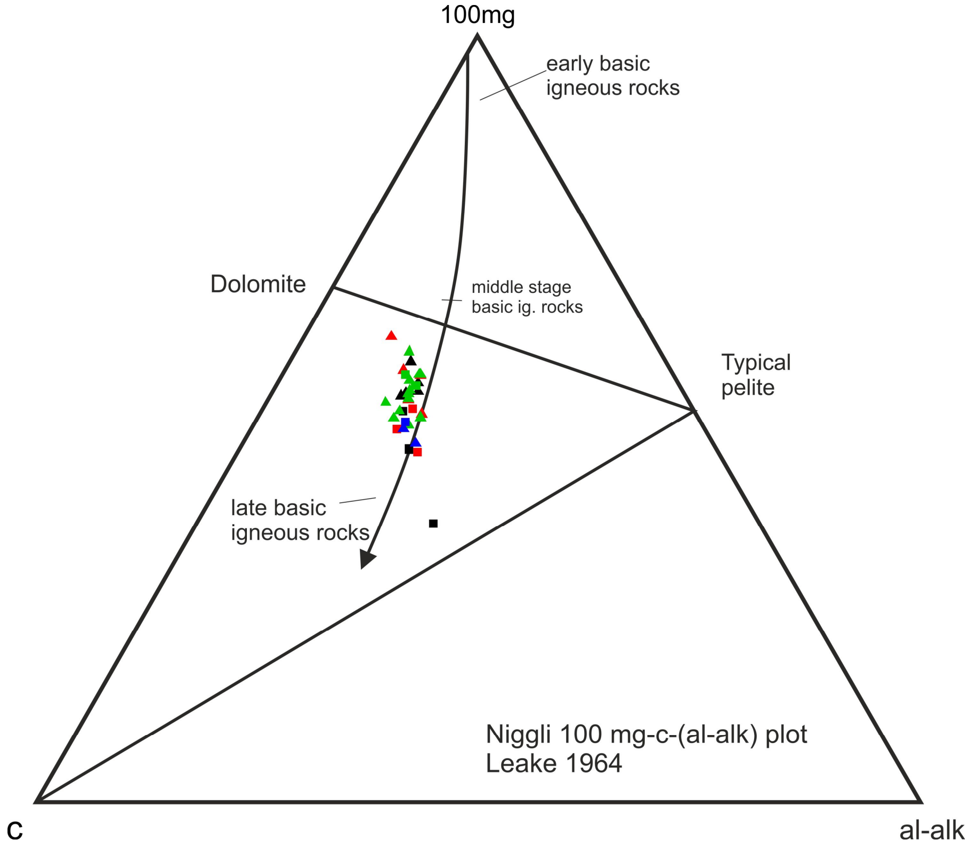

Fig. 43 100mg - c - al-alk triangular diagram after Leake 1964. Niggli parameters are displayed in **table 27**. Data is plotted along basic igneous trend line.

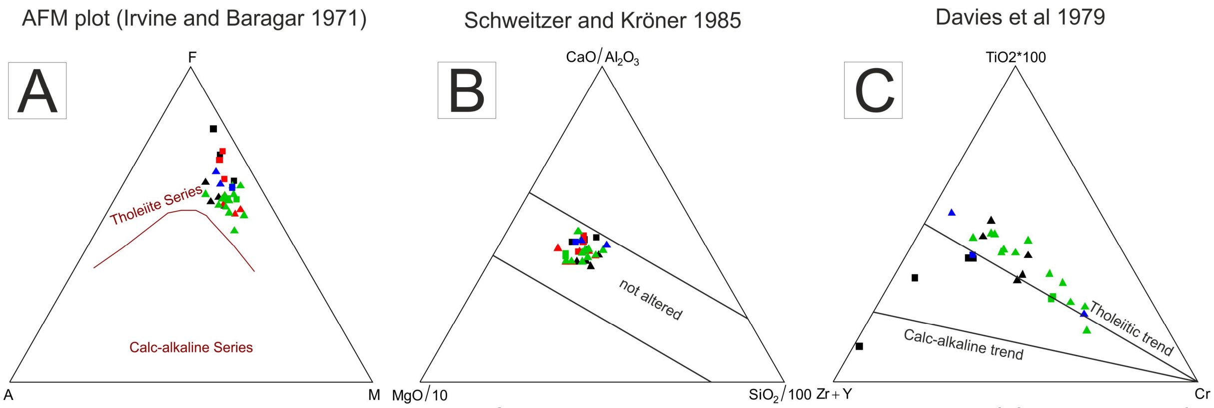

Fig. 44 Plots with rectangular shape representing Grt amphibolites, and triangular ones amphibolites. **(A)** AFM diagram after Irvine and Baragar 1971, **(B)** TiO_2-Zr+Y-Cr diagram after Davies et al. 1979 sustaining tholeiitic affinity of Songshugou metabasites. **(C)** CaO/Al_2O_3-MgO-SiO_2 diagram after Schweitzer and Kröner 1985 showing unaltered geochemistry of Songshugou metabasic rocks.

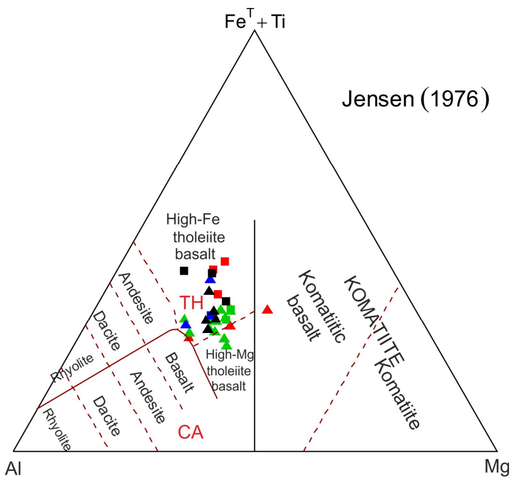

Fig. 45 Cationic discrimination scheme after Jensen 1976. Samples plot in High-Fe tholeiitic basalt field. Sympology of data points according to legend in Fig. 40.

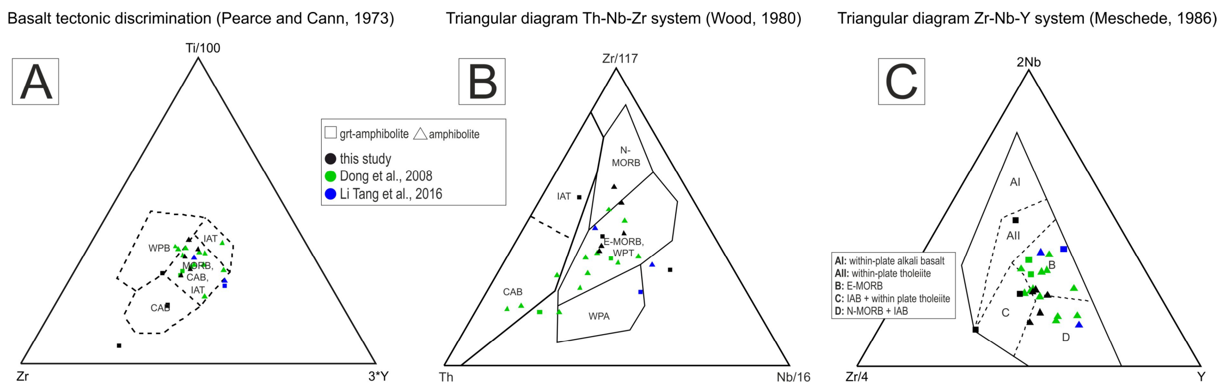

Fig. 46 discrimination diagrams for basalts. Grt amphiboles, plotted as rectangles, tend to diverge from amphibolite data **(A)** ternary Zr-Y-Ti plot after Pearce and Cann 1973. Most data plots in the field of MORB. **(B)** Discrimination diagram Th-Nb-Zr after Wood 1980. Samples mainly plot in the E-MORB field. **(C)** Zr-Nb-Y triangular diagram after Meschede 1986 with data plotting within E-MORB field and to lesser extend in the N-MORB field.

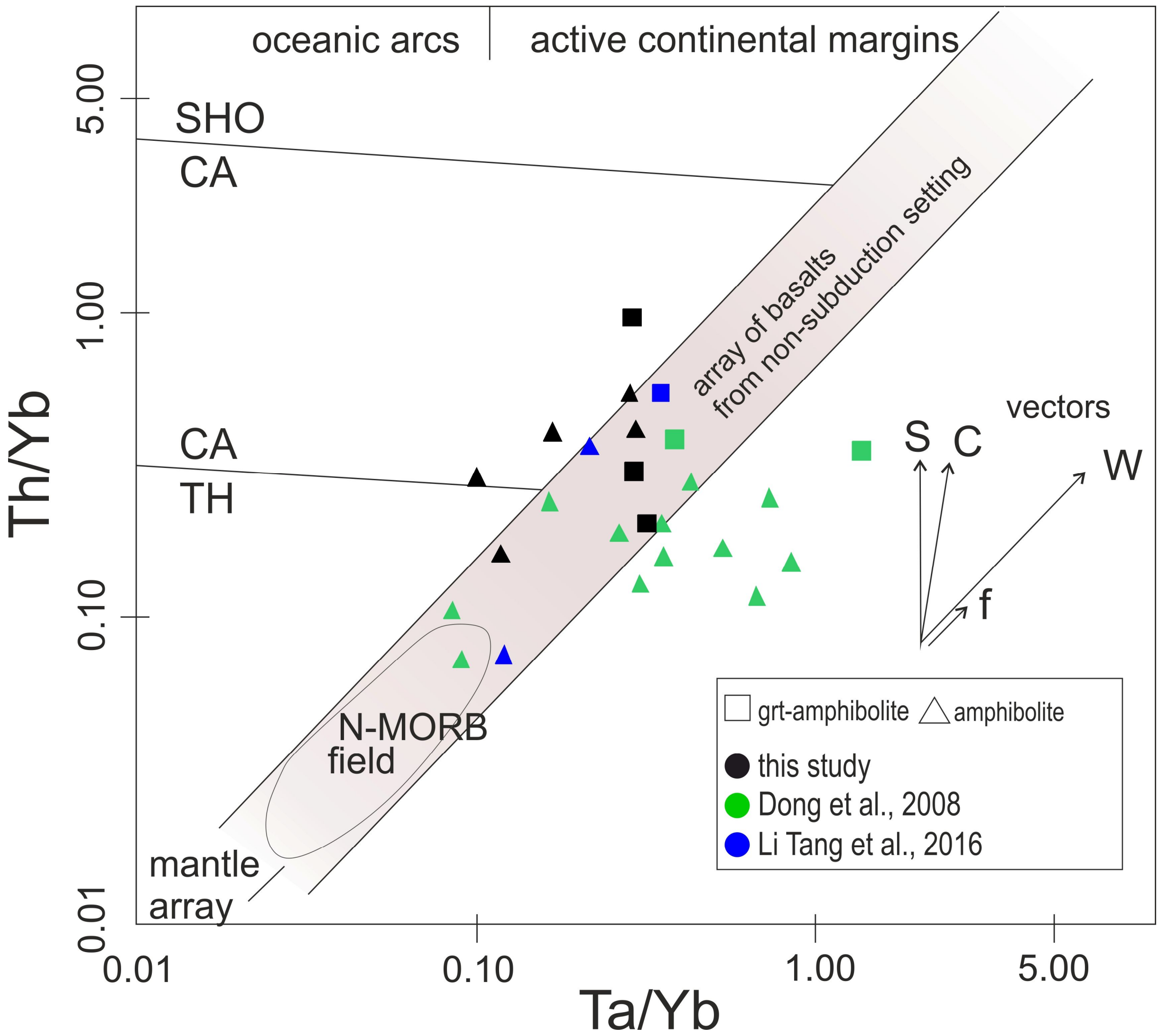

Fig. 47 Ta/Yb versus Th/Yb (Pearce, 1983), used symbology right at the bottom. Vectors show the influence of subduction components **(S),** within-plate enrichment **(W),** crustal contamination **(C)** and fractional crystallization **(f).** Tholeiitic **(TH)**, calc-alkaline **(CA)** and shoshonitic **(SHO).**

table 27 Whole rock major and trace elemental compositions for various rock types from the Songshugou ophiolite. Trace elements and REEs were obtained by ICP-MS. Trace elements given in ppm.

	garnet-amphibolite			amphibolite				
Sample	X 35	X 36	X 37	X 38	X 39	X 382	X 42	QS2D
SiO_2 (%)	40.51	41.25	38.27	47.89	49.75	45.60	50.50	48.38
TiO_2 (%)	3.27	2.64	2.34	1.46	1.78	1.49	1.78	1.42
Al_2O_3 (%)	13.94	14.04	16.94	14.75	12.58	14.78	13.15	14.36
Fe_2O_3t (%)	21.36	17.98	24.01	14.64	16.65	15.50	14.51	12.94
MnO (%)	0.42	0.24	0.62	0.21	0.26	0.22	0.25	0.20
MgO (%)	5.85	7.62	4.31	6.40	5.30	7.23	6.16	6.53
CaO (%)	11.42	13.29	11.69	10.27	8.72	10.76	8.54	11.68
Na_2O (%)	1.49	1.25	0.94	2.55	3.15	2.34	3.45	2.47
K_2O (%)	0.09	0.31	0.03	0.40	0.24	0.42	0.17	0.21
P_2O_5 (%)	0.82	0.26	0.79	0.10	0.19	0.07	0.15	0.12
LOI (%)	0.09	0.39	0.23	0.30	0.36	0.38	0.25	0.49
Sum (%)	99.17	98.90	99.94	98.65	98.62	98.41	98.66	98.31
^{7}Li	8.42	4.29	9.41	13.3	4.27	12.9	30.1	12.4
^{9}Be	0.98	1.41	0.36	0.62	0.49	0.64	0.49	0.37
^{49}Ti	46.0	31.6	37.4	31.6	32.8	30.1	40.9	37.1
^{51}V	268	386	153	298	454	299	312	303
^{53}Cr	59.0	127	31.6	151	62.0	160	69.7	118
^{55}Mn	72.5	78.4	67.2	84.1	83.2	60.6	77.2	86.5
^{59}Co	30.6	83.7	42.1	98.9	50.2	84.2	50.7	78.1
^{60}Ni	105	25.0	31.5	31.8	55.9	33.0	115	179
^{66}Zn	139	177	82.2	104	115	114	104	84.8
^{71}Ga	20.3	25.7	17.2	17.8	19.6	18.4	17.9	19.4
^{85}Rb	2.60	1.79	0.87	1.56	4.29	1.21	7.29	3.20
^{88}Sr	70.7	90.0	76.4	108	76.1	100	137	234
^{89}Y	108	44.1	194	30.6	23.7	31.6	29.2	23.6
^{90}Zr	499	240	1628	104	84.9	125	110	71.1
^{93}Nb	37.9	50.7	42.8	6.29	7.83	5.47	9.54	6.54
^{133}Cs	0.41	0.17	0.45	0.10	0.17	0.05	0.97	0.15
^{137}Ba	165	146	118	103	111	101	150	63.9
^{139}La	38.0	16.3	90.0	4.37	5.60	4.77	8.27	7.15
^{140}Ce	94.1	40.6	218	11.2	13.6	12.1	21.2	18.1
^{141}Pr	13.4	5.80	31.1	1.78	1.94	1.99	3.03	2.63
^{146}Nd	60.8	26.9	135	9.20	9.03	10.3	14.4	12.6
^{147}Sm	15.5	7.52	32.4	3.03	2.62	3.46	4.08	3.76
^{153}Eu	4.44	2.46	8.25	1.16	1.07	1.25	1.37	1.39
^{157}Gd	17.8	8.62	34.1	3.88	3.30	4.34	4.71	4.29
^{159}Tb	3.07	1.47	5.79	0.71	0.58	0.79	0.80	0.69
^{163}Dy	20.6	9.31	40.2	5.04	4.05	5.50	5.27	4.30
^{165}Ho	4.22	1.84	8.79	1.15	0.89	1.18	1.07	0.87
^{166}Er	12.0	5.00	25.9	3.40	2.54	3.43	3.00	2.35
^{169}Tm	1.71	0.69	3.94	0.53	0.39	0.51	0.45	0.33
^{172}Yb	10.9	4.16	25.2	3.46	2.50	3.13	2.74	2.03
^{175}Lu	1.61	0.58	3.69	0.52	0.36	0.47	0.40	0.28
^{178}Hf	-	-	-	-	-	-	-	-
^{181}Ta	3.30	4.00	5.13	1.00	1.02	0.51	1.14	1.10
^{208}Pb	-	-	-	-	-	-	-	-
^{232}Th	3.16	1.19	8.00	0.35	0.42	0.37	0.80	0.57
^{238}U	0.52	0.54	0.88	0.13	0.11	0.11	0.19	0.15

Niggli parameters calculated after Leake et al., 1964

	garnet-amphibolite			amphibolite				
Sample	X 35	X 36	X 37	X 38	X 39	X 382	X 42	QS2D
si	86.01	84.14	78.98	111.01	122.50	100.44	124.17	112.12
al	17.44	16.88	20.61	20.15	18.26	19.18	19.05	19.61
fm	53.39	51.19	51.63	48.04	50.84	49.84	49.96	45.52
c	25.97	29.05	25.84	25.51	23.02	25.39	22.49	29.01
alk	3.19	2.89	1.93	6.31	7.89	5.59	8.50	5.85
k	0.04	0.14	0.02	0.09	0.05	0.11	0.03	0.05
mg	0.35	0.45	0.26	0.46	0.38	0.48	0.45	0.50
c/fm	5.22	4.06	3.64	2.55	3.29	2.48	3.30	2.47
ti	0.74	0.22	0.69	0.09	0.20	0.07	0.15	0.12
p	0.49	0.57	0.50	0.53	0.45	0.51	0.45	0.64

chondrite normalized REEs after Nakamura 1974

	garnet-amphibolite			amphibolite				
Sample	X35	X36	X37	X38	X39	X382	X42	QS2D
La_N	115.27	49.28	272.84	13.24	16.98	14.46	25.06	21.66
Ce_N	108.79	46.89	251.92	12.90	15.70	14.01	24.49	20.89
Pr_N	120.02	51.77	277.92	15.91	17.31	17.77	27.03	23.45
Nd_N	96.44	42.74	214.93	14.61	14.33	16.42	22.83	20.06
Pm_N	NA	NA	NA	NA	NA	NA	NA	NA
Sm_N	76.10	37.03	159.56	14.91	12.92	17.06	20.12	18.53
Eu_N	57.68	31.95	107.16	15.10	13.95	16.19	17.86	18.09
Gd_N	64.62	31.22	123.55	14.08	11.95	15.71	17.05	15.55
Tb_N	65.43	31.30	123.28	15.17	12.34	16.81	17.13	14.70
Dy_N	59.05	27.15	117.26	14.69	11.80	16.02	15.36	12.55
Ho_N	60.27	26.34	125.61	16.40	12.66	16.79	15.29	12.36
Er_N	53.24	22.23	115.08	15.10	11.29	15.25	13.32	10.45
Tm_N	56.97	23.13	131.47	17.57	12.93	16.87	14.83	11.13
Yb_N	49.63	18.90	114.54	15.71	11.38	14.25	12.45	9.20
Lu_N	47.35	17.00	108.62	15.18	10.65	13.79	11.71	8.26
Eu/Eu*	0.82	0.94	0.76	1.04	1.12	0.99	0.96	1.07
La_N/Yb_N	2.32	2.61	2.38	0.84	1.49	1.02	2.01	2.35
Tb_N/Yb_N	1.32	1.66	1.08	0.97	1.08	1.18	1.38	1.60
La_N/Sm_N	1.51	1.33	1.71	0.89	1.31	0.85	1.25	1.17
Ce_N/Yb_N	2.19	2.48	2.20	0.82	1.38	0.98	1.97	2.27
Ce_N/Sm_N	1.43	1.27	1.58	0.87	1.21	0.82	1.22	1.13
Eu_N/Yb_N	1.16	1.69	0.94	0.96	1.23	1.14	1.43	1.97
Sum_REE	297.84	131.20	662.76	49.38	48.45	53.27	70.75	60.78

10 Pseudosections

The evaluation of the P-T evolution of mafic HP rocks was complicated due to the high number of variances, and the refractory nature of the mineralogy. Growth zoning conserved in garnets is widely regarded as evidence for a change in effective bulk composition during metamorphism similar to fractional crystallisation (Marmo et al., 2002). Hence, the effective bulk composition which applies to matrix phases depends on the amounts of elements already fractionated into garnets, and the transport rate of these elements (Carlson, 1989; Chernoff and Carlson 1997).

In order to model metamorphic evolution of the investigated area, pseudosections were calculated for selected samples. The Gibbs free energy minimization software package Perple_X version 6.7.3 (Connolly, 2005, updated in 2016) and the internally consistent thermodynamic data set hp04ver.dat (Holland and Powell, 1998, revised in 2004) was used. Plots of mineral modes and isopleths of mineral compositions were obtained by the program PyWerami version 2.0.1 (Lexa, 2011). The chemical system MnO-Na_2O-CaO-FeO-MgO-Al_2O_3-SiO_2-H_2O-TiO_2 (MnNCFMASHT) was applied with the following solution models: orthopyroxene (Holland and Powell, 1999), chlorite (Holland et al., 1998), amphibole (Holland and Powell, 1998), feldspar (Benisek et al., 2010), spinel (Holland and Powell, 1998), garnet (Ganguly, Cheng & Tirrone, 1996), clinopyroxene (Holland and Powell, 1996) and omphacite for high-pressure calculations (Diener and Powell, 2011). A water content of 1.00 wt.% was applied based on mineralogy, and an empirical correction for ferric iron (15 wt.% of total iron) content was undertaken.

Based on petrographic observations described in the previous chapters, a three stage garnet growth was concluded. The first stage of garnet growth was modelled by applying the measured bulk-rock composition. Pseudosections were calculated for the samples X35, X36 and X37 (Fig. 48, Fig. 49 and Fig. 50). Since matrix minerals are not in equilibrium with garnet core compositions, calculated isopleths for all Grt endmembers and X_{Mg} of pargasitic amphibole inclusions in garnet cores were used to obtain a PT field of initial garnet growth. In addition, the garnet-hornblende FeMg-1 exchange geothermometry, calibrated by Dale et al., (2000), further constrained PT conditions of 630°C – 740°C and 0.7 – 0.9 GPa. For the geothermometer smaller Amp grains were chosen adjoined to Grt core and no other mineral phases. The theoretical full mineral assemblage at these conditions include Amp-Pl-Grt-Cpx-Ilm-H_2O. All phases with the exception of Cpx could also be found within the garnet cores. Calculated pseudosections of X35, X36 and X37 do not differentiate significantly with isopleths intercepting at similar PT conditions.

In order to calculate the metamorphic PT evolution recorded by Rim1 and Rim2 of the garnet porphyroblasts, the effective bulk composition used in pseudosection calculation has to be adapted, since it has changed from the previously used whole rock composition by the formation and chemical fractionation of the garnet cores. At temperatures below 600–700°C all major chemical components in garnet have very low intragranular diffusivity (Chakraborty & Ganguly, 1992; Spear, 1988; Thompson & England, 1984; Tracy, 1982). Therefore pseudosections calculated for garnet rim growth were chemically adjusted in consideration of elements being locked in cores. Similar corrections have been utilized by several authors (Spear et al., 1998; Evans, 2004; Gaidies et al., 2011). Authors like Evans (2004) estimated garnet fractionation by using Mn partitioning between whole rock and garnet as proxy. Therefore, a consistent Mn distribution in garnet grains, usually described by Rayleigh fractionation, is necessary. However, Songshugou samples do not exhibit any consistant pronounced zoning in Mn due to diffusional modifications. Therefore, the chemical correction for this effect was accomplished by estimating the volume of garnet cores in thin-sections using the software package ImageJ (http://imagej.net). The chemical composition, and the variations within the garnet core, were determined by applying element profiles across the garnet core; and analyzing element distribution images. The obtained garnet core vol.% was then converted into wt.% with an estimated garnet density of 4.1 g/cm³. Chemically adjusted pseudosections of samples X35, X36 and X37 are illustrated in Fig. 51, Fig. 52 and Fig. 53, respectively. For PT estimations, calculated isopleths of Grt endmembers and isopleths of Omp (X_{Mg}, X_{Na}) were plotted into the pseudosections. For Omp isopleths, matrix Cpx analyses with highest X_{Na} values found in Cpx-Qz symplectites were taken since they are considerd to be least influenced by retrogression. In the pseudosection of sample X37, no Cpx isopleths were plotted solely because all Cpx found in matrix occurs as strongly developed symplectites and supposably yields extremely altered compositions. In the pseudosections of all three samples, isopleths intersect at 1.7 – 2.1 GPa and 570 – 640 °C, representing minimum PT conditions of a HP eclogite facies metamorphic event. This is substantiated by Cpx-Grt FeMg-1 geothermobarometric calculations (Krogh, 2000), where microprobe analyses of Grt rim and omphacitic Cpx found in Cpx-Qz symplectites in matrix resulted in a temperature window of 500 to 650°C. Within the obtained PT window the mineral assemblage Grt-Omp-Amp-Rt-H_2O±Zo, which is also observed in the samples, remained stable.

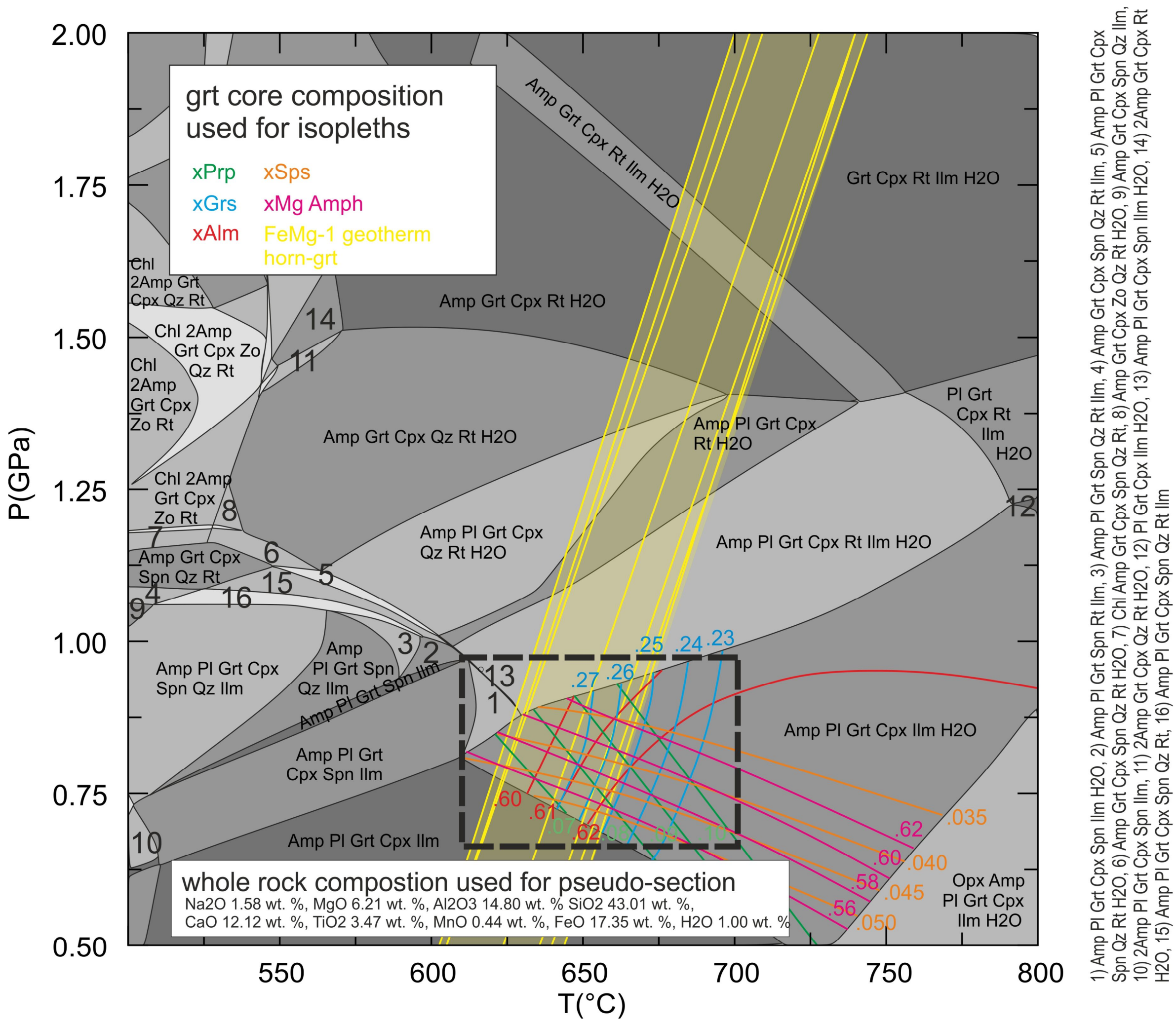

Fig. 48 Calculated pseudosection of bulk-rock composition representing initial garnet growth of sample X35. Isopleths intercept inside the dashed rectangle in the field of Amp, Pl, gt, Cpx, Ilm and H2O. Used bulk rock composition is found at the bottom of the diagram.

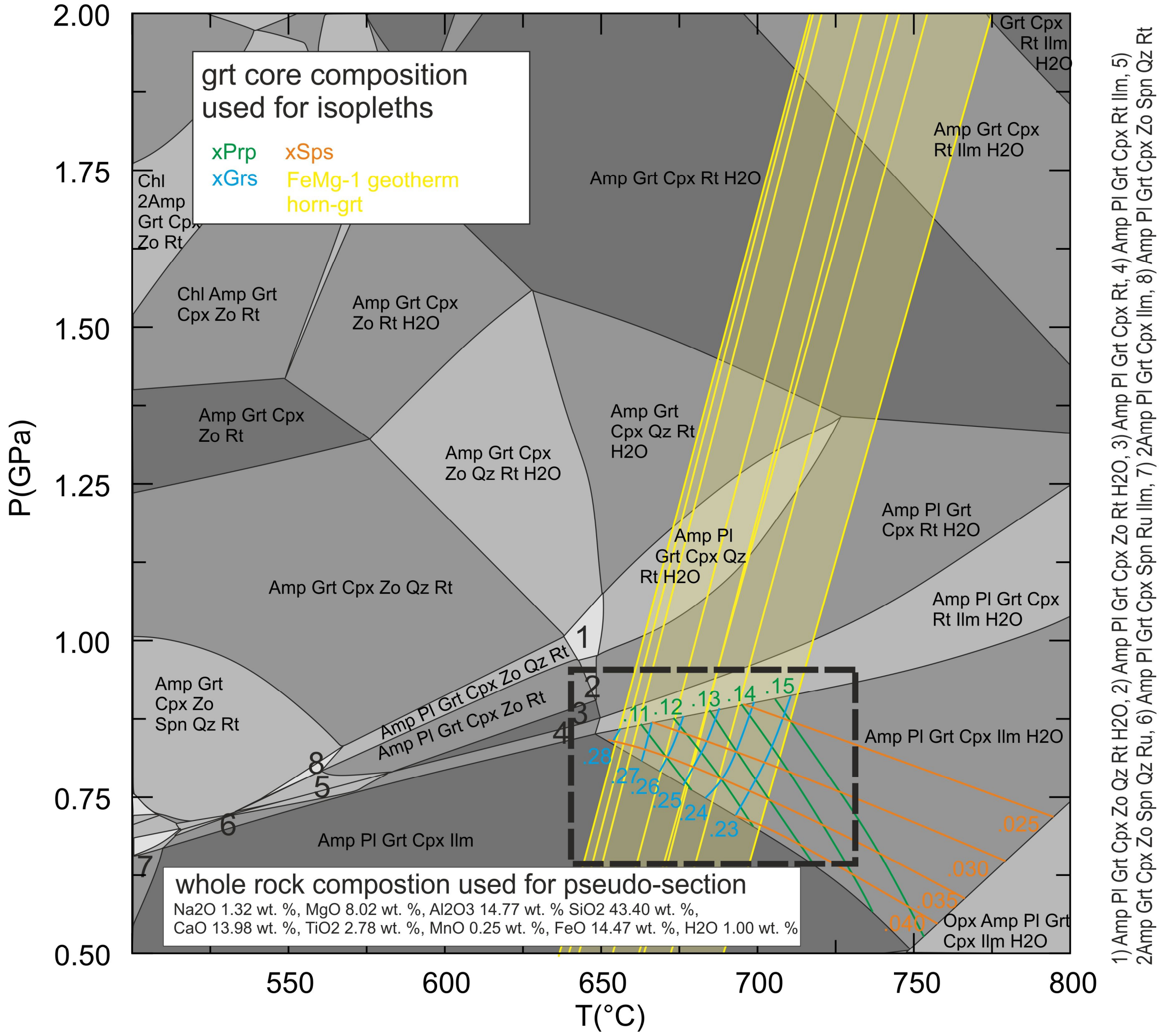

Fig. 49 Calculated pseudosection of bulk-rock composition representing initial garnet growth of sample X36. Isopleths intercept inside the dashed rectangle in the field of Amp, Pl, gt, Cpx, Ilm and H_2O. Used bulk rock composition is found at the bottom of the diagram.

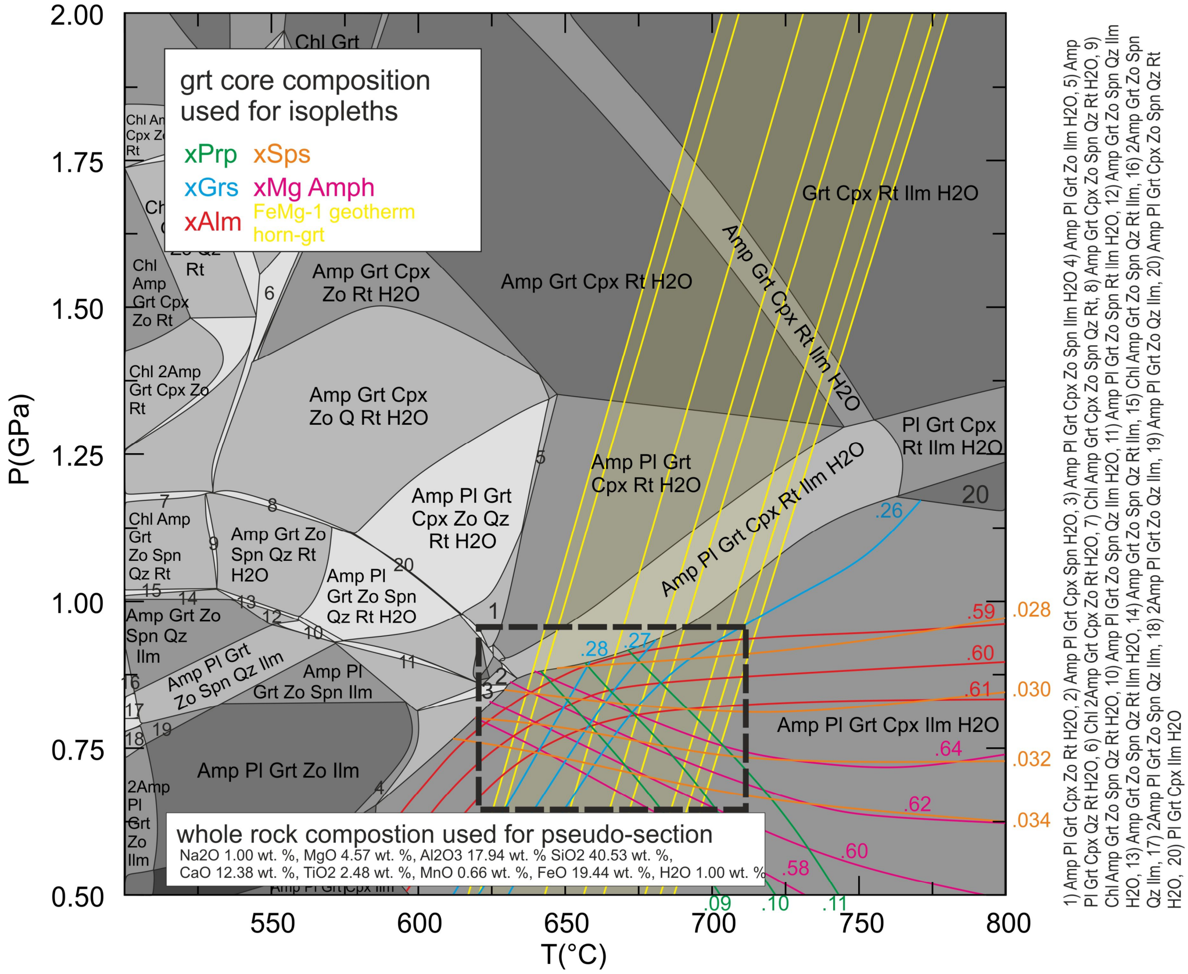

Fig. 50 Calculated pseudosection of bulk-rock composition representing initial garnet growth of sample X37. Isopleths intercept inside the dashed rectangle in the field of Amp, Pl, Grt, Cpx, Ilm and H_2O. Used bulk rock composition is found at the bottom of the diagram.

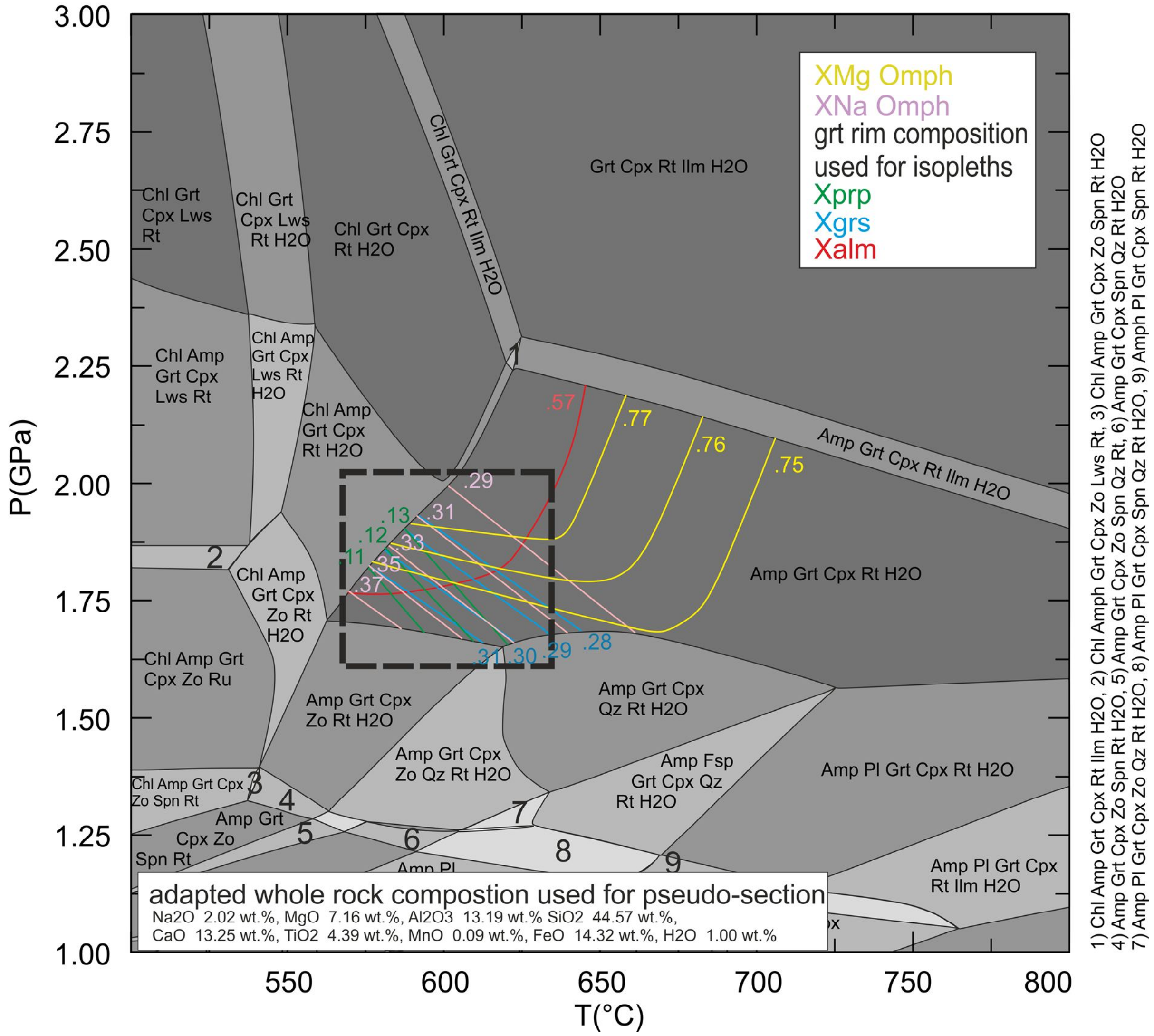

Fig. 51 Calculated pseudosection of recalculated bulk-rock composition representing garnet rim growth of sample X35. Isopleths intercept inside the dashed rectangle in the field of Amp, Grt, Cpx, Rt and H_2O. Used bulk rock composition is found at the bottom of the diagram.

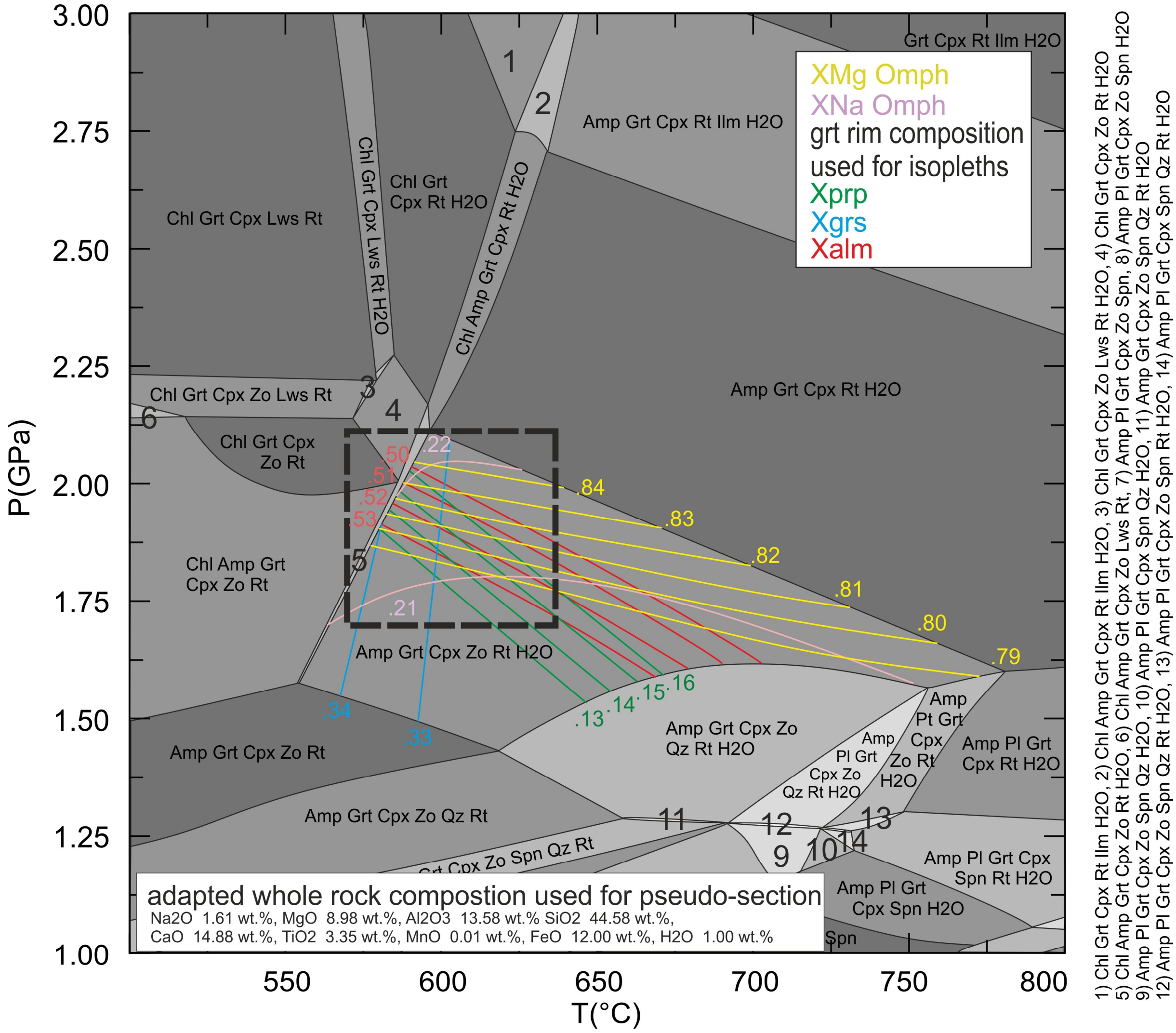

Fig. 52 Calculated pseudosection of recalculated bulk-rock composition representing garnet rim growth of sample X36. Isopleths intercept inside the dashed rectangle in the field of Amp, Grt, Cpx, Zo, Rt and H_2O. Used bulk rock composition is found at the bottom of the diagram.

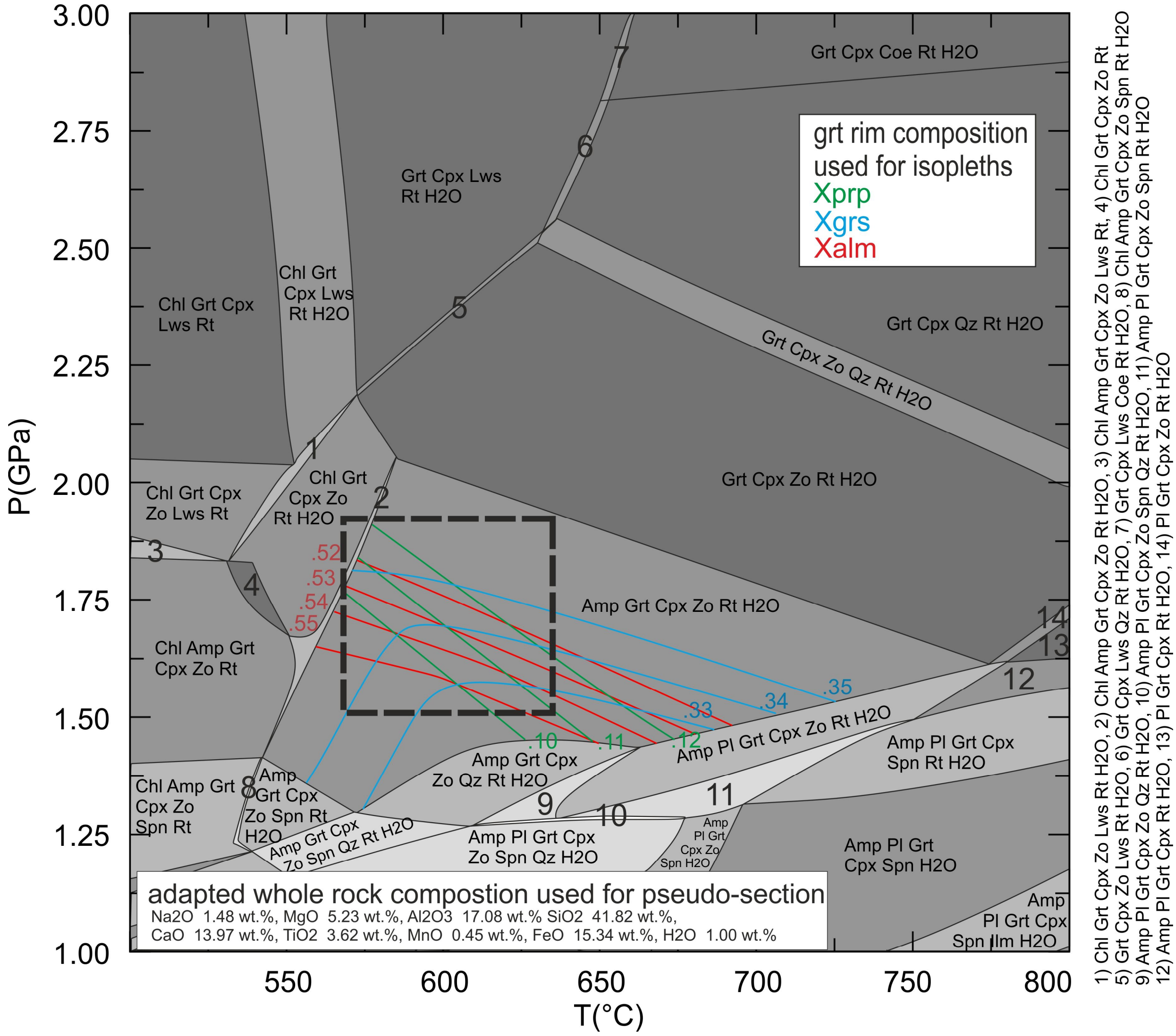

Fig. 53 Calculated pseudosection of recalculated bulk-rock composition representing garnet rim growth of sample X37. Isopleths intercept inside the dashed rectangle in the field of Amp, Grt, Cpx, Zo, Rt and H_2O. Used bulk rock composition is found at the bottom of the diagram.

11 Discussion and Interpretation

The metabasic unit of the Songshugou ophiolite can be divided into garnet amphibolites and amphibolites. Based upon their trace elements, and REE patterns, amphibolites are interpreted as oceanic tholeiitic basalts with T-MORB and E-MORB character. Amphibolites contain SiO_2 ranging from 45 wt.% to 49 wt.%, whereas Grt-amphibolites contain less SiO_2 varying from 38 wt.% to 42 wt.%. Amphibolites show typical trends of tholeiitic differentiation. Garnet amphibolites show different trends, probably related to amphibole fractionation (positive correlation between MgO and Na_2O, K_2O, Rb, and Sr; Rb, K, Sr troughs in chondrite normalized spider plots). Garnet amphiobolites are highly enriched in LREEs similar to trends observed in EMORB and OIB but with higher overall REE abundance; and are enriched in HFSE e.g. (TiO_2, P_2O_5). Amphibolites are far less enriched in REEs and hardly show overall REE fractionation. The REE enrichment patterns of garnet amphibolites point at a different mantle source compared to amphibolites; crustal contamination seems unlikely since no Nb and Ta troughs were observed. Grt amphibolites represent either unusual SiO_2 – poor FeO and TiO_2-rich E-MORB melts, or probably evolved dikes of alkaline affinity. Grt amphibolite showed textural evidence of decompression and retrogression; in terms of various symplectites formed after omphacite, and reaction bands between Grt and Cpx. The reaction bands can be divided into 4 zones: 1=Grt, 2=Pl-Amp corona, 3=Amp, 4=Cpx symplectite. In analyzed samples, strong spatial organization and chemical zoning of minerals was observed, occurring in the reaction zones; with continuous edenite exchange of Amp towards Grt in zones 2 and 3, and continuous increase in X_{An} component of Pl towards Grt in zone2. This is typical for diffusion-controlled reactions. The phenomenon of Cl-rich amphibole rarely forming thin layers along the boundary of Pl-coronae (zone2) and matrix-amphibole (zone3), or crosscutting matrix assemblege as norrow veinletts, suggests that Cl rich fluids were at least partly involved in reaction-band formation. Reintegration of Cpx-Amp-Pl symplectites resulted in former omphacitic compositions similar to those acquired in Cpx grains that are almost free of intergrowths.

Garnet zoning

Garnet grains show a pronounced chemical zoning pattern with three distinctive compositional zones (core, rim1, & rim2). In some cases, rim2 was entirely consumed due to retrogression. Since the chemical composition of Grt is very susceptible to PT changes, the observed chemically homogenous Grt cores indicate that Grt core growth occurred within a small PT window or was homogenized through diffusion at high temperatures. The most conspicuous feature is the abrupt increase of X_{Grs} between core and rim1, and the drop of X_{Grs} between rim1 and rim2 ; and is ubiquitous in all garnets. X_{Alm} usually shows inverse zoning. Garnet poikioblasts are typically inclusion rich. Inclusions of Amp + albitic Pl + Ilm + Ap + Zrn ± Czo/Ep ± Qtz are commonly enclosed in garnet cores and Amp + Rt + Ap ± Zrn ± Czo/Ep in garnet rim1. Trace element patterns show an abrupt increase in V, Ni and Cr at the core - rim1 boundary. Ilmenite usually contains significant amounts of Cr, Ni, Sc, and V. Thus, the observed increase in V, Ni and Cr in garnet rim1 indicates a breakdown of ilmenite to garnet and rutile. Chondrite normalized REE patterns of Grt core and rim (1+2) clearly diverge. Garnet cores show strong HREE enrichment. Grt rim(1+2) measurements are slightly enriched in the lighter HREEs. A general rimward decrease in heavy HREE is observed, which is symptomatic for HREE depletion in the matrix during garnet growth in a closed system. Neodymium, Sm, Tb, Dy and Ho show similar zoning trends with low abundances in the core and an abrupt increase at rim1, which can be attributed to the breakdown of Amp which has high partition coefficients for these elements. Breakdown of Amp could also contribute to the observed enrichement in Cr and V at garnet rim1. Fig. 54 displays a calculated pseudosection of sample X37 with Amp modes plotted as orange lines. Modal Amp content decreases towards higher PT conditions. Therefore, we conclude that an Amp breakdown during Grt rim growth at high PT conditions contributed to the observed chondrite normalized REE patterns of the Grt rims.

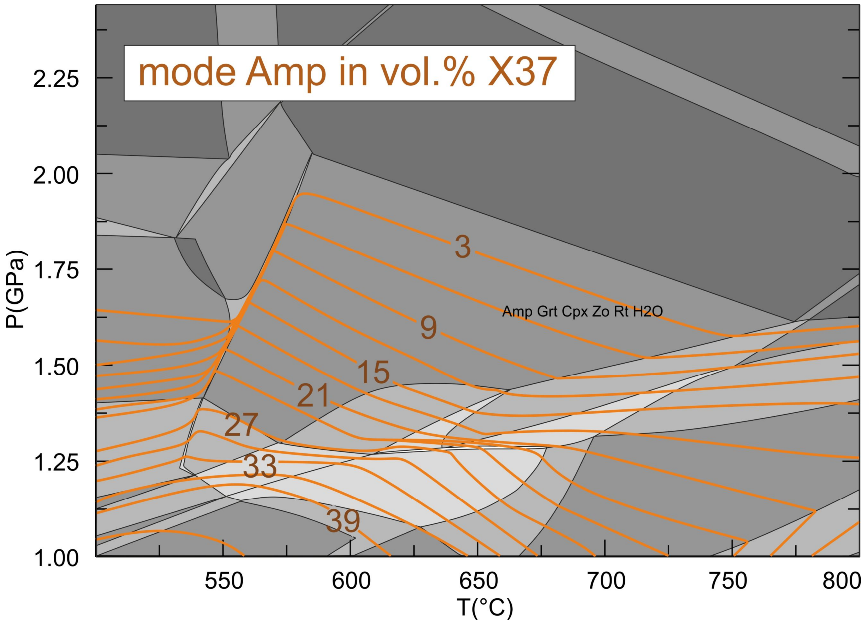

Fig. 54 Pseudosection calculated for sample X37. Orange lines represent Amp mode in vol.%.

Chemical zoning patterns in garnets (REEs and majors) and different mineral assemblages associated with core and rim compositions indicate a poly-phase metamorphic history. We propose that the Grt rim1 with its high X_{Grs} content relates to HP conditions during garnet rim growth. Rim2 must have grown subsequent to the HP event at lower PT conditions prior to garnet consumption.

Estimation of metamorphic P-T conditions

P-T conditions were estimated by means of pseudosection modeling substantiated by conventional geothermobarometry. Based on petrography, major element and REE distribution patterns of garnet, a polymetamorphic history can be concluded.

(1) First metamorphic event is represented by garnet cores, which typically contain inclusions of amphibole, plagioclase, and ilmenite ± quartz ± clinozoisite. Observed snowball textures in the cores indicate syndeformative garnet growth. PT estimations of this metamorphic event has been specified by intersection of garnet core isopleths (X_{Grs}, X_{Alm}, X_{Prp}) and X_{Mg} isopleths of amphibole in calculated bulk-rock pseudosections. Along with garnet-hornblende geothermometry of amphibole inclusions in garnet core, an amphibolite to lower granulite facies event can be concluded with 0.7 – 1.0 GPa and 630 – 730 °C with a stable mineral assemblage of amphibole, plagioclase, garnet, clinopyroxene and ilmenite. The first metamorphic event is solely represented by the garnet cores with mineral inclusions. Garnet cores do not exhibit any pronounced zonation. Thus, with the lack of further PT information no PTt-path can be constructed for the first metamorphic event. PT conditions of initial garnet cores representing a pre eclogites metamorphic event are displayed in Fig. 55.

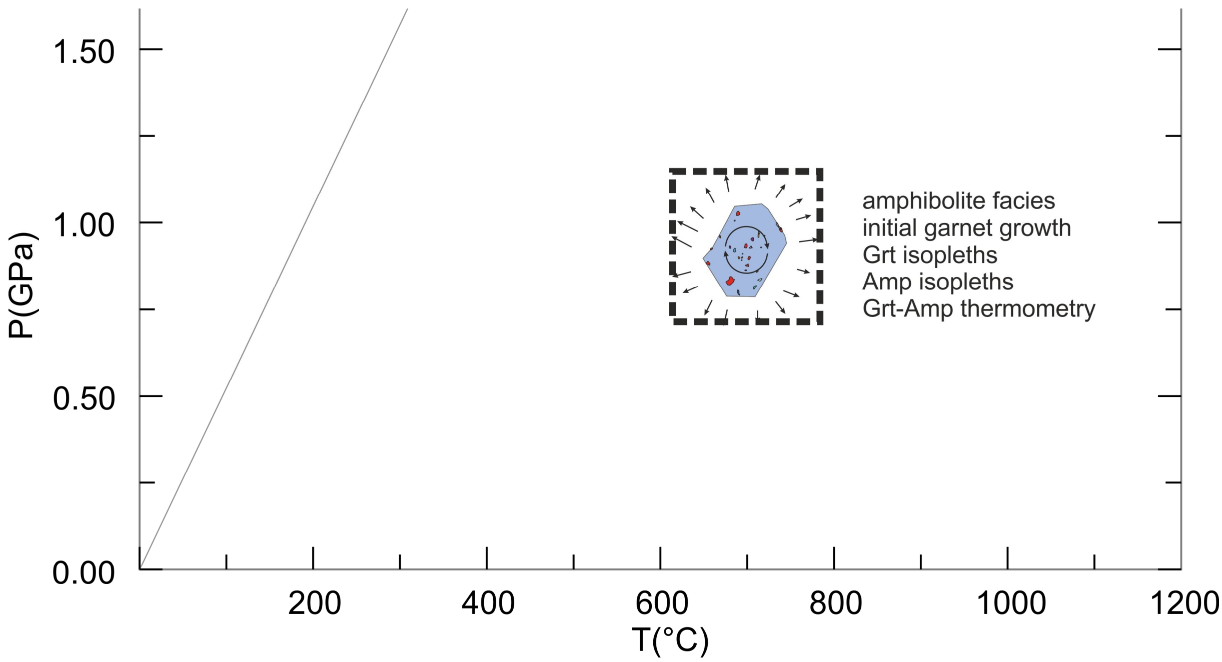

Fig. 55 PT diagram displaying first metamorphic event represented solely by garnet core. Isopleth geothermobarometry of garnet endmembers and X_{Mg} in amphibole and amphibole-garnet geothermometry yield a PT window of 0.7-1.0GPa and 630-730°C.

(2) A second metamorphic event of eclogitic conditions is represented by garnet rim and omphacitic clinopyroxene. To constrain PT conditions, pseudosections for garnet-rim growth were chemically adjusted in consideration of elements being locked into cores. Garnet rim isopleths (X_{Grs}, X_{Alm}, X_{Prp}) and omphacite isopleths (X_{Mg}, X_{Na}) intersect at 1.7 – 2.1 GPa and 570 – 650 °C, representing typical PT conditions of a eclogites facies metamorphic peak. That is substantiated by Cpx-Grt FeMg-1 geothermobarometry (Krogh, 2000) of garnet rim and omphacitic clinopyroxene found in matrix, yielding temperatures of 500 to 650°C.

Subsequent exhumation and hydration contributed to symplectitic clinopyroxene, amphibole growth, reaction bands between clinopyroxene and garnet, and consumption of garnet. A late retrograde stage is described by the formation of low grade minerals such as prehnite and pumpellyite. To evaluate PT conditions of retrogression, thermobarometric calculations and multi equilibrium geothermobarometry were used. For microtextural domains in the garnet coronae, consisting of plagioclase, amphibole and garnet, local equilibrium is assumed. Therefore strong to hardly developed garnet coronae have been analyzed to constrain PT conditions of the retrograde path by applying the Grt-Amp FeMg- thermometer and the Grt-Amp-Pl barometer (Prg-Tr reaction) after Dale et al., 2000, reaction 1-2.

1.) 3Fact + 5Prp = 3Tr + 5Alm — Dale et al., 2000
2.) 3Prg + 4Grs + 2Prp + 12Qz = 3Tr + 12An — Dale et al., 2000

Narrow coronas, of less retrogressed samples yield temperatures from 670 to 800°C and pressures from 0.8 to 1.3 GPa, representing an early retrograde stage. Coronae of stronger retrogressed grains yield lower conditions of 450-650°C and 0.4 – 0.6 GPa (**Fig. 56**). Further reactions that could contribute to the observed reaction bands between Cpx and Grt were calculated with winTWQ (Berman, 1991). Activities of mineral endmembers were determined by the activity-composition calculation program winCMP using nonideal activity models for garnet (Berman, 1990), amphibole (Mader et al., 1994) and plagioclase (Fuhrman and Lindsley, 1988).

Calculated reactions 3-10 are listed below and point at temperatures from 600 to 800°C.

3.) 12Ts + 6Prg = 19Prp + 6Jd + 11Grs + 3Di +18H_2O	TWQ 1.02
4.) 3Prg + 9Ts = 8Grs + 3Jd + 13Prp + 3Qz + 12H_2O	TWQ 1.02
5.) 5Qz + Tr + 3Prg = 3Prp + 3Jd +8Di + 4H_2O	TWQ 1.02
6.) 5An + 9Tr + 7Prg = 12Prp + 7Jd + 37Di + 16H_2O	TWQ 1.02
7.) 21Ts + 3Tr = 16Grs + 26Prp + 24Qz + 24H_2O	TWQ 1.02
8.) 8Prg + 5Ts + 11Tr = 48Di + 8 Jd + 18Prp + 24H_2O	TWQ 1.02
9.) 12Qz + 6Prg = 5Prp + 6Jd + Grs + 9Di + 6H_2O	TWQ 1.02
10.) 3An + 3Ts + 3Prg = 7Prp + 3Jd + 5Grs + 6H_2O	TWQ 1.02

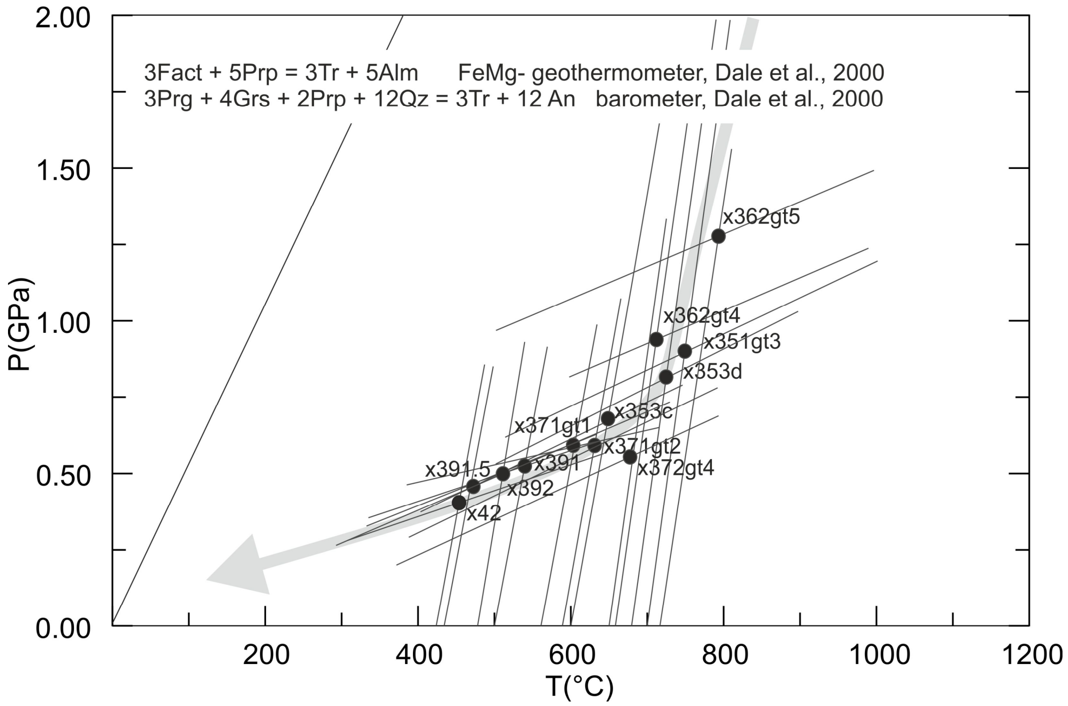

Fig. 56 P-T estimates of Pl-Amp coronae around Grt by using the Grt-Amp FeMg- thermometer and the Grt-Amp-Pl barometer (Prg-Tr reaction) after Dale et al., 2000. Each point represents the average value of multiple microprobe analyses taken at one micro domain.

PT estimates of retrograde Cpx-Pl-Amp symplectite assemblages range from 570 to 700°C and 0.5 to 0.7GPa (reactions 10-12).

10.) Ed + Ab = Ri + An	Hbl-Pl thermometer	Holland and Blundy, 1994
11.) Tr + 4Jd + Cats = 3Ab + Di + Prg		TWQ 1.02
12.) 2Cats + Di + Jd + Ts = Prg + 3An		TWQ 1.02

Lowest conditions at late stage retrogression are presented by the formation of prehnite. Activities of mineral endmembers have been determined by the AXWin, i.e. (Tr=0.14, Ts=0.002, Prg=0.003, An=0.45, Di=0.61, Grs=0.03, Cats=0.21). Possible reactions leading to Prh in Grt corona (reaction 13) and Prh in Cpx-Pl-Amp-Prn (reactions 14-17) symplectite are listed below and point to temperatures between 200 – 350 °C for late stage retrogression.

13.) 2Prn = 1Grs + 1Qz + 1An + 2 H_2O PerpleX
14.) 1Ts + 6Prh + 1Tr = 8An + 8Di + $8H_2O$ PerpleX
15.) 1Ts + 3Prh + 1Qz = 5An + 3Di + $4H_2O$ PerpleX
16.) 3Prh + 1Tr = 3An + 5 Di + 1Q + $4H_2O$ PerpleX
17.) 1Ts + 3Prh = 1Cats + 4An + 3Di + $4H_2O$ PerpleX

Results plotted in Fig. 57 suggest a clockwise P-T path for the second metamorphic event with eclogite facies conditions in field1. A short residence time at field2 was responsible for garnet rim2 growth, followed by early stage retrogression recorded by upper amphibolite facies decompression reactions in field3 (garnet breakdown, cpx-symplectite development) and late stage retrogression at low PT conditions in field4 (prehnite, pumpellyite formation).

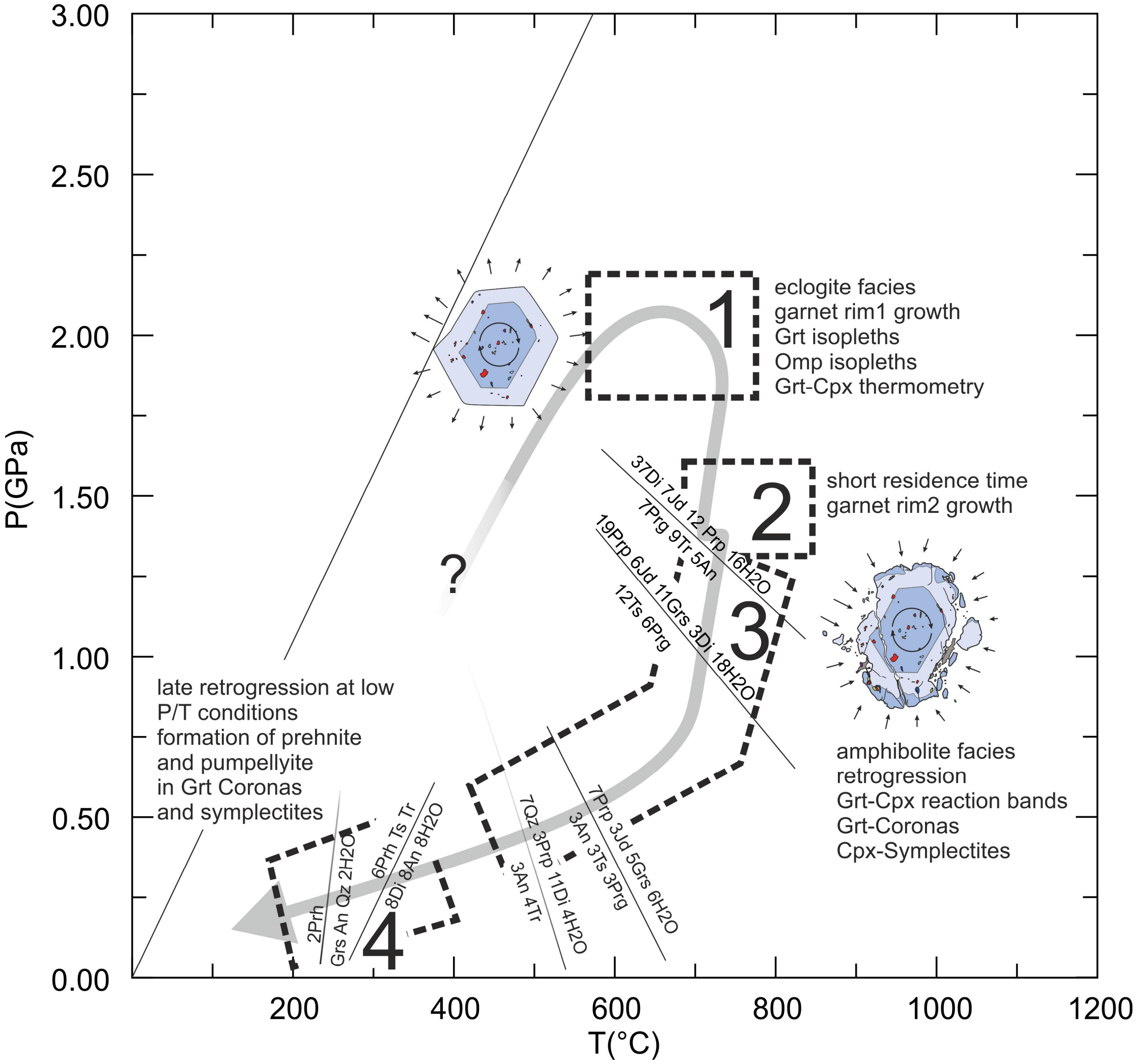

Fig. 57 PT estimates of Songshugou Grt-amphibolites for the second metamorphic event represented by garnet rim and matrix. **Field 1:** PT estimates from Grt core and Cpx isopleths geothermobarometry and Cpx-Grt geothermometry representing minimum peak conditions. **Field 2:** Short residence time in mid-crustal levels, growth of rim2. **Field 3:** retrograde stage, PT conditions estimated from Cpx-Pl-Amp symplectites, Grt-Cpx reaction bands and Grt-coronae (reactions 1-12). **Field 4:** late retrograde stage, PT conditions derived from Prn formation in Grt-coronae and symplectites.

(2) Tectonic framework.

“The Songshugou ophiolite represents a fragment of oceanic lithosphere that once separated the North Qinling and South Qinling terranes” (Dong et al., 2008). Obtained Sm-Nd whole rock ages of 1030 - 983 Ma represent the age of the basaltic oceanic crust protolith (Li et al., 1991; Liu et al., 2004, Dong et al,. 2008), similar to the Sm-Nd age of the Heihe ophiolite (963±10Ma, Zhang et al., 2000) which outcrops in the western part of the Shangdan suture zone.

An amphibolite/lower granulite facies event is recorded in garnet cores, which may have taken place during Early Paleozoic. The modelled clockwise PT path for rim1 growth in this study is probably related to subduction at a collision regime, maybe the northward subduction of the Shangdan oceanic crust (Li Tang et al., 2016). Zircons of ophiolites along the Shangdan suture zone have been dated and yielded ages of 534-440 Ma for the northward subduction of the Shangdan oceanic crust. (Lu et al., 2003; Yang et al., 2006; Liu et al., 2007; Pei et al., 2007; Li 2008; Dong et al., 2011b). In North Qinling, HP to UHP metamorphism is widely observed at around 500 Ma. (Yang et al., 2003; Wang et al., 2011, Liu et al., 2013; Wang et al., 2014). Zircon, included in Grt amphibolites of the Songshuou metabasic unit, reveals similar ages of 485 – 510 Ma (Chen et al., 2004; Liu et al., 2009; Qian et al., 2013; Li et al., 2014b, Li Tang et al., 2016). Peak conditions of Songshugou Grt amphibolites (>18kbar, 550-650°C) represented by garnet rims and omphacitic clinopyroxene, probably belong to this subduction event. Subsequent post-peak decompression and retrogression contributing to retrograde textures such as symplectites after omphacite and coronae around garnet are commonly observed in eclogites (Eskola, 1921; Griffin and Raheim, 1973; Wilkerson et al., 1988; O’Brien et al., 1990; Droop et al., 1990; Zhao et al., 2001). A short residence time at midcrustal levels probably lead to formation of rim2, which was consumed partly together with rim1 by retrograde reactions Those characteristic retrograde textures together with the PT path point at decompression and later cooling possibly related to two stages of lifting in North Qinling at around 450Ma and 420Ma (Liu et al., 2013; Li Tang et al., 2016).

12 References

Ames et al., 1996 ; Ames, L., Zhou, G., Xiong, B., 1996. Geochronology and geochemistry of ultrahighpressure metamorphism with implications for collision of the Sino-Korean and Yangtze cratons, Central China. Tectonics 15, 422–489.

An et al., 1985 ; An, S.Y., Wang, D.R., Shu, Q.Q. 1985 Reconstruction of the protoliths and polyphase metamorphism of the amphibolite series of the Qinling terrain in Shangnan, Shaanxi. Regional Geology of China 13, 159-70

Carlson and Johnson, 1991 ; William D.Carson, Cambria D. Johnson, 1991, Coronal reaction textures in garnet amphibolites of the Llano Uplift. American Mineralogist, Volume 76 pages 756-772

Chakraborty and Ganguly, 1991 ; Chakraborty, S. and Ganguly, J. C. (1991). Compositioinal zoning and cation diffusion in garnets. Advances in Physical Geochemistry 8 120-175.

Chakraborty and Ganguly, 1992 ; Chakraborty, S. and Ganguly, J. (1992). Cation diffusion in aluminosilicate garnets; experimental determination in spessartine-almandine diffusion couples, evaluation of effective binary, diffusion coefficients, and applications. Contributions to Mineralogy and Petrology. 111 (1): 74-86.

Chen et al., 1993 ; Chen, N.S., Yang, Y., Zhou, H.W., 1993. High pressure metamorphism of garnet amphibole rocks from Songshugou area, eastern Qinling mountain and its tectonic implication. Journal of China University of Geosciences 14, 36–45 (in Chinese with Englishabstract).

Chen et al., 2004 ; Chen, D.L., Liu, L., Sun, Y., Zhang, A.D., Liu, X.M., Luo, J.H., 2004. LA-ICP-MS zircon U-PB dating for high-pressure basic granulite from North Qinling and ist geological significance. Chinese Science Bulletin 49, 2296-2304.

Chopin, 1984 ; Chopin, C., 1984. Coesite and pure pyrope in high-grade blueschists of the Western Alps: first record and some consequences. Contrib. Mineral. Petrol. 86, 107–118.

Connolly, 2005 ; Connolly JAD (2005) Computation of phase equilibria by linear programming: A tool for geodynamic modeling and ist application to subduction zone decarbonation: Earth and Planetary Science Letters 236:524-541

Czamanske et al., 1981 ; Czamanske G. K , Ishihara,S .,and Atkin, S.A.(1981)C hemistry of rock forming minerals of the Cretaceous-Paleogenbatholith in southwestern Japan and implications for magma genesis. Journal of Geophysical Research8.6 . 10431-10469

Dachs, 1998 ; Dachs Edgar (1998) PET: Petrological elementary tools for Mathematica. Computers & Geoscience 24/3:219-235

Dale et al., 2000 ; Jonathon Dale, Tim Holland, Roger Powell 2000, Hornblende-garnet-plagioclase thermobarometry: a natural assemblage calibration of the thermodynamics of hornblende Contrib Mineral Petrol 2000, 140:353-362

Diwu et al., 2010 ; Diwu, C.R., Sun, Y., Liu, L., Zhang, C.L., Wang, H.L., 2010. The disintegration of Kuanping Group in North Qinling orogenic belts and Neo-proterozoic N-MORB. Acta Petrologica Sinica 26, 2025–2038 (in Chinese with English abstract).

Diwu et al., 2012 ; Diwu, C.R., Sun, Y., Zhang, H., Wang, Q., Guo, A.L., Fan, L.G., 2012. Episodic tectonothermal events of the western North China Craton and North Qinling Orogenic Belt in central China: constraints from detrital zircon U–Pb ages. Journal of Asian Earth Sciences 47, 107–122.

Dong and Santosh, 2016 ; Dong, Y., Santosh, M., 2016. Tectonic architecture and multiple orogeny of the Qinling Orogenic Belt, Central China. Gondwana Research 29, 1-40

Dong et al., 1996 ; Dong, Y.P., Zhou, D.W., Liu, L., 1996. Dislocation microstructures of olivine from Songshugou ophiolite and their rheological implications. Acta Petrologica et Mineralogica 15, 46-53

Dong et al., 1999 ; Dong, Y.P., Zhang, G.W., Lai, S.C., Zhou, D.W., Zhu, B.Q., 1999, An ophiolitic tectonic melange first discovered in Huashan area, shouth margin of qinling orogenic belt and ist tectonic implications. Science in China (Series D) 42, 292-301

Dong et al., 2008 ; Dong, Y.P., Zhou, M.F., Zhang, G.W., Zhou, D.W., Liu, L, Zhang, Q., 2008. The Grenvillian Songshugou ophiolite in the Qinling Mountains, Central China: implications for the tectonic evolution of the Qinling orogenic belt. Journal of Asian Earth Sciences 32, 325-335

Dong et al., 2011a ; Dong, Y.P., Genser, J., Neubauer, F., Zhang, G.W., Liu, X.M., Yang, Z., Heberer, B., 2011a. U-Pb and 40Ar/39Ar geochronological constraints on the exhumation history of the North Qinling terrane, China. Gondwana Research 19, 881-893.

Dong et al., 2011b ; Dong, Y.P., Zhang, G.W., Hauzenberger, C., Neubauer, F., Yang, Z., Liu, X.M., 2011b. Palaeooic tectonics and evolutionary history of the Qinling orogen: evidence from geochemistry and geochronology of ophiolite and related volcanic rocks. Lithos 122, 39-56

Dong et al., 2011c ; Dong, Y.P., Zhang, G.W., Neubauer, F., Liu, X.M., Genser, J., Hauzenberger, C., 2011c. Tectonic evolution of the Qinling orogen, China: review and synthesis. Journal of Asian Earth Sciences 41, 213-237.

Dong et al., 2013 ; Dong, Y.P., Liu, X.M., Neubauer, F., Zhang, G.W., Tao, N., Zhang, Y.G., Zhang, X.N., Li, W., 2013. Timing of Paleozoic amalgamation between the North China and South China Blocks: evidence from detrital zircon U–Pb ages. Tectonophysics 586, 173–191.

Dong et al., 2014 ; Dong, Y.P., Yang, Z., Liu, X.M., Zhang, X.N., He, D.F., Li,W., Zhang, F.F., Sun, S.S., Zhang, H.F., Zhang, G.W., 2014. Neoproterozoic amalgamation of the Northern inling terrain to the North China Craton: constraints from geochemistry of the Kuanping ophiolite. Precambrian Research 255, 77–95.

Droop et al., 1990 ; Droop GTR, Lombardo B, Pognante U (1990) Formation and distribution of eclogite facies rocks in the Alps. In: Carswell DA (ed) Eclogite facies rocks. Chapman and Hall, New York, pp 225–259

Dupre and Allegre, 1983 ; Dupre, B., Allegre, C.J., 1983. Pb–Sr isotopic variation in Indian Ocean basalts and mixing phenomena. Nature 303, 142–146.

Enami et al., 1993 ; Enami, M., Liou, J.G and Bird, D.K. (1993) Cl amphibole in the salton Sea geothermal system, California, Canadian Mineralogist, 30, in press.

Enkin et al., 1992 ; Enkin, R.J., Yang, Z., Chen, Y., Courtillot, V., 1992. Paleomagnetic constraints on the geodynamic history of the major blocks of China fromPermian to the present. Journal of Geophysical Research 97, 13953–13989.

Eskola, 1921 ; On the eclogites of Norway. Videnskapsselskapets Skrifter, I Mat Naturv Klasse 8:1–118

Evans 2004 ; Evans, T.P. 2004. A method for calculating effective bulk composition modification due to crystal fractionation in garnet-bearing schist: implications for isopleth thermobarometry. J. metamorphic Geol., 2004, 22, 547-557

Fisher, 1977 ; Fisher, G.W. (1977) Nonequilibrium thermodynamics in metamorphism. Thermodynamics in geology, p. 381-403. Reidel, Boston

Frey and Green, 1974 ; Frey. F.A., Green, D.H., 1974. The miuneralogy, geochemistry and origin of lherzolite inclusions in Victorian basanites. Geochim. Cosmochim. Acta 38 1023-59

Gaidies et al., 2011 ; Gaidies, F., Pattison, D.R.M., de Capitani, C., 2011, Toward a quantitative model of metamorphic nucleation and growth: Contributions to Mineralogy and Petrology, v. 162, no.5 p. 975-993

Gao et al., 1995 ; Gao, S., Zhang, B.R., Gu, X.M., Xie, X.L., Gao, C.L., 1995. Silurian–Devonian provenance changes of South Qinling basins: implications for accretion of the Yangtze (South China) to the North China Cratons. Tectonophysics 250, 183–197.

Grifin and Raheim, 1973 ; Griffin WL, Ra°heim A (1973) Convergent metamorphism of eclogites and dolerites, Kristiansund area, Norway. Lithos 6:21–40

Hacker et al., 1998 ; Hacker, B.R., Ratschbacher, L., Webb, L., Ireland, T., Walker, D., Dong, S., 1998. U/Pb zircon ages constrain the architecture of the ultrahigh-pressure Qinling-Dabie Orogen, China. Earth and Planetary Science Letters 161, 215–230.

Hamelin et al., 1986 ; Hamelin, B., Dupre, B., Allegre, C.J., 1986. Pb–Sr–Nd isotopic data of Indian Ocean ridge: new evidence of large-scale mapping of mantle heterogeneities. Earth and Planetary Science Letters 76, 288–298.

Heinrich 1982 ; Heinrich C.A. 1982. Kyanite-eclogite to amphiibolite facies evolution of hydrous mafic and pelitic rocks, Adula Nappe, Central Alps, Contrib Mineral Petrol 81:30-38

Holland and Powell, 1998 ; Holland TJB, Powell R (1998 revised by authors in 2004) An internally consistent thermodynamic data set for phases of petrological interest. Journal of Metamorphic Geology 16: 309–343

Holland and Powell, 1999 ; Holland TJB, Powell R (1999) Relating formulations of the thermodynamics of mineral solid solutions: Activity modeling of pyroxenes, amphiboles, and micas. American Mineralogist 84: 1–14

Holland and Powell, 2001 ; Holland TJB, Powell R (2001) Calculation of phase relations involving haplogranitic melts using an internally consistent thermodynamic solid solutions: American Mineralogist 81: 1425–1437

Huang 1984 ; Huang, Y.H., 1984. The contact metamorphic belt of the Alps-type ultramafic body from Songshugou area. Geochemica 13, 206–215 (in Chinese with English abstract).

Janoušek et al., 2006 ; Janoušek V, Farrow CM, Erban V (2006) Interpretation of whole-rock geochemical data in Journal of igneous geochemistry: introducing Geochemical Data Toolkit (GCDkit). Petrology 47: 1255–1259

Jensen 1976 ; Jensen, L.S. 1976. A new cation plot for classifying subalkalic volcanic rocks. Ontario Geological survey miscellaneous paper 66

Kallerud 1996 ; Chlorine-rich amphiboles: interplay between amphibole composition and an evolving fluid. European Journal of Mineralogy, 8 355-370

Krogh, 2000 ; Krogh Ravana, E.J. (2000) The garnet-clinopyroxene Fe2+-Mg geothermometer: an updated calibration. J. Metamorph. Geol., 18:211-219

Kröner et al., 1993 ; Kröner, A., Zhang, G.W., Sun, Y., 1993. Granulites in the Tongbai Area, Qinling Belt, China: geochemistry, petrology, single zircon geochronology, and implications for the tectonic evolution of eastern Asia. Tectonics 12, 245–255.

Kullerud 1995 ; Kullerud K., 1995. Chlorine, titanium and barium-rich biotites: factors controlling biotite composition and implications for garnet-biotite geothermometry. Contributions to Mineralogy and Petrology, 120, 42-59

Le Bas and Maitre 1986 ; Le Bas, M. J., Le Maitre, R. W., Streckeisen A & Zanettin, B. 1986. A chemical classification of volcanic rocks based on the total alkali-silica diagram. Journal of Petrology 27, 745-750

Leake 1964 ; Bernard E.Leake 1964. The chemical distinction between ortho- and para-amphibolites. Journal of Petrology Vol 5 pp 238-254

Leake et al. 1997 ; Leake, B.E., Woolley, A.R., Arps, C.E.S., Birch, W.D., Gilbert, M.C., Grice, J.D., Hawthorne, F.C., Kato, A., Kisch, H.J., Krivovichev, V.G., Linthout, K., Laird, J., Mandarino, J.A., Maresch, W.V., Nickel, E.H., Rock, N.M.S., Schumacher, J.C., Smith, D.C., Stephenson, N.C.N., Ungaretti, L., Whittaker, E.J.W., and Youzhi, G. (1997) Nomenclature of amphiboles: Report of the Subcommittee on Amphiboles of the International Mineralogical Association, Commission on New Minerals and Mineral Names. American Mineralogist, 82, 1019–1037

Leake, 1978 ; Leake. B.E. (1978) Nomenclature of amphiboles. Mineralogical Magazine. 42.533-563.

Lexa, 2011 ; Ondrej Lexa. Program to make contour plot from contour data file generated by Perplex X. http://petrol.natur.cuni.cz/~ondro/pywerami:home.

Li et al., 1991 ; Li, S.G., Chen, Y.Z., Zhang G.W. Zhang, Z.Q. 1991, A 1 Ga B.P. Alpine peridotite body emplaced into the Qinling Group: evidence for the existence of the late Proterozoic plate tectonics in the North Qinling area. Geological Review 37, 235-242

Li et al., 1993a ; Li, S.G., Xiao, Y.L., Liu, D.Y., Chen, Y.Z., Ge, N.J., Zhang, Z.Q., Sun, S.S., Cong, B.L., Zhang, R.Y., Hart, S.R.,Wang, S.S., 1993a. Collision of the North China and Yangtze blocks and formation of coesite-bearing eclogites: timing and processes. Chemical Geology 109, 89–111.

Li et al., 1996 ; Li, S.G., Jagoutz, E., Xiao, Y.L., Ge, N.J., Chen, Y.Z., 1996. Chronolgy of ultrahigh-pressure metamorphism in the Dabie Mountains and Su-lu terrane. Sm-Nd isotope system. Science in China (Series D: Earth Schience) 39

Li et al., 2006a ; Li, H.M., Chen, Z.H., Xiang, Z.Q., Li, H.K., Lu, S.N., Zhou, H.Y., Song, B., 2006a. Difference in U–Pb Isotope ages between baddeleyite and zircon in metagabbro from the Fushui complex in the Shangnan-Xixia area, Qinling orogen. Geological Bulletin of China 25, 653–659.

Li et al., 2014 ; Li, Y., Zhou, H.W., Li, Q.L, Xiang, H., Zhong, Z.Q. Brouwer, F.M., 2014b. Palaeozoic polymetamorphism in the North Qinling orogenic belt, Central China: insights from petrology and in situ titanite and zircon U-Pb geochronology. Journal of Asian Earth Sciences 92, 77-91

Li Tang et al., 2016 ; Li Tang, M. Santosh, Yunpeng Dong, Toshiaki Tsunogae, Shouting Zhang, Huawen Cao (2016) Early Paleooic tectonic evolution of the North Qinling orogenic belt: Evidence from geochemistry, phase equilibrium modeling and geochronology of metamorphosed mafic rocks from the Songshugou ophiolite, Gondwana Research 30 (2016) 48-64

Li, 1994 ; Li, Z.X., 1994. Collision between the North and South China blocks: a crustaldetachment model for suturing in the region east of the Tanlu fault. Geology 22, 739–742.

Li, 2008 ; Li, W.Y., 2008. Geochronology and Geochemistry of the Ophiolites and Island-arctype Igneous Rocks in the Western Qinling Orogen and the Eastern Kunlun Orogen: Implication for the Evolution of the Tethyan Ocean. University of Science and Technology of China, Hefei, pp. 1-154

Liu and Zhou, 1994 ; Liu, L., Zhou, D.W., 1994. Discovery of high-pressure basic granulites from the Songshugou area, Shannan, eastern Qinling Mountains, Chinese Science Bulletin 39, 1599-601

Liu et al., 1993 ; Liu, G.H., Zhang, S.G., You, Z.D., 1993. Metamorphic Rocks in Qinling Orogen Belt and Its Metamorphic Evolution. Geology Press, pp. 68–89 (in Chinese).

Liu et al., 1995 ; Liu, L., Zhou, D.W., Dong Y.P., Zhang, H.F., Liu, Y.J., Zhang, Z.J., 1995. High pressure metabasites and their retrograde metamorphic P-T-t path from Songshugou area, eastern Qinling Mountain, Acta Petrologica Sinica 11, 127-136

Liu et al., 2004 ; Liu, L., Chen, D.L., Zhang, A.D., Zhang, C.L., Yuan, H.L., Luo, J.H., 2004. Geochemical characteristics and La-ICP-MS zircon U-Pb dating of amphibolites in the Songshugou ophiolite in the Eastern Qinling. Acta Geologica Sinica-English Edition 78, 137-145

Liu et al., 2009 ; Liu, J.F., Sun, Y., Tong, L.X., Sun, W.D., 2009. Emplacement age of the Songshugou ultramafic massif in the Qinling orogenic belt, and geologic implications. International Geology Review 51, 58-76

Liu et al., 2013 ; Liu, L., Liao, X.Y., Zhang, C.L., Chen, D.L., Gong, X.K., Kang, L., 2013. Multi-metamorphic timings of Hp-UHP rocks in the North Qinling and their geological implications. Acta Petrologica Sinica 29, 1634-1656

Lu et al., 2003 ; Lu, S.N., Li, H.K., Chen, Z.H.., Hao, G.J., Zhou, H.Y., Guo, J.J., Niu, G.H., Xiang, Z.Q., 2003. Meso-Neoproterozoic Geological Evolution of the Qinling and ist Respondence to Rodinia Event. Geological Publishing House, Beijing, pp. 1-194

Mao et al., 2005 ; Mao, J.W., Xie, G.Q., Zhang, Z.H., Li, X.F., Wang, Y.T., Zhang, C.Q., Li, Y.F., 2005. Mesozoie large-scale metallogenic pulses in North China and corresponding geodynamic settings. Acta Petrologica Sinica 21, 171–190 (in Chinese with English abstract).

Mertz et al., 1991 ; Mertz, D.F., Devey, C.W., Todt, W., 1991. Sr–Nd–Pb isotope evidence against plume asthenosphere mixing north of Iceland. Earth and Planetary Science Letters 107, 243–255.

Meschede 1986 ; Meschede M. 1986. A method of discrimination between different types of mid-ocean ridge basalts and continental tholeiites with the Nb-Zr-Y diagram. Chemical Geology 56, 207-218

Messiga and Bettini, 1990 ; Mesigga, B., Bettini, E., 1990. Reactions behavious during kelyphyte and symplectite deformation: a case study of mafic granulites and eclogites from the Bohemian Massif. Eur J Mineral 2:125-144

Morimoto 1988 ; Morimoto N. 1988. Nomenclature of pyroxenes. Mineralogical Magazine 52, 535-50

Nakamura, 1974 ; Nakamura Noboru (1974) Determination of REE, Ba, Fe, Mg, Na and K in carbonaceous and ordinary chondrites, Geochimica et Cosmochimica Acts, 1974, Vol. 38, pp. 757 to 775

O'Brien et al., 1990 ; O'Brien PJ, Carswell DA, Gebauer D (1990) Eclogite formation and distribution in the European Variscides. In: Carswell DA (ed) Eclogite facies rocks. Chapman and Hall, New York, pp 204– 224

Okay and Sengör, 1993 ; Okay, A.I., Sengör, A.M.C., 1993. Tectonics of an ultra-high pressure metamorphic terrane: the Dabie Shan/Tongbai Shan orogen, China. Tectonics 12, 1320–1334.

Pearce 1975 ; Pearce J. A. 1975, Basalt geochemistry used to investigate past tectonic environments on Cyprus - Tectonophysics 25, 41-67

Pearce and Cann, 1973 ; Pearce, J.A., Cann, J.R., 1973. Tectonic setting of basic volcanic rocks determined using trace element analyses. Earth and Planetary Science Letters 19, 290–300.

Pearce et al., 1975 ; T.H. Pearce, B.E. Gorman, T.C. Birkett 1975, The TiO2-K2O-P2O5 diagram: a method of discriminating between oceanic and non oceanic basalts. Earth and Planetary Science Letters 24, 419-426

Pearce, 1983 ; Pearce, J.A., 1983. Role of sub-continental lithosphere in magma genesis at active continental margins. Continental Basalts and Mantle Xenoliths. Shiva, Nantwich, pp. 230–249.

Pei et al., 2007 ; Pei, X.Z., Ding, S.P., Li, Z.C., Liu, Z.Q., Li, R.B., Wang, F., Li, F.J., 2007. LA-ICP-MS zircon U-Pb dating of the Gabbro from the Guanzizhen ophiolite in the North Margin of the Western Qinling and ist geologic significance. Acta Geologica Sinica 81, 1550-1561

Perchuk et al., 1998 ; Perchuk, A.L., Yapaskurt, V.O., Podlesskii, S.K., 1998. Genesis and exhumation dynamics of eclogites in the Kokchetav massif near mount Sulu- Tjube, Kazakhstan. Geochemistry International (Geokhimiya) 36 (10), 877–885 (979–988).

Pohl 2005 ; Walter L. Pohl. Book petraschecks, lagerstättenlehre, 5te Auflage 2005

Qian et al., 2013 ; Qian, J.H., Yang, X.Q., Liu, L., Cao, Y.T., Chen, D.L., Yang, W.Q., 2013. Zircon U-Pb dating, mineral inclusions, Lu-Hf isotopic data and their geological significance of garnet amphibolite from Songshugou, North Qinling. Acta Petrologica Sinica 29, 3087-3098

Ren et al., 1990 ; Ren, J.S., Chen, T.Y., Niu, B.G., Liu, Z.G., Liu, F.R., 1990. Continental lithospheric tectonic evolution and metallogenism of Eastern China and adjacent rgions. Scientific Press, Bejing.

Schwandt et al., 1996 ; Schwandt, C.S., Cygan, R.T., Westrich, H.R., 1996. Ca self-diffusion in grossular garnet. Am Mineral 81:448-451

Shi et al., 2009 ; Shi, Y., Yu, J.H., Xu, X.S., Qiu, J.S., Chen, L.H., 2009. Geochronology and geochemistry of the Qinling Group in the eastern Qinling Orogen. Acta Petrologica Sinica 25, 2651–2670 (in Chinese with English abstract).

Shu 2012 ; Shu L.S., 2012. An analysis of principal features of tectonic evolution in South China Bock. Geological Bulletin China 31(7): 1035-1053

Skublov and Drugova, 2003 ; Sergey Skublov and Galina Drugova (2003). Patterns of Trace-element distribution in calcic amphiboles as a function of metamorphic grade. The Canadian Mineralogist Vol. 41, pp. 383-392

Spear 1993 ; Spear, F.S. Metamorphic Phase Equilibria and Pressure-Temperature-Time Paths Mineralogical Society of America

Spear and Daniel, 2001 ; F. S. Spear and C. G. Daniel (2001) Diffusion control f garnet growth, Harpswell Neck, Maine, USA J. metamorphic Geol., 2001, 19, 179-195

Spear and Menard, 1989 ; Spear, F. S. and Menard, T. (1989). Program GIBBS; a generalized Gibbs method algorithm. American Mineralogist 74 (7-8): 942-943.

Spear, 1988 ; Spear, F. S., 1988. Metamorphic fractional crystallization and internal metasomatism by diffusional homogenization of zoned garnets. Contributions to Mineralogy and Petrology, 99, 507–517.

Su et al., 2004 ; Su, L., Song, S.G., Song, B., Zhou, D.W., Hao, J.R., 2004. SHRIMP zircon U–Pb ages of garnet pyroxenite and Fushui gabbroic complex in Songshugou region and constraints on tectonic evolution of Qinling Orogenic Belt. Chinese Science Bulletin 49, 1307–1310.

Sun et al., 1996a ; Sun,W.D., Li, S.G., Sun, Y., Zhang, G.W., Zhang, Z.Q., 1996a. Chronology and geochemistry of a lava pillow in the Erlangping Group at Xixia in the northern Qinling Mountains. Gological Review 42, 144–153 (in Chinese with English abstract).

Sun et al., 1996b ; Sun, Y., Lu, X., Han, S., Zhang, G.W., 1996b. Composition and formation of Paleozoic rlangping ophiolitic slab, North Qinling: evidence from geology and geochemistry. cience in China (Series D) 39, 50–59.

Sund and McDonough, 1989 ; Sun, S., McDonough, W.F., Chemical and isotopic systematics of oceanic basalts: implications for mantle composition and processes. Geological Society, London, Special Publications v. 42; p. 313-

345
Thompson and England, 1984 ; Thompson, A. B. & England, P. C., 1984. Pressure–temperature– time paths of regional metamorphism II. Their inference and interpretation using mineral assemblages in metamorphic rocks. Journal of Petrology, 25, 929–955.

Tracy, 1982 ; Tracy, R. J., 1982. Compositional zoning and inclusions in metamorphic minerals. Reviews in Mineralogy, 10, 355–397.

Tseng et al., 2009 ; Tseng, C.Y., Yang, H.Y., Liu, D., Wu, C., Cheng.C.K., Chen, C.H., and Ker, C.M., 1009, Continuity of the North Qilian and North Qinling orogenic belts, Central orogenic system of China: Evidence from newly discovered Paleozoic adakitic rocks: Gondwana REsearch, v 16, p 285-293

Volkova et al., 2014 ; Volkova, N.I., Kovyazin, S.V., Stupakov, S.I., Simonov, V.A., Sakiev, K.S. 2014. Trace Element Distribution in Mineral Inclusions in Zoned Garnets from Eclogites of the Albashi Range (South Tianshan) Geochemistry International, 2014, Vol. 52, No. 11, pp. 939-961

Wang et al., 1995 ; Wang, X.R., Hua, H., Sun, Y., 1995. A study on microfossils of the Erlangping Group in Wantan area, Xixia county, Henan province. Journal of Northwest University 25, 353–358 (in Chinese with English abstract).

Wang et al., 2011 ; Wang, H., Wu, Y.B., Gao, S., Li, Q.L., Li, X.H., Yuan, H.L., 2011. Eclogite origin and timings in the North Qinling terrane, and their bearing on the amalgamation of the South and North China Blocks. Journal of Metamorphic Geology 29, 1019-1031

Wang et al., 2014 ; Wang, H., Wu, Y.B., Gao, S., Zheng, J.P., Liu, Q., Liu, X.C., Qin, Z.W., Ynag, S.H., Gong, H.J., 2014. Deep subduction of continental crust in accretionary orogen: evidence from U-Pb dating on diamond-bearing zircons from the Qinling orogen, central China Lithos 190-191, 420-429

Whitney and Evans, 2010 ; Donna L. Whitney, Bernard W. Evans., 2010. Abbreviations for names of rock-forming minerals American Mineralogist, Volume 95, pages 185-187

Wilkerson et al., 1988 ; Wilkerson, A., Carlson, W.D., and Smith, D. (1988) High-pressure metamorphism during the Llano orogney inferred from Proterozoic eclogites remnants. Geology, 16, 391-394

Wood 1980 ; Wood, D.A. 1980 the application of a Th-Hf-Ta diagram to problems of tectonomagmatic classification and to establishing the nature of crustal contamination of basaltic lavas of the british tertiary volcanic province. Earth and planetary science letter 50, 11-30

Wu and Zheng, 2013 ; Wu, Y.B., Zheng, Y.F., 2013. Tectonic evolution of a composite collision orogen: an overview of the Qingling-Tongbai-Hong'an-Dabie-Sulu orogenic belt in central China. Gondwana Research

Xu and Castillo, 2004 ; Xu, J.F., Castillo, P.R., 2004. Geochemical and Nd–Pb isotopic characteristics of the Tethyan asthenosphere: implications for the origin of the Indian Ocean mantle domain. Tectonophysics 393, 9–27.

Xu et al., 2002 ; Xu, J.F., Castillo, P.R., Li, X.H., Yu, X.Y., Zhang, B.R., Han, Y.W., 2002. MORB-type rocks from the Paleo-Tethyan Mian-Lueyang northern ophiolite in the Qinling Mountains, central China: implications for the source of the low Pb-206/Pb-204 and high Nd-143/Nd-144 mantle component in the INdian Ocean. Earth and Planetary Science Letters 198, 323-337

Yan et al., 2008 ; Yan, Q.R., Chen, J.L., Wang, Z.Q., Yan, Z., Wang, T., Li, Q.G., Zhang, Z.Q., Jiang, C.F., 2008. Zircon U–Pb and geochemical analyses for leucocratic intrusive rocks in pillow lavas in the Danfeng Group, north Qinling Mountains, China. Science in China (Series D) 51, 249–262.

Yang 2004 ; Yang TN, 2004. Retrograded textures and associated mass transfer: evidence for aqueous fluid action during exhumation of the Qinglongshan eclogite, Southern Sulu ultrahigh pressure metamorphic terrane, eatern China. J Metamorph Geol 22:653-669

Yang et al., 1986 ; YANG Z., CHENG Y. & WANG H. 1986 The Geology of China, Clarendon Press, Oxford.

Yang et al., 2006 ; Yang, Z., Dong, Y.P., Liu, X.M., Zhang, J.H., 2006. LA-ICP-MS zircon U-Pb dating of gabbro in the Guanzizhen ophiolite, Tianshui, West Qinling. Geological Bulletin of China 25, 1321-1325

Ye et al., 2006 ; Ye, H.S.,Mao, J.W., Li, Y.F., Guo, B.J., Zhang, C.Q., Liu,W.J., Yan, Q.R., Liu, G.Y., 2006. SHRIMP zircon U–Pb andmolybdenite Re–Os dating for the superlarge Donggou porphyryMo deposit in East Qinling, China, and its geological implication. Acta Geologica Sinica 80, 1078–1088 (in Chinese with English abstract).

You et al., 1991 ; You, Z.D., Suo, S.T., Han, Y.J., Zhong, Z.Q., Chen, N.S., 1991. The Metamorphic Progresses nd Tectonic Analyses in the Core Complex of an Orogenic Belt: An Example From he Eastern Qinling Mountains. China University of Geosciences, Wuhan, pp. 1–326 in Chinese with English abstract).

Yu Shi et al., 2013 ; Shi, Y., Yu, J.H., Santosh, M. Tectonic evolution of the Qinling orogenic belt, Central China: New evidence from geochemical, zircon U-Pb geochronology and Hf isotopes. Precambrian Research 231, 19-60

Yuan 1991 ; Yuan, X.C., 1991. Deep structure and tectonic evolution of Qinling orogenic belt. In:Ye, L.J., Qian, X.L, Zhahang, G.W., A Selection of Papers presented at the conference on the Qinling Orogenic Belt Northwest University Press, Xi'an, pp. 174-184

Zhai 2011 ; Zhai, M.G., 2011. Cratonization and the Ancient North China Continent: a summary and review, Sci China Earth Sci 54(8): 1110-1120

Zhai 2013 ; Zhai, M.G., 2013. The main old lands in China and assembly of Chinese unified continent. Science China Earth Sciences 56, 1829–1852.

Zhai 2014 ; Zhai, M.G., 2014. Multi-stage crustal growth and cratonization of the North China Craton. Geoscience Frontiers 5, 457–469.

Zhai and Bian, 2001 ; Zhai, M.G., Bian, A.G., 2001. Amalgamation of the supercontinental of the North China craton and ist break up during late-middle Proterozoic. Sci China Ser D-Earth Sci 43:219-232

Zhai and Santosh, 2011 ; Zhai, M.G., Santosh, M., 2011. The early Precambrian odyssey of the North China Craton: a synoptic overview. Gondwana Research 20, 6-25

Zhai et al., 1998 ; Zhai, X., Day, H.W., Hacker, B.R., You, Z.D., 1998. Paleozoic metamorphism in the Qinling orogen, Tongbai Mountains, central China. Geology 26, 371–374.

Zhang and Zhang, 1995 ; Zhang, Z.Q., Zhang, Q., 1995. Geochemistry of metamorphosed Late Proterozoic Kuanping ophiolite in the Northern Qinling, China. Acta Petrologica Sinica 11, 165-177

Zhang and Zhang, 1995 ; Zhang, Z.Q., Zhang, Q., 1995. Geochemistry of metamorphosed Late Proterozoic Kuanping ophiolite in the Northern Qinling, China. Acta Petrologica Sinica 11, 165–177 (Suppl., in Chinese with English Abstract).

Zhang C.L. , 1994a ; Zhang, C.L., Zhang, G.W., Lu, X.X., 1994a. Characteristics and orogin of Kuanping granite body in the East Qinling. Northwest Geoscience 15, 27–34 (in Chinese with English Abstract).

Zhang C.L. , 2004a ; Zhang, C.L., Li,M.,Wang, T., Yuan, H.L., Yan, Y.X., Liu, X.M., Wang, J.Q., Liu, Y., 2004a. U–Pb zircon geochronology and geochemistry of granitoids in the Douling Group in the Eastern Qinling. Acta Geologica Sinica 78, 83–95 (in Chinese with English abstract).

Zhang C.L. , 2004b ; Zhang, C.L., Liu, L., Zhang, G.W.,Wang, T., Chen, D.L., Yuan, H.L., Liu, X.M., Yan, Y.X., 2004b. Determination of Neoproterozoic post-collisional granites in the north QinlingMountains and its tectonic significance. Earth Science Frontiers 11, 33–42 (in Chinese with English abstract).

Zhang et al., 1989 ; Zhang, G., Yu, Z., Sun, Y., Cheng, South, Li, T., Xue, F., Zhang, C., 1989. The major suture zone of the Qinling orogenic belt: Southeast Asian Earth Sciences, v.3, p. 63-76

Zhang et al., 1991 ; Zhang, S.Y., Hu, K., Qiao, L.Y., Liu, X.C., 1991. The origin and rock assemblage of aciend intracontinental collaps in collision zone: a discription of the HP metamorphic belt in central China. In: Ye, L.J., Qian, X.L., Zhang, G.W., (Eds.), A selection of papers presented at the conference on the Qinling Orogenic Belt. Northwest universtity Press, Xi'an. pp, 48-56

Zhang et al., 1994b ; Zhang, Z.Q., Liu, D.Y., Fu, G.M., 1994b. Isotopic Geochronology of Metamorphic Strata in North Qinling. Geological Publishing House, Beijing, pp. 1–191 (in Chinese with English abstract).

Zhang et al., 1994b ; Zhang, Z.Q., Liu, D.Y., Fu, G.M., 1994b. Isotopic Geochronology of Metamorphic Strata in North Qinling. Geological Publishing House, Beijing, pp. 1–191 (in Chinese with English abstract).

Zhang et al., 1996 ; Zhang, H.F., Zhang, B.R., Ling, W.L., Luo, T.C., Xu, J.F., 1996a Paleo-oceanic crust recycling in north Qinling evidence of Pb, Nd, Sr isotopes from island arc granitoids. Chinese Science Bulletins 41, 234-237

Zhang et al., 1997a ; Zhang, H.F., Gao, S., Zhang, B.R., Luo, T.C., Lin, W.L., 1997a. Pb isotopes of granites suggest Devonian accretion of Yangtze (South China) craton to North China craton. Geology 25, 1015–1018.

Zhang et al., 2000 ; Zhang, H.F., Gao, S., Zhang, L., Zhong, Z.Q., Zhang, B.R., 2000b. Granitoids in erlangping ophiolite fragment from northern tongbai area, china: geochemistry, petrogenesis and deep crustal nature. Scientia Geologica Sinica 35, 27–39.

Zhang et al., 2001 ; Zhang, G.W., Zhang, B.R., Yuan, X.C., 2001. Qinling Orogenic Belt and Continent Dynamics. Science Press, Beijing, pp. 1–855.

Zhang et al., 2010 ; Zhang, Z.W., Li, W.Y., Zhao, D.H., Gao, Y.B., Peng, S.X., 2010. Zircon U-Pb dating of Lianhuagou Pluton in East Qinling and its geological implications. Geochimica 39, 90–99 (in Chinese with English abstract).

Zhang et al., 2014 ; Zhang, H-F., Yu, H., Zhou, D-W., Zhang, J., Dong, Y.P., Zhang, G.W 2014. The meta-gabbroic complex of Fushui in north Qinling orogen: A case of syn-subduction mafic magmatism. Gondwana research 2014

Zhang G.W. et al., 1995 ; Zhang, G.W., Meng, Q.R., Lai, S.C., 1995. Tectonics and structure of the Qinling Orogenic belt. Science in China Series B 38, 1379-1394

Zhang G.W. et al., 1995a ; Zhang, G.W., Meng, Q.R., Lai, S.C., 1995a. Structure and tectonics of the Qinling Orogenic belt. Science in China. Series B 25, 994–1003.

Zhang G.W. et al., 1995b ; Zhang, G.W., Meng, Q.R., Lai, S.C., 1995b. Tectonics and structure of the Qinling Orogenic belt. Science in China. Series B 38, 1379–1394.

Zhang G.W. et al., 1996 ; Zhang, G.W., Meng, Q.R., Yu, Z.P., Sun, Y., Zhou, D.W., Guo, A.L., 1996b. Orogenesis and dynamics of Qinling orogen. Science in China 26, 193-200

Zhang G.W. et al., 2000 ; Zhang, G.W., Yu, Z.P., Dong, Y.P., Yao, A.P., 2000. On Precambrian framework and evolution of the Qinling belt. Acta Petrologica Sinica 16, 11–21 (in Chinese with English abstract).

Zhang G.W. et al., 2000a ; Zhang, G.W., Yu, Z.P., Dong, Y.P., Yao, A.P., 2000a. On Precambrian framework and evolution of the Qinling belt. Acta Petrologica Sinica 16, 11–21.

Zhang G.W. et al., 2001 ; Zhang, G.W., Zhang, B.R., Yuan, X.C., Xiao, Q.H., 2001. Qinling Orogenic Belt and Continental Dynamics. Science Press, Beijing. pp. 1–855.

Zhang, 1999 ; Zhang, Z. J., 1999. Metamorphic evolution of garnet-clinopyroxene-amphibole rocks from the Proterozoic Songshugou mafic-ultramafic complex, Qinling Mountains, central China, The Island Arc 8, 259-280

Zhao and Zhai, 2013 ; Zhao, G.C., Zhai, M.G., 2013. Lithotectonic elements of Precambrian basement in the North China Craton: review and tectonic implications. Gondwana Research 23, 1207–1240.

Zhao et al., 2001 ; Zhao G, Cawood PA, Wilde SA, Lu L (2001) High-pressure granulites (retrograded eclogites) from the Hengshan Complex, North China craton: petrology and tectonic implications. J Petrol 42: 1141–1170

Zhou et al., 1995 ; Zhou, D.W., Zhang, C.L., Han, S., Zhang, Z.J., Dong, Y.P., 1995. Tectonic setting on the two different tectonic magma complex of the East Qinling in Early Paleozoic. Acta Petrologica Sinica 11, 115–126.

Zhou et al., 2008 ; Zhoug, J.C., Wang, X.L., Qiu, J.S., 2008. Is the Jiangnan Orogenic belt a Grenvillian Orogenic Belt some problems about the Precambrian geology of South china. Geological Journal China Univ 14:64-72

Zhu 2001 ; Zhu, B.Q., 2001. Geochemical Province and Geochemical Steep Zone. Sceience Press, Beijing, pp. 1–118

Zhu et al., 2008a ; Zhu, L.M., Zhang, G.W., Guo, B., Li, B., 2008a. U–Pb (LA-ICP-MS) zircon dating for the large Jinduicheng porphyry Mo deposit in the East Qinling, China, and its metallogenetic geodynamical setting. Acta Geologica Sinica 82, 204– 220.